Simon Feigl

Heat Transfer Measurements at Ultra Low Temperatures for the Antimatter Experiment AEGIS at CERN

Master Thesis

For obtaining the academic degree
Diplom-Ingenieur

Diploma Programme of
Technical Physics

Graz University of Technology

Supervisor:

Univ.-Prof. Dr. Laurentius Windholz
Institute of Experimental Physics

In cooperation with CERN

Graz, October 2010

To my parents, my brother and my grandmother.

Deutsche Fassung:
Beschluss der Curricula-Kommission für Bachelor-, Master- und Diplomstudien vom 10.11.2008
Genehmigung des Senates am 1.12.2008

EIDESSTATTLICHE ERKLÄRUNG

Ich erkläre an Eides statt, dass ich die vorliegende Arbeit selbstständig verfasst, andere als die angegebenen Quellen/Hilfsmittel nicht benutzt, und die den benutzten Quellen wörtlich und inhaltlich entnommene Stellen als solche kenntlich gemacht habe.

Graz, am ……. ……..
(Unterschrift)

Englische Fassung:

STATUTORY DECLARATION

I declare that I have authored this thesis independently, that I have not used other than the declared sources / resources, and that I have explicitly marked all material which has been quoted either literally or by content from the used sources.

……. ……..
date (signature)

Abstract

The AEgIS experiment at CERN will use antihydrogen atoms to investigate the gravitational interaction of antimatter with matter. The experimental setup includes a Penning trap, whose copper electrodes will be cooled to 100 mK. To do so, they have to be in very good thermal contact with the cold mixing chamber of a dilution refrigerator. At the same time, this contact has to ensure electrical insulation. One solution to this problem is a sapphire disk, which is placed between the electrodes and the cold surface of the mixing chamber. Thin indium layers on either side of the disk provide relatively good thermal contact. However, the interface between a metal and a dielectric acts as an effective thermal resistance at ultra low temperatures. This resistance and other thermal properties depend strongly on the preparation of the contact, especially on the surface treatment of the sapphire disks. Four differently prepared contacts are investigated in this work in order to find the solution which optimizes the heat transfer from the electrodes through the sapphire disk to the mixing chamber. This is done by thermal measurements on a test setup at temperatures between 30 and 130 mK. These very low temperatures are reached using the dilution refrigerator at CERN's central cryogenic laboraty. The obtained results are used to estimate the thermal behaviour of the future AEgIS setup.

Kurzfassung

Das Experiment AEgIS am CERN wird mithilfe von Antiwasserstoff die gravitationelle Wechselwirkung zwischen Materie und Antimaterie untersuchen. Der experimentelle Aufbau beinhaltet eine Penning-Falle, dessen Kupferelektroden auf 100 mK gekühlt sein werden. Um dies zu erreichen müssen die Elektroden thermisch möglichst gut an die Mischkammer eines Verdünnungskryostaten ankontaktiert sein, wobei gleichzeitig elektrische Isolierung gegeben sein muss. Eine Lösung für dieses Problem bietet Saphir, welcher als Plättchen ausgeführt zwischen den Elektroden und der Mischkammer positioniert ist. Thermischer Kontakt wird hierbei über dünne Indiumschichten auf beiden Seiten des Plättchens realisiert. Bei sehr tiefen Temperaturen, wie sie hier auftreten, bildet die Grenzschicht zwischen einem Metall und einem Dielektrikum einen beachtlichen thermischen Widerstand. Dieser Widerstand sowie weitere thermische Eigenschaften sind sehr stark abhängig von der Oberflächenbeschaffenheit und -behandlung der am Kontakt beteiligten Materialien. In dieser Arbeit werden vier verschieden präparierte Kontakte untersucht. Ziel dabei ist es, den thermisch besten Kontakt zu identifizieren, welcher den Wärmeübergang von den Elektroden über ein Saphirplättchen zur Mischkammer maximiert. Dafür werden an einem Testaufbau thermische Messungen im Bereich von 30 bis 130 mK durchgeführt. Diese tiefen Temperaturen werden mithilfe eines Mischungskryostaten erreicht, welcher im Kältelabor des CERN verfügbar ist. Mit den gewonnenen Resultaten werden Abschätzungen des thermischen Verhaltens des zukünftigen AEgIS-Versuchsaufbaus gemacht.

Acknowledgements

Many people have supported me conducting the work and writing this thesis. They have provided valuable academic and practical advice, have always been willing to go into discussions and have assisted generously with their experience and work.
I want to thank Prof. Dr. Laurentius Windholz from Graz University of Technology for his academic supervision, and Mr. Michael Doser from CERN's physics departement for providing the position as a technical student and being my direct supervisor at CERN. Furthermore I want to thank Mr. Johan Bremer for accepting me in his section, the CERN cryogenic laboratory.
Special thanks go to my colleagues Mr. Thomas Eisel, Mr. Torsten Koettig and Mr. Gerhard Burghart, which have introduced me to the methods in the laboratory and have spent a lot of time and effort to support my work and answer questions.
Last but not least I want to thank the whole team of the cryogenic laboratory, especially Mrs. Laetitia Dufay-Chanat, Mr. Sebastien Prunet, Mr. Jihao Wu, Mr. Daniel Cochet, Mr. Jean Louis Servais and Mr. Sylvain Devidal for their support.

Contents

X

Nomenclature

Abbreviations

AD	antiproton decelerator
AEgIS	Antimatter Experiment: Gravitation, Interferometry, Spectroscopy
Al_2O_3	aluminum oxide
BC	boundary conditions
CCDR	CERN Cryolab Dilution Refrigerator
CERN	European Organization for Nuclear Research
Cryolab	central cryogenic laboratory at CERN
G-10	glass-fiber reinforced epoxy laminate
GPIB	general purpose interface bus
GUI	graphical user interface
HV	high voltage
IC	initial conditions
IVC	inner vacuum chamber
LINAC	linear accelerator
LS	labeling of LakeShore temperature sensor
MC	mixing chamber
OFHC	oxygen-free high thermal conductivity (quality standard for elementary copper)
PDE	partial differential equation
PVD	physical vapor deposition
RF	radio frequency
RTD	resistive thermal device
RuO_2	ruthenium oxide

Trademarks

Kapton®	polyimide film used widely in cryogenics
LabVIEW®	platform and development environment for the visual programming language *G* from *National Instruments*®
MATLAB®	programming language by *The MathWorks, Inc.*

1 Introduction

1.1 Motivation

The current standard model of particle physics describes the known particles and most of their interactions accurately. It is a very powerful theory, but one force, which is the most obvious in daily live, still can't be understood by it: gravitation. Newton's theory of gravitation and Einstein's general theory of relativity cover gravitation, but physicists have not yet succeeded in incorporating it into the standard model. A potential way of finding hints to this unification is to investigate the gravitational interaction of "ordinary" matter with a kind of matter, which is well included in the standard model: antimatter. The "Antimatter Experiment: Gravitation, Interferometry, Spectroscopy" (AEgIS) at the European Organization for Nuclear Research (CERN) is a future experiment which will investigate this interaction of matter with antimatter. AEgIS will use uncharged atoms of antihydrogen, since measurements on charged particles would be perturbed by any stray electromagnetic field. This effect has already hindered two experiments in the 1970s and 1990s in conducting successful measurements on this subject[1, 2].
The antihydrogen in AEgIS will be produced in a Penning trap and then accelerated towards a detector, where the vertical deflection due to gravity is measured. In order to get a good signal, the atoms have to be at a temperature of about 100 mK before being accelerated. This temperature is reached by cooling antiprotons to this low temperature before they are used for antihydrogen formation. These antiprotons are thermally coupled to the electrodes of the Penning trap via an electron plasma. Therefore the electrodes have to be cooled accordingly. Now the difficulty is to find a reliable, thermally effective contact from the electrodes to a cooling device, which also has to guarantee the electrical insulation between the high potential of the electrodes and ground.
This thesis investigates this problem and focuses on thermal tests of a possible solution. It deals mainly with thermal contacts at ultra low temperatures and how to measure and quantify thermal contact properties. The aim is to find a solution, which enables AEgIS to operate at its foreseen performance to reveal knowledge about the gravitational

interaction of matter with antimatter.

1.2 Task

The central part of AEgIS houses the region in which the antihydrogen atoms are formed out of cold antiprotons and positronium. This formation is done in a Penning trap, whose electrodes surround the cloud of particles completely (except for small entrance and exit regions). The cooling is effected via the electrodes, so the electrodes have to be at the foreseen temperature of the atoms, which is 100 mK, or even lower. The only device providing continuous cooling performance in this temperature range is a dilution refrigerator[3]. The electrodes have to be in a very good thermal contact with the cold surface of a dilution refrigerator: its mixing chamber, which is made out of copper. On the other hand, the electrodes are charged up to 1 kV and have to be electrically insulated from the cold surface connected to ground potential, and from each other.
The solution for this problem, investigated in the presented work, is the so-called "sandwich-solution", where the electrodes are mounted on the surface of the mixing chamber, electrically insulated and thermally connected by sapphire disks and different layers of indium. For AEgIS it is crucial to know if and how fast the heatloads acting on the electrodes can be transferred away so as to maintain the operating temperature. In literature there is useful information on metal-indium-sapphire contacts[4, 5, 6], but these contacts were not investigated under the conditions of AEgIS. Most important, AEgIS' temperatures are below any others where measurements have been found for. In order to give a definite answer to the question if the heatloads can be handled, new measurements down to 30 mK and with sandwiches applicable in AEgIS had to be conducted. These measurements and the results are presented in this work.
Another solution investigated is the "rod-solution", where the electrodes reach into the mixing chamber and the ^{3}He-^{4}He mixture has to withstand the differences of potential. In this work, a literature research on the resistance of the mixture to electrical breakdown is included. The complete development and discussion of the rod-solution will be included in the doctoral thesis of my colleague T. Eisel[7].

1.3 Outline of work

The needs of AEgIS set the whole framework for this work. CERN's Cryolab is one of the many institutions working on AEgIS and it is in permanent contact with other

collaboration partners of the experiment. While the Cryolab is in charge of the whole cooling system of AEgIS, this thesis focuses on the thermal performance of the contact between the electrodes of the Penning trap and the mixing chamber of the dilution refrigerator.
The foundations of this work are the specifications of the electrodes, defined by the physics and the mechanical layout of the experiment, see chapter 2. Based on them, two possible solutions for the problem are discussed. The sandwich-solution seems suitable for AEgIS and is therefore investigated in detail. Since the thermal performance is of main interest, theories of heat transfer at very low temperatures are studied in chapter 3. The experimental setup for the thermal measurements conducted is described in chapter 4. The measurements, their results and the consequences for AEgIS are discussed in chapter 5. Literature shows that the surface treatment of the sapphire disk and the application method of indium have fundamental influence on the thermal behavior of the contact. Therefore differently prepared sandwiches are measured, which indeed lead to different overall thermal performances. The summary of the work and the conclusions are given in chapter 6.

Appendix A lists the collaboration partners of AEgIS.

2 AEgIS and its challenge for cryogenics

In it's current state, the standard model of particle physics struggles to describe gravitation. In contrast, the other fundamental forces - electroweak and strong interaction - and all known particles are astonishingly well described[8]. Furthermore, the standard model predicts yet undiscovered particles (like the Higgs boson) and leaves possibilities open for new particles (e.g. dark matter). Therefore there are many different ways where physicists could find a hint on how to incorporate gravitation into the standard model. One of them is to investigate how antimatter, which is well included in the standard model, interacts gravitationally with matter. There have been attempts to measure this interaction but none of them was successful [1, 2]. These experiments have however revealed that charged antiparticles like antiprotons are not suitable for such an experiment. The problem is that even when taking earth's large mass into account, gravitational effects on such particles are overshadowed by electromagnetic effects. For a successful measurement a ratio of gravitational force to electromagnetic force of 1:100 has to be reached[9]. A simple calculation shows that any electric field larger than $0.1\,\mu$V/m will exceed this ratio[1]. The case with magnetic fields is similar. Since it is impossible to realize such a field-free environment in an apparatus handling antimatter, no revealing measurements have been conducted until now.

To avoid the problem of stray electromagnetic fields, neutral antimatter particles have to be used. Until now, antihydrogen is the most promising candidate for investigation. It has only been produced and detected in a laboratory since 1995[10]. At those times, the energy of the antihydrogen atoms was too high to conduct studies on it. Only in 2002, after installation of the Antiproton Decelerator (AD) and its first experiments at CERN, it was possible to produce the first cold (i.e. low kinetic energy) antihydrogen [11]. By now, the production rate of antihydrogen atoms is high enough to produce significant

[1] A simple comparison of the gravitational force acting on a proton on earth ($\vec{F}_g = m_p \cdot \vec{g}$) and the force in an electric field ($\vec{F}_{el} = q \cdot \vec{E}$) yields that figure.

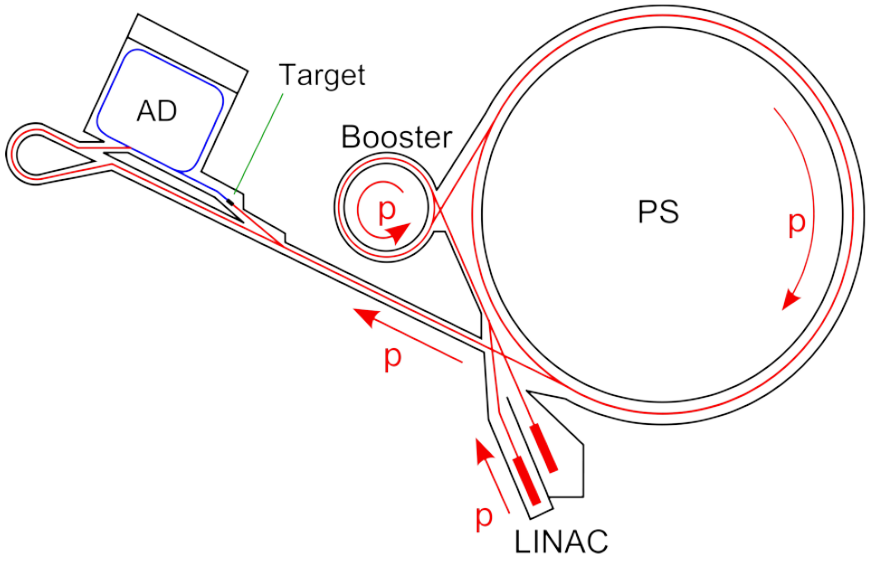

Figure 2.1: Scheme of antiproton production at CERN[15]. Protons (p) are first accelerated by the linear accelerator (LINAC), then boosted to an intermediate energy level before being further accelerated by the proton synchrotron (PS). Antiprotons are produced by directing the beam of protons from the PS onto a special target made out of iridium. Red: protons, blue: antiprotons.

amounts of it in an acceptable time span. This makes the direct measurement of earth's gravitational acceleration on antimatter, $\bar{g}$, possible. AEgIS' major aim is to measure $\bar{g}$ with a relative precision of 1 % [12].

2.1 AEgIS setup

AEgIS will be located at CERN in Geneva, Switzerland, since the laboratory's AD can provide low-energy antiprotons to produce cold antihydrogen[13]. The AD-complex is connected to the accelerator complex at CERN and uses protons from the Proton Synchrotron (PS) with a momentum of 26 GeV/c to produce antiprotons, see Figure 2.1. The antiprotons are subsequently decelerated ("cooled") to 100 MeV/c and then used to create antihydrogen[14].

Next to AEgIS, the AD-hall will house four other experiments, already installed and running. That's why AEgIS has only limited space available in this hall, posing external restrictions to its design and construction. The current layout of the experiment is shown in Figure 2.2. Main features include the two superconducting magnets necessary for the particle beam environment. There will be two beams to the experiment, providing an-

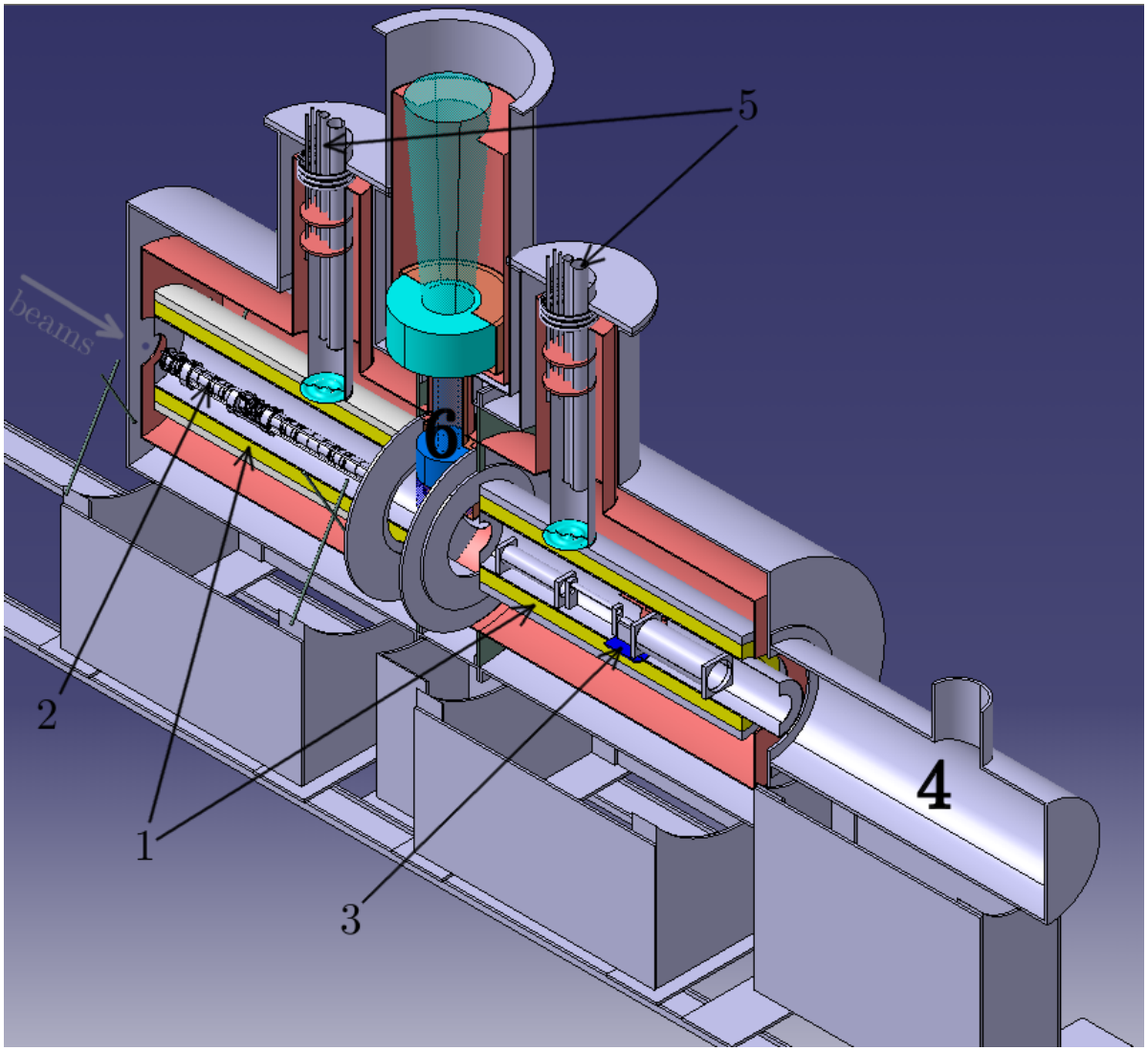

Figure 2.2: Setup of AEgIS. 1 . . . superconducting magnets (yellow), 2 . . . beamline for the incoming beams, 3 . . . central part for the production and acceleration of antihydrogen (100 mK-region and mixing chamber of dilution refrigerator), 4 . . . deflectometer and detector unit, 5 . . . cryogenic supply for the superconducting magnets, 6 . . . dilution refrigerator (not shown)

tiprotons and positrons, respectively. The beam of anihydrogen will be formed within the experiment. That means the antihydrogen is not provided from an outside source, but produced within the apparatus. The recombination of the antiprotons and positrons to antihydrogen will take place in a Penning trap, in the so-called "central" or "cold" part of the experiment. Therein, antiprotons from the AD will be accumulated and cooled during a time of about 120 s. During operation, the experiment will be intermittent with this period. At the same time, positrons will be accumulated in a separate trap parallel to the antiproton beam line. As soon as enough particles have been accumulated, the positrons will be sent into the antiproton trap after having been converted to positronium, which is immediately laser-excited[16]. Only this process will guarantee the recombination of antihydrogen. The recombination process will take place within about $1\,\mu s$[17], after which the atoms will immediately be accelerated horizontally towards the detector unit. The detector is a Moiré-deflectometer, which will detect the vertical deflection of the antihydrogen beam due to earth's gravitational field. The gravitational acceleration of antimatter, $\bar{g}$, will then directly be calculated from this measured free fall. Therefore, the precision of the measurement will be directly linked to the preparation of the antiyhdrogen beam. To detect the vertical deflection only due to gravity, the atoms must have velocities pointing exactly horizontally to the deflectometer just when they begin their free fall. However, the atoms' velocities will always have a random vertical component according to the Maxwell-Boltzmann distribution. The mean value of this component is smaller the lower the temperature, so a cooler antihydrogen cloud means a better directed beam and therefore a more better signal. In order to achieve the foreseen relative precision of 1 % in an acceptable time span of about one month, current specifications of the experiment set the temperature of the antihydrogen cloud before acceleration to 100 mK[16, 17].

2.2 The cold part

Since the antihydrogen will be used immediately after it's creation, there will be no time to cool the atoms. Instead, the constituent particles will already have to be at the foreseen low temperature before antihydrogen formation. Especially the antiprotons have to be already at about 100 mK before they recombine with the positrons[17]. Therefore, the trapped antiprotons will have to be cooled in their storing device, the Penning trap. With the exception of small entrance and exit regions, the electrodes of the Penning trap will completely enclose the accumulated antiprotons, so the electrodes also have to

be cooled to at least 100 mK. The thermal coupling of the antiprotons to the electrodes is done by a cold electron gas. Active cooling of the antiprotons is additionally achieved by resistive cooling via appropriate variation of the electrodes' potentials.
Since the cooling of the antiprotons and more significantly other heatloads would permanently raise the electrodes' temperature, it is necessary to contact the electrodes to a cooling device, which is continuously providing cooling power. In this temperature range, only a dilution refrigerator is capable of doing so. Ergo, the electrodes will have to be thermally well connected to the cold part of a dilution refrigerator, its mixing chamber (dilution refrigeration is explained in section 4.3). On the other hand, the Penning trap requires high voltages (HV) and differences in potential of up to 1 kV will occur. The electrodes have therefore to be electrically insulated from each other and also from the mixing chamber. The latter poses the problem treated in this thesis: testing various materials and setups to find the optimum solution, ensuring sufficient thermal contact and electrical insulation below 100 mK.

2.3 The electrodes

As mentioned above, the very central part of AEgIS is the Penning trap, where antiprotons are stored and cooled and antihydrogen is produced and accelerated. The required design and properties of the trap are given by its physics and are taken care of by the INFN-group (Istituto Nazionale di Fisica Nucleare, Genova, Italy) of the AEgIS-collaboration[2]. An internal collaboration document finally sets the specifications for the trap[18]. In the following list, the most important constraints resulting from this document are given. In Figure 2.3 a possible design of the trap is shown.

- The electrodes' internal geometry has to form a circular hole with a diameter of (14 ± 0.01) mm, the center of it being the axis of the antiproton beam. Apart from the outermost electrodes, also the thickness of the electrodes along the beam axis is given. The outer geometry can be adapted to the needs of the cooling system.
- There are 10 electrodes at ≈ 100 mK sitting consecutively along the beam axis with a distance of (1 ± 0.01) mm between them. Some of them are split into four electrically independent sectors, see Figure 2.4.
- All electrodes an all sectors have to be electrically insulated from each other and from ground potential to allow for HV to be applied.

[2]The full collaboration list can be found in appendix A.

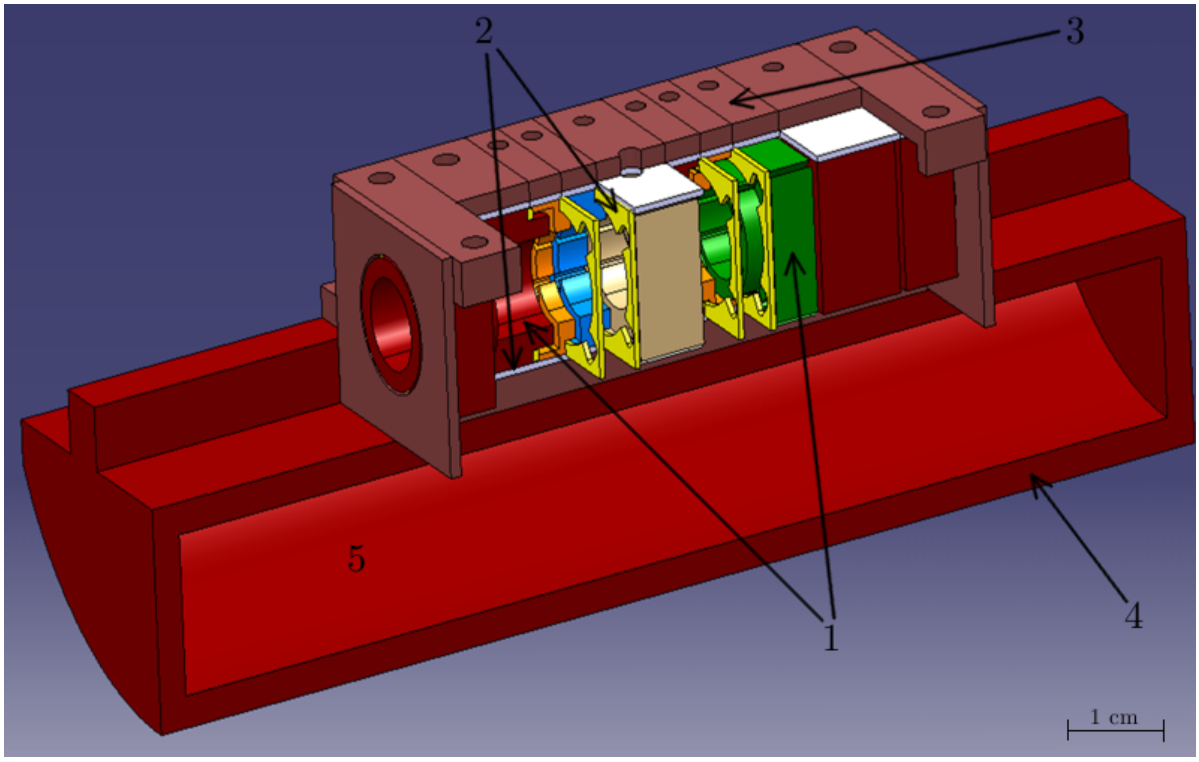

Figure 2.3: The Penning trap of AEgIS, partially opened. 1 . . . electrodes (selection; only two of 10 are marked with arrows), 2 . . . sapphire spacers (selection; all the light blue and yellow parts are sapphire disks), 3 . . . support frame (copper), 4 . . . mixing chamber of the dilution refrigerator (copper), 5 . . . volume of the mixing chamber filled with ^{3}He and ^{4}He.

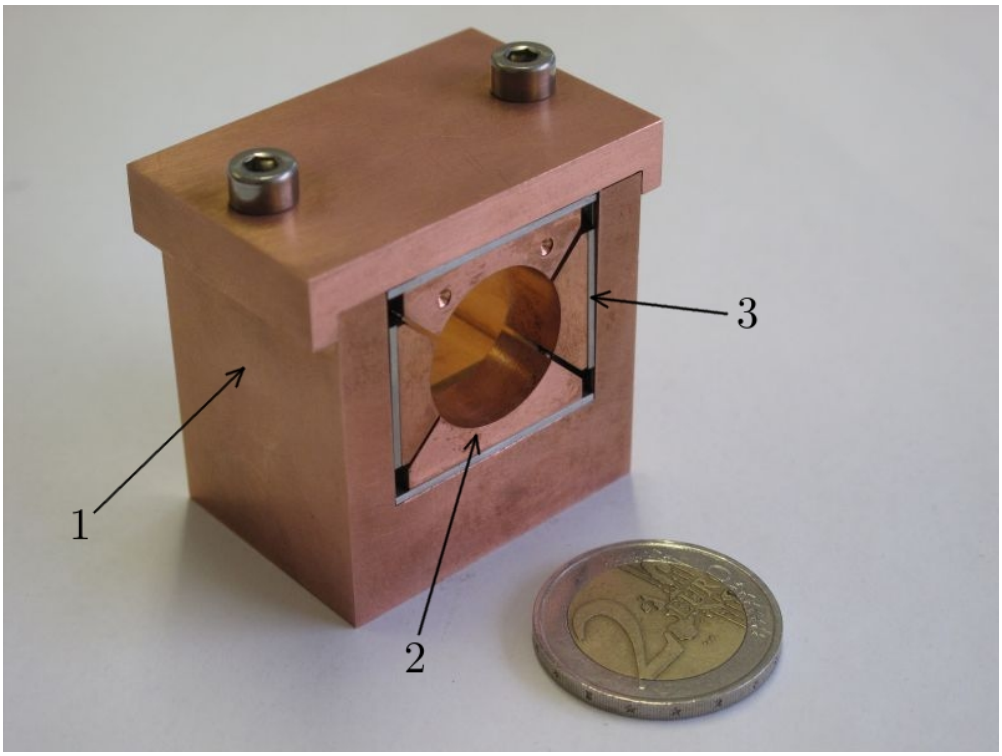

Figure 2.4: A test electrode of the Penning trap and it's mechanical support. The electrode is surrounded by a copper frame (1), which ensures mechanical stability and thermal contact to the mixing chamber. This electrode is split into four sectors (arrow 2 points on one of them), with each of them being electrically insulated from other copper parts by sapphire disks and spacers (3).

- The particles traveling along the beam axis must not "see" any of the insulation material but only electrode material.
- Any material used must not influence the necessarily needed highly homogeneous magnetic field generated by the outer superconducting magnet.
- Any material used needs to be radiation hard, since during operation it will be exposed to gamma radiation from annihilation as well as particle radiation from beam losses.
- Strict geometrical tolerances have to be applied.

In addition, the electrodes' inner surfaces need to be gold coated to guarantee a smooth surface and prevent oxidation for times where the setup is exposed to the normal atmosphere. Each electrode and sector needs to be connected for power supply from outside. All these restrictions lead to a more or less intricate package of electrodes, insulation material and connections. One possible design is shown in Figure 2.3. Geometric tolerances can be met at room temperature, but during cooldown to the operating temperature misalignments can't be ruled out. The operation temperature also provides the basis for this work: over and above all difficulties resulting from the mentioned requirements, a major challenge is the thermal contact of the electrodes to the cooling device. Materials, which conduct heat well at low temperatures are normally also good electrical conductors and therefore not suited for the required contact. Two possible solutions to this issue are given in the next sections, where the latter one will be further investigated in the following chapters of this thesis.

2.4 Rod-Solution

The rod-solution avoids the problem of finding a material, which conducts heat well and insulates electrically at the same time at very low temperatures. This is achieved by separating the thermal contact from the part where electrical insulation is needed. In Figure 2.5 the basic principle is shown: the electrodes are placed on the mixing chamber lid and are electrically insulated from it and from each other by an appropriate material. Here the insulation material doesn't have to conduct heat well at the same time, since the thermal contact is realized elsewhere. Concerning the material issue, this simplifies construction. The material for the thermal contact can be chosen to maximize thermal performance. Therefore, the contact is realized by rods out of oxygen-free high

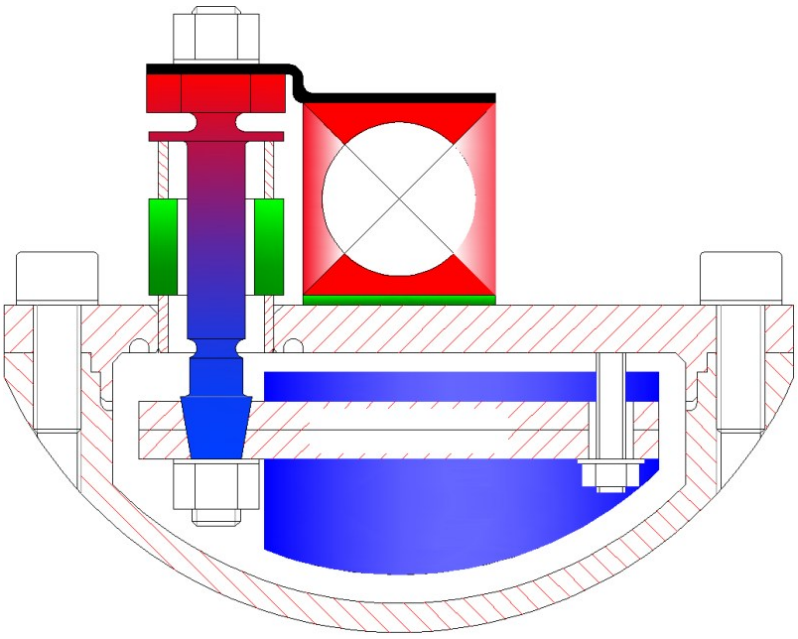

Figure 2.5: Sectional drawing of the rod-solution on the AEgIS setup. The hatched part is the mixing chamber with the heat exchanger inside (blue). On the left the rod leads from the cold inside of the mixing chamber to the outer warm part (red). There it is contacted to the electrode via a metal part (black). Electrical insulation is achieved by the green pieces, which - at least for the rod - is a ceramic ring out of Al_2O_3.

thermal conductivity (OFHC) copper, the standard material used for any cold parts in the dilution refrigerator. The rods sit aside the electrode package on the mixing chamber lid and extend into the mixing chamber. Each of them has its own heat exchanger within the mixing chamber, since the cooling power is provided right there. Each electrode is connected to such a rod. The connection is made of bulk copper or copper cables, which ensures very good thermal contact but on the other hand also electrical contact. This electrical contact means that any metal part connected to the rod will be at the same potential as the electrode. Therefore, electrical insulation has to be guaranteed at the inlets of the rods on the mixing chamber lid and inside the mixing chamber between the heat exchangers. The insulation from the lid is realized by a tubular ceramic piece also realizing the mechanical support, see Figure 2.6. This insulation is however not guaranteed in a straightforward way, since the environment within the mixing chamber is not beam vacuum like outside, but the ^{3}He-^{4}He mixture of the dilution refrigerator. Thus, the electrical breakdown strength of the helium mixture is the crucial factor of the rod-solution.

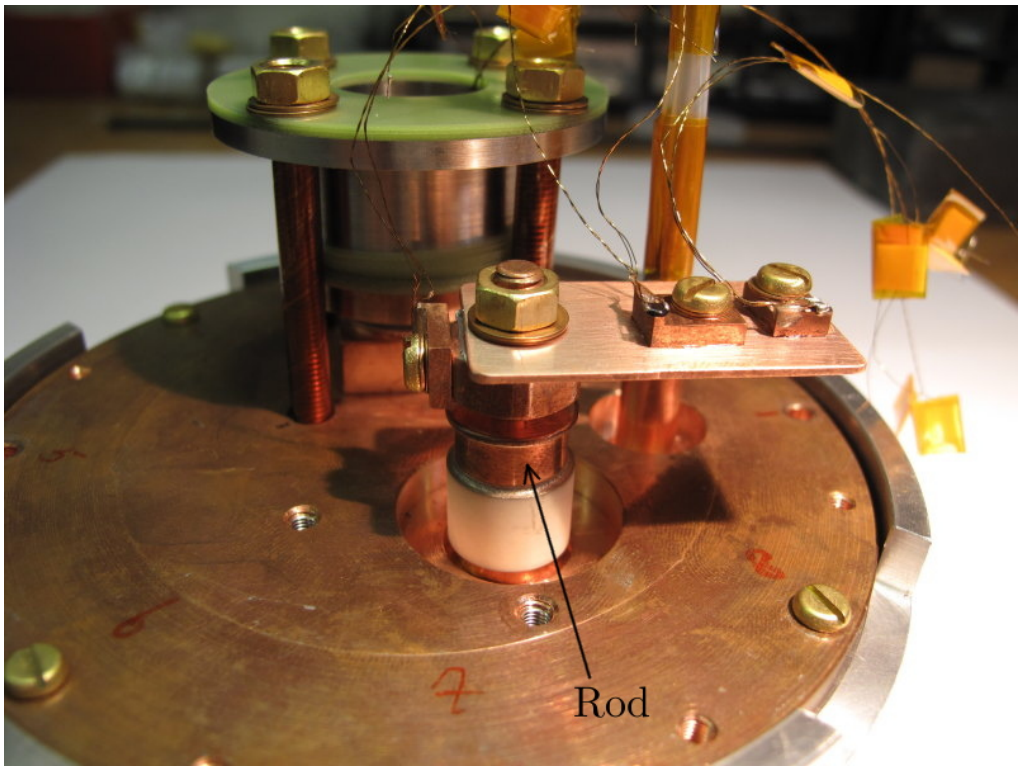

Figure 2.6: Test-rod mounted on the mixing chamber (in the foreground). The white ceramic ring realizes electrical insulation between the rod and the mixing chamber lid. All other parts are metals (mainly OFHC copper) to ensure good thermal conductance. In this setup no electrode is connected to the rod, so just the rod with mounted heater and sensors is visible.

2.4.1 Electrical breakdown strength of the helium mixture

The electric breakdown strength of the helium mixture is not easy to estimate and extensive literature research has been done to get information about it. The challenge is that electrical breakdown in the mixing chamber has to be avoided in any case. First of all, the electronics wouldn't bear a breakdown and second, the effects on the dilution refrigerator are not known. Therefore, it has to be estimated in advance if the mixture withstands the high voltage.
The environment in the mixing chamber will have the following characteristics: The critical distances will be in the range of millimeters within a bath of liquid helium. The bath consists of two separated phases, a mixed phase (94 % ^{4}He and 6 % ^{3}He) and an almost pure ^{3}He phase. The applied voltage per electrode will be continuously $\approx 100\,\mathrm{mV}$ and up to 1 kV for the acceleration pulse (rise time 50 μs, then controlled exponential falloff). In order to have a safety margin the setup should be robust up to even higher values. The temperature will be 50 mK and the pressure 0.1 mbar. Under these conditions both ^{3}He[19] and ^{4}He are in the fluid state (^{4}He is even in the superfluid state, called He II). A homogeneous magnetic field of 1 T will be applied. Due to the presence of antimatter, annihilation will occur and the resulting γ radiation will ionize atoms in the mixing chamber. For this reason, at any given moment an estimated 10^5 extra charge carriers will be available in the volume of the mixing chamber[9].
As expected, no published figures have been found for exactly these conditions. Especially the low pressure poses a problem; most of the found measurements have been conducted at higher pressure. Also the temperature has hardly ever been found to be lower than 1.5 K. So any values stated in the literature research below are only valid for the conditions in the respective reference. Still, they provide a starting point for an estimation of what to expect under the conditions of AEgIS.

In detail, for the AEgIS setup the following question have to be answered:

- Will an electrical breakdown occur within the considered voltage range?

- Will there be leakage currents at any voltage applied?

Toward answering these questions, the following literature research has been conducted.

2.4.2 Literature research

The most informative measurements were found in a paper and the dissertation of B. Sethumadhavan et al.[20, 21]. They include temperatures down to 100 mK and also radiative environment (realized by a 0.5 mCi β^- emitter, ^{63}Ni). Their setup has been a cylindrical cell (the copper electrodes being the top respectively bottom face) with 4 mm gap size.
Measurements have conducted on the cell completely filled with liquid ^{4}He and with the radioactive source mounted. No breakdown has been observed in the given voltage range (up to 2 kV), but leakage currents have been detected. The current has been found to be directly proportional to the source activity. This is due to separation of electrons from ions by the electric field, which prevents recombination. The saturation current (i.e. all secondary electrons are separated) has been estimated to be 600 pA. The current characteristics have changed after ^{3}He has been added, see Figure 2.7. However, this effect has only been present below ≈ 1 kV.
Furthermore, below 1 K the characteristics have not shown significant dependence on the temperature any more.
Measurements have also been conducted on a partially filled cell. There breakdown has occurred at -1300 V, +600 V respectively. Important findings have been that there were no precursors to breakdown seen and the breakdown has been accompanied by a rapid increase of cell temperature. This supports the demand of avoiding breakdown in AEgIS' test setup.
All measurements have been done under slight overpressure (i.e. >1013 mbar). A pressure dependence of the breakdown current has been observed: the higher the pressure the better for avoiding breakdown[22]. This is a disadvantageous observation for AEgIS, since the pressure in the mixing chamber is around 0.1 mbar.

Parameters' influence on breakdown strength

Several other publications on liquid ^{4}He have been studied and the following tendencies have been found.

- **Temperature**
  Below 1 K there is no temperature dependence observable of a possible leakage current[21].

- **Pressure**
  Lower pressure results in lower breakdown strength[22].

- **Magnetic field**
  Trajectories of electrons are elongated in a magnetic field (spirals), so ionizing collisions become more likely, which lowers the breakdown strength[23].

- **Electrodes (polarity, material, roughness)**
  Theories assume that a small bubble formed near the cathode precedes the main breakdown and the breakdown occurs in the gas phase at some critical condition[24]. Details to field emission and field ionization can be found in Phillips and McClintock [25].
  Furthermore, several experiments have shown that polarity plays an important role in the breakdown phenomenon[24, 26, 27, 28]. The breakdown voltage is at its lowest when a point cathode and a plane anode are used, followed by a higher voltage when both electrodes are plane-like and finally the highest values appear when only the anode is point-like (variation of a factor of ≈ 2). The conclusion is, that the breakdown process is initiated from the cathode and triggered by field emission of electrons from the cathode.
  Material and surface condition (roughness) of the cathode influence strongly the breakdown strength but those of anode influence little. When having needle anode and plane cathode, the breakdown strength depends also on the work function of the cathode material (variation of up to a factor of 2). Copper has a high work function and therefore shows a higher breakdown voltage than e.g. aluminum.

- **Geometry**
  Size effects concerning area and volume have been observed and quantified in various works[23, 26, 27]. According to them, breakdown strength strongly depends on the overall system properties.

- **Voltage shape**
  The stressing time has influence on the breakdown voltage. Voltage pulses reach higher voltage levels without breakdown than persistent voltages applied[23, 26].

- **Leakage current**
  With natural background radiation, leakage currents or precursors to a breakdown are not measurable[20, 22, 23]. Measurable leakage currents can be caused by ionizing radiation or emission of charge carriers from the electrodes, which however needs a high local field strength of more than $10^8\,\mathrm{V/m}$[23].

Table 2.1: Selected literature values of the breakdown strength of liquid helium.

Reference	Set-up	T (K)	p (mbar)	Gap Size (mm)	Breakdown Strength (kV/mm)
[28]	stainless steel, 6 μs DC pulse	4.2	N/A	0.05	50-167
[24]	plane-plane stainless steel 6 μs DC pulse	4.2	1013	0.1	72
[23]	aluminum sphere to stainless steel plane, DC	2	32	1	22
[26]	steel spheres, DC	1.2	0.8	1	13

- **Impurities and mixtures with ^{3}He**
  Impurity particles with internal freedom may scatter electrons by inelastic collision, hence augmenting breakdown voltage. In contrast, impurities of low ionization may supply free electrons and therefore act as effective charge carrier producers[24].
  Additional ^{3}He atoms introduces small angle scattering and the motion of the electrons and ions is hindered. Therefore the recombination rate is higher and a possible current decreases[21]. This is in accordance with the already mentioned measurements of B. Sethumadhavan et al., see Figure 2.7: the bigger the fraction of ^{3}He in the mixture, the smaller the leakage current. At higher voltages, when all electron-ion pairs are separated, the values of the leakage current of different mixtures merge to one value.
  Pollution of the electrode material may assist electron injection from cathode resulting in lower breakdown strength[23, 24].

- **Statistical event**
  Breakdown is a statistical event and individual readings are often 50 % off the mean value[23] and standard deviations as high as 25 % emerge[26]. This means that for any literature values found large errors of 50 % should be assumed.

Conclusion of literature research

According to this literature research, the breakdown strength depends strongly on the conditions of the setup, i.e. the whole system considered. Therefore it is difficult to scale literature values to the AEgIS setup.
No values for the breakdown voltage under the conditions of AEgIS have been found. The conditions of Blank[26] in Table 2.1 have been the closest to ours and they have

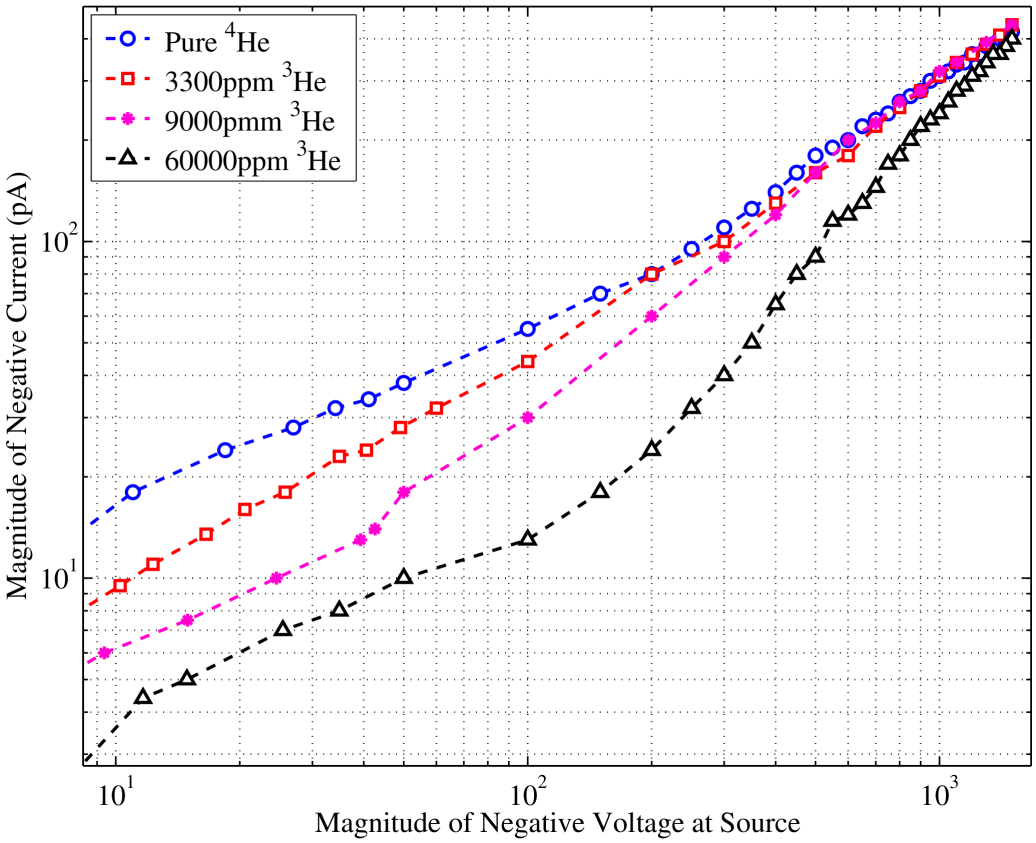

Figure 2.7: Dependence of the leakage current on the applied voltage difference between electrodes for different mixtures of helium isotopes in a certain setup. The presence of ^{3}He lowers the leakage current up to a certain voltage difference. From B. Sethumadhavan[21].

lead to a value of 13 kV/mm for the breakdown field strength. Given that our pressure is lower and that the absolute pressure dependence in the range of millibars seems to be quite strong, the breakdown strength could be significantly lower in our environment and reach a value which is critical to the setup.
According to Sethumadhavan[21], the lower temperature plays not an important role.
Technical problems arouse when measuring the leakage current and trying to avoid electrical breakdown at the same time. Apparently there is no sign whatsoever before breakdown, especially no characteristic leakage current. This also means that *any* measurement bears the risk of unintended electric breakdown.

2.4.3 Consequences of the literature research for AEgIS

Taking all these considerations into account, avoidance of electrical breakdown can a priori not be guaranteed in the rod-solution. Since breakdown bears a great probability of damaging measurement electronics it has to be avoided even in the test setup. Therefore trial and error measurements can not be conducted. Even though the thermal performance of the rod solution is about ten times better than the one of the sandwich solution (see Figure 5.16), the risk connected to the rod solution is too high for implementation in AEgIS. Therefore this solution is being discarded.

The answers to the questions stated before are:

- Electrical breakdown *can* occur in the given voltage range.
- Leakage currents in the rage of several 100 pA have to be expected under the radiation environment of AEgIS, depending on the ionizing radiation level. Disadvantageously, this current will not carry any information of a possible imminent breakdown.

Nevertheless, *if* measurements on this issue will be done in the future, the following points should be considered:

- To reduce the risk of electrical breakdown, one could insert thin electrical insulant (e.g. Kapton® foil) at the critical points of the setup (edges and spikes). This would elongate the effective distance between two electrodes.
- Alternatively/additionally, one could adapt the test setup so that the electronics can bare breakdowns. However, the effects of electrical breakdown in the mixing

chamber on the dilution refrigerator are yet unknown. Damage of hardware other than electronics can not be excluded.

- The radiation in the final setup has to be simulated in the test setup. Issues of implementation (contamination etc.) and reproduction of the real radiation environment (γ radiation) have to be thoroughly deliberated before.

2.5 The sandwich solution

Since the rod-solution has been estimated too risky for AEgIS, the sandwich-solution is tested for its suitability for AEgIS.

Like above, the electrodes are mounted on the surface of the mixing chamber lid. The difference to the rod-solution is that the electrical insulation and thermal contact is both realized at the very same place, i.e. in a layer between the electrodes and the mixing chamber lid. Therefore, the material constituting this layer has to insulate electrically and has to transfer heat well at 100 mK. Unfortunately, good heat conductivity of a material is normally directly connected to good electrical conductivity since both are mainly accomplished by the material's freely moveable electrons. This means that an electrical insulator (with no "free" electrons available) has to resort to other mechanism for heat transfer. In solid materials phonons provide such a mechanism. However, the capability of phonons to conduct heat is orders of magnitude lower than the one of electrons, so solid insulators are in general poor heat conductors. In addition, a boundary between two dissimilar materials acts as an obstacle for phonons and can significantly reduce heat transfer over such a contact when only phonons are available.
A material, which is known to conduct heat relatively well at low temperatures and insulate electrically at the same time, is sapphire. Above 20 K, it conducts heat even better than metals, but it loses this feature when approaching lower temperatures. Below 1 K, the value decreases by a factor of more than 10^4, but still stays larger than the values for other comparable dielectrics. That's why sapphire will be used here. Furthermore, the limiting factor of heat transfer is not the bulk sapphire, but the contact metal-dielectric. In the presented work, an optimization of this contact is done for AEgIS.
The layer between the electrodes and the mixing chamber lit will be a sapphire disk, whose surfaces are treated to improve thermal contact to the copper surfaces. Work of Schmidt and Umlauf[5] suggests that indium layers between the disk and the copper improves the contact. The method of applying indium as well as the surface roughness

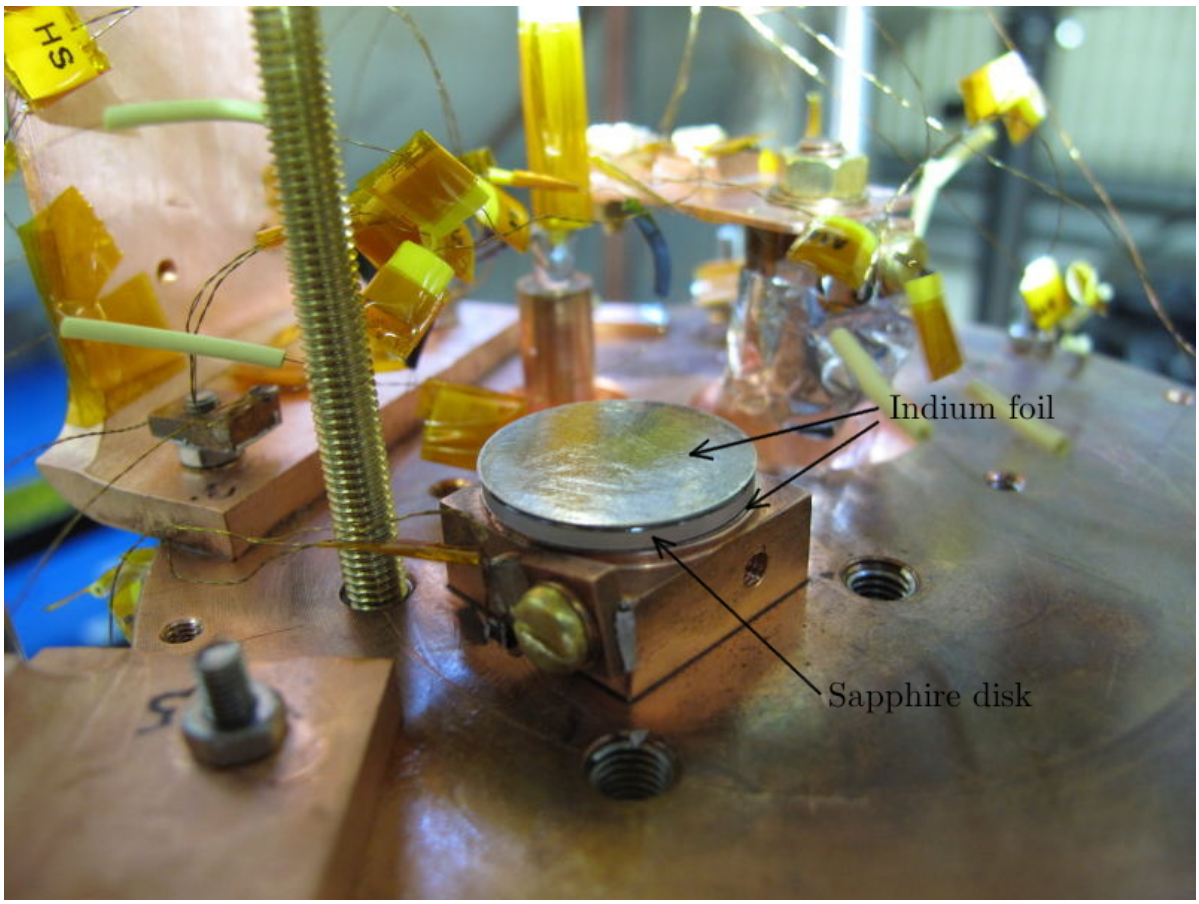

Figure 2.8: The top lid of the mixing chamber of the test setup. The sandwich is already in place (round structure in the middle). The layers of the sandwich are visible: the sapphire disk (gray) is placed on a thin indium foil. On the top of the disk, another indium foil is placed. The top copper stamp which presses the sandwich is not mounted in this picture.

of the sapphire influence the ability to conduct heat. For AEgIS two different types of sapphire disks are investigated: rough sapphire and optically polished sapphire. Between the sapphire and the copper thin indium films are placed. The influence of additionally applying an indium coating on the sapphire by physical vapor deposition (PVD) is also investigated. Altogether, four different sandwiches are compared:

- sandwich A: rough sapphire disk with indium sheets
- sandwich B: polished sapphire disk with indium sheets
- sandwich C: polished sapphire disk with indium sheets and PVD-indium
- sandwich D: rough sapphire disk with indium sheets and PVD-indium

2.6 Operational heatloads on the cold part

The central part of AEgIS is cooled to $\approx 100\,\mathrm{mK}$. The surrounding environment will be at higher temperatures, acting as a heatload on the cold part. Two different kinds of hatloads can be identified during operation of AEgIS: First, constant ones coming from the continuously operating parts of AEgIS and second, intermittent heatloads caused by the periodic creation of antihydrogen.

2.6.1 Constant heatloads

Constant heatloads come from residuals, thermal conduction (mountings) and thermal radiation. Residual heatloads are caused by subsystems of a material/setup which release their heat slowly due to very long low-temperature relaxation times[3]. Heatloads from convective heat transfer are avoided by the vacuum environment of the setup.
Estimations of values for the constant heatloads acting on the cold part are subject of current studies. The specifications of the future dilution refrigerator for AEgIS foresee its cooling power to $\approx 100\,\mu\mathrm{W}$ at a mixing chamber temperature of 50 mK. All heatloads on the cold part will have to be transferred via the dilution refrigerator, so they must not excess $100\,\mu\mathrm{W}$.
The static measurements presented in this work will give a preliminary estimation about the amount of heatloads, which can be transferred from the electrodes of the central part through the sandwich to the mixing chamber.

2.6.2 Pulsed heatloads

AEgIS will produce antihydrogen in an intermittend way with a period of about 120 s, causing a periodic heatload during the pulsed creation of antihydrogen. The major part of them will stem from annihilation of matter and antimatter. Estimations of this heatload predict an input of $10\,\mu\mathrm{J}$[9] during a time of $1\,\mu\mathrm{s}$. If this energy is equally distributed on all the electrodes, their temperature will rise from 100 mK to about 130 mK[29]. There are two questions to be answered:

- Which type of sandwich transfers the deposited energy fastest to the mixing chamber?
- Will the low operating temperature of the electrodes be reached again in a short enough time span, i.e. significantly below 120 s?

The dynamic measurements are conducted to get an answer to the first question and the step measurements clarify the second question.

3 Theory

This work deals with thermal measurements at ultra low temperatures between 30 and 130 mK. Thermal properties at these extreme temperatures are discussed in this chapter as well as the distillation of important physical quantities out of temperature measurements

3.1 Thermal conductivity at low temperatures

Thermal conductivity in solids is achieved by motion of particles carrying a certain amount of energy. These particles normally can not travel freely in the solid but are scattered by different mechanisms. This is a typical diffusion process and can therefore be described by the kinetic gas theory. Doing so, the thermal conductivity κ can be calculated by

$$\kappa = \frac{1}{3} c\, v\, \lambda \ , \tag{3.1}$$

where c is the material's specific heat, v is the velocity of the particles and λ their mean free path[3]. To determine the temperature dependence of κ, we have to distinguish between the different types of particles contributing to the process of heat transfer.

3.1.1 Phonons as energy carriers (dielectrics)

In dielectric solids (i.e. no conduction electrons availabe) phonons are the only energy carriers available for heat transfer. They travel with the speed of sound, which at low temperatures is independent of the temperature T. The dependence of the specific heat on T at low temperatures is evaluated via the Debye-model and is found to be $\propto T^3$ [30]. At low temperatures only a small part of the phonon spectrum can be excited. Therefore the phonon density is low and phonon-phonon scattering can be neglected. Furthermore, the wavelength of the emerging phonons is typically large compared to lattice defects, so phonon-defect scattering is not important either. As a consequence, the mean free path of the phonons is determined by grain boundaries, which in a monocrystal are the

same as the macroscopic borders of the crystal. Therefore λ_{ph} is not dependent on T and we get a final temperature dependence of the thermal conductivity of

$$\kappa_{ph} \propto c_{ph} \propto T^3 \ . \tag{3.2}$$

3.1.2 Electrons as energy carriers (metals)

In metals also electrons are available for the transfer of heat. More exactly, the conduction electrons can move around the solid. The characteristic velocity is the Fermi velocity, which is temperature independent.
The heat capacity c_e in metals is dependent on T, but the Debye-model is not applicable on electrons. Electrons are fermions and therefore follow the Fermi-Dirac distribution, where the theory yields $c_e \propto T$.
As said above, phonon scattering is no issue at low temperatures any more. Electron-electron scattering is also negligible due to the electrons' fermionic nature. Therefore, λ_e is determined by lattice defects and impurities and hence not dependent on the temperature. This together results in

$$\kappa_e \propto c_e \propto T \ . \tag{3.3}$$

3.1.3 Comparison metal-dielectric

The speed of sound in solids is in the range of several 10^3 m/s whereas the Fermi velocity is typically between 10^5 and 10^6 m/s. That's why metals have in general a higher thermal conductivity than dielectrics. In addition, the contributions from phonons and electrons are additive, so metals have two mechanisms of heat transfer whereas dielectrics only have one. At very low temperatures the temperature dependencies stated above are valid, resulting in differences of κ of up to several orders of magnitude, see Figure 3.1.

3.2 Kapitza resistance

In 1941, P. Kapitza was the first to observe the thermal resistance of an interface between a metal and He II[31]. About ten years later, I. M. Khalatnikov[32] provided a first theory to this phenomenon, describing phonon transmission through a liquid-solid interface. This theory is called acoustic mismatch theory.
Phonons travel with the speed of sound. In analogy to optics, Snell's law can be applied

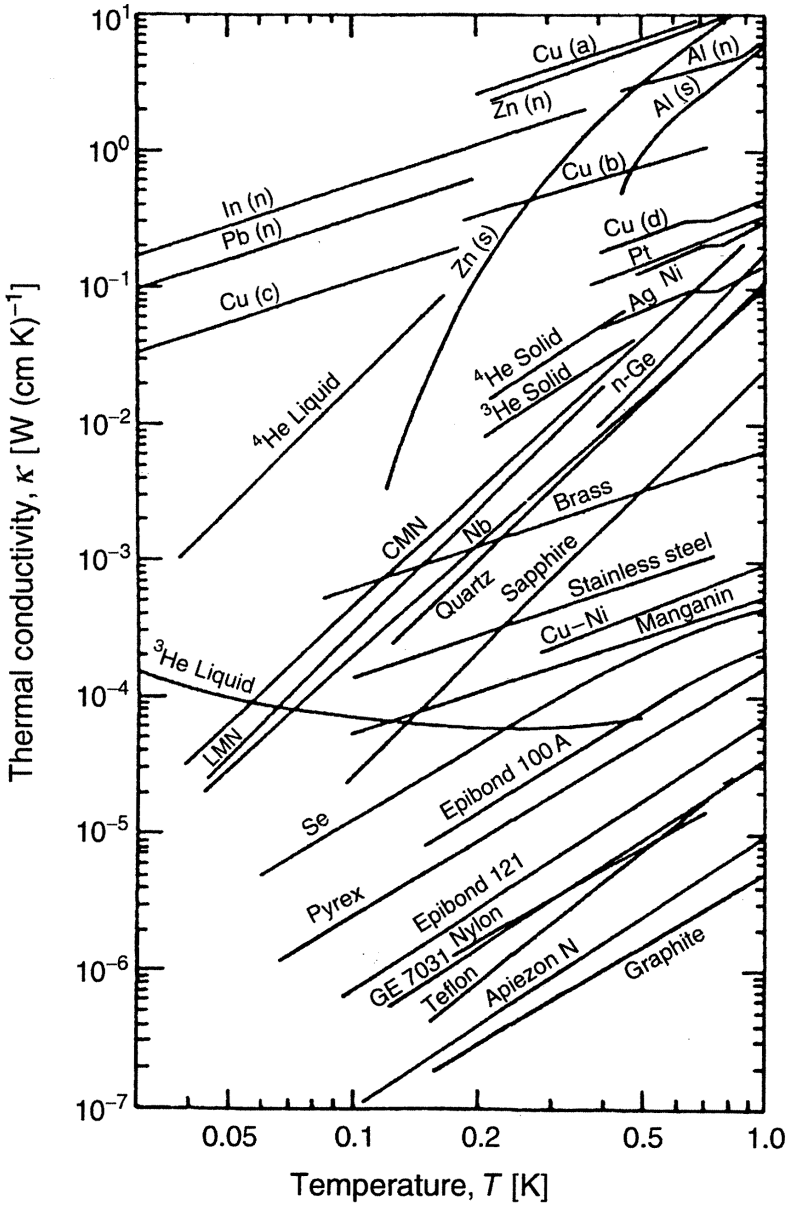

Figure 3.1: Thermal conductivity κ in dependence of temperature for various materials. From[3].

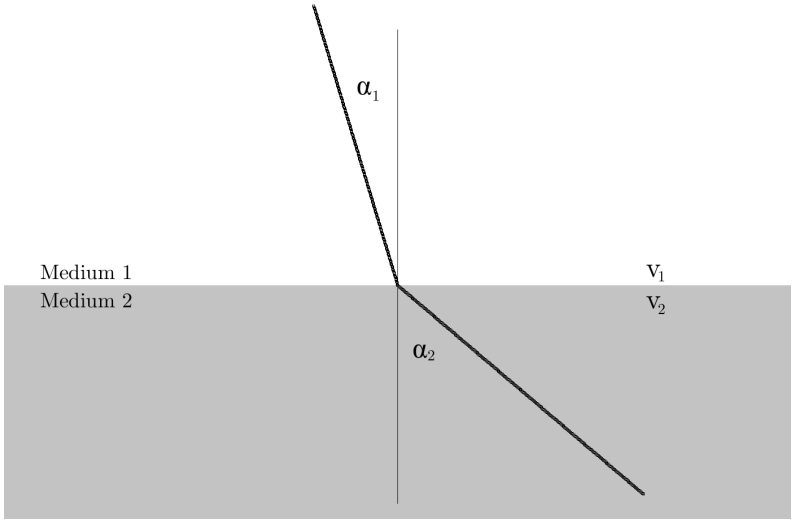

Figure 3.2: Illustration of Snell's law. The two media have different speeds of sound, therefore diffraction occurs. α . . . angle of the incident/refracted phonon, v . . . speed of sound for the medium

when phonons travel from one medium to another[3]:

$$\frac{\sin\alpha_1}{\sin\alpha_2} = \frac{v_1}{v_2} \,, \tag{3.4}$$

where α_1 and α_2 are the angle of incident and refracted phonon paths and v_1 and v_2 the speeds of sound in the respective medium, see Figure 3.2.

Like in optics, total reflection can occur. If the first medium is helium, v_1 is 238 m/s[3]. Having a metal as the second medium, v_2 is in the order of 3×10^3 to 5×10^3 m/s. With these values the critical angle is about 3 °. From all the phonons hitting the interface, only the ones coming from the helium within a cone with this small apex angle can enter the metal. Calculating the ratio of the solid angle of the cone to the whole hemisphere gives the fraction of phonons able to enter the solid. Taking the values from above, it is about 10^{-3}. But even not all phonons from this small fraction are transmitted due to the difference of the acoustic impedances. The acoustic impedance Z of a material is defined as $Z = \rho v$, where ρ is the density. The transmission coefficient k_t for phonons depends on the acoustic impedances of the materials and is given by[3]

$$k_t = \frac{4Z_1Z_2}{(Z_1+Z_2)^2} \approx \frac{4Z_1}{Z_2} = \frac{4\rho_1 v_1}{\rho_2 v_2} \,. \tag{3.5}$$

For helium-metal contacts k_t is is about 10^{-3}. Multiplying the two factors gives a

value of 10^-6. Only this very little fraction of all phonons available can contribute to transmission and therefore a rather high value of thermal resistance for such interfaces is observed.

Taking these explanations into account and having the energy density of photons at a temperature T given as[30]

$$\frac{\pi^2 k_B^4 T^4}{30\hbar^3 v_1^3} \,, \tag{3.6}$$

the energy flux $\dot{Q}$ through a surface A is

$$\dot{Q} = \frac{\pi^2 k_B^4 \rho_1 v_1}{30\hbar^3 \rho_2 v_2^3} A T^4 \,, \tag{3.7}$$

where k_B is the Stefan-Boltzmann constant and $\hbar$ the Planck constant. When the temperature difference ΔT is small compared to T, $\dot{Q}$ can be expressed as

$$\dot{Q} = \frac{d\dot{Q}}{dT}\Delta T = \frac{2\pi^2 k_B^4 \rho_1 v_1}{15\hbar^3 \rho_2 v_2^3} A T^3 \Delta T \,. \tag{3.8}$$

The Kapitza resistance R_K is defined as[33]

$$R_K = \frac{A\Delta T}{\dot{Q}} \,. \tag{3.9}$$

This definition combined with (3.8) yields

$$R_K = \frac{15\hbar^3 \rho_2 v_2^3}{2\pi^2 k_B^4 \rho_1 v_1} \frac{1}{T^3} \,. \tag{3.10}$$

The T^{-3}-dependence is an important result. It was derived for an interface between liquid helium and a solid, having only phonons as heat carrier. As shown in the next section, it is also valid for solid-solid interfaces. For good heat transfer at low temperatures it poses a big problem, since the resistance rises drastically towards very low temperatures.

Finally it should be mentioned, that the name “Kapitza resistance” is badly chosen, but common in literature. Actually it should be named Kapitza *resistivity*, since the surface area is included in its definition.

3.3 Thermal boundary resistance

The Kapitza resistance was first observed on liquid helium-solid interfaces, but this phenomenon arises also between solid-solid interfaces. To avoid confusion, this resistance is subsequentially called thermal boundary resistance R_{TB}. Theoretical descriptions use the same acoustic mismatch model as above[34], yielding a T^{-3}-dependence for R_{TB} like the Kapitza resistance. However, at solid-solid interfaces surface effects play a major role in the ability of the contact to transfer heat. Impurities, oxidation, the microscopic structure (surface roughness), and many other factors have to be considered. Swartz and Pohl[4] give a detailed overview of measurements and theory developments done since the first application of the phenomenon to solid-solid interfaces by Little.

As mentioned in section 2.5, Schmidt and Umlauf have investigated the thermal boundary resistance for indium-sapphire contacts[5]. They have observed a temperature dependence of T^{-n} with n always being smaller but close to three. They have explained the difference to the value 3 by the quality of the contact, stating that the condition of an ideal boundary had never been fulfilled.
In literature it is common to graph the thermal boundary resistance as $R_{TB}T^3$, see Figure 3.3. According to the theory, a perfect contact has a T^{-3}-dependence and therefore yields a horizontal line in this graph.

Like the Kapitza resistance, the thermal boundary resistance should actually be called thermal boundary *resistivity*.

3.4 Thermal radiation

The radiative heat flow from a surface A at the temperature T is given by the Stefan-Boltzmann equation

$$\dot{Q} = \sigma \epsilon A T^4 \ . \tag{3.11}$$

σ is the Stefan-Boltzmann constant and ϵ the emissivity of the surface. Having two surfaces at the temperatures T_1 and T_2, respectively, the heat exchange between these surfaces is given by

$$\dot{Q} = \sigma E \tilde{A} \left(T_1^4 - T_2^4 \right) \ , \tag{3.12}$$

where E is a factor depending on the two emissivities of the surfaces and $\tilde{A}$ a geometric factor.

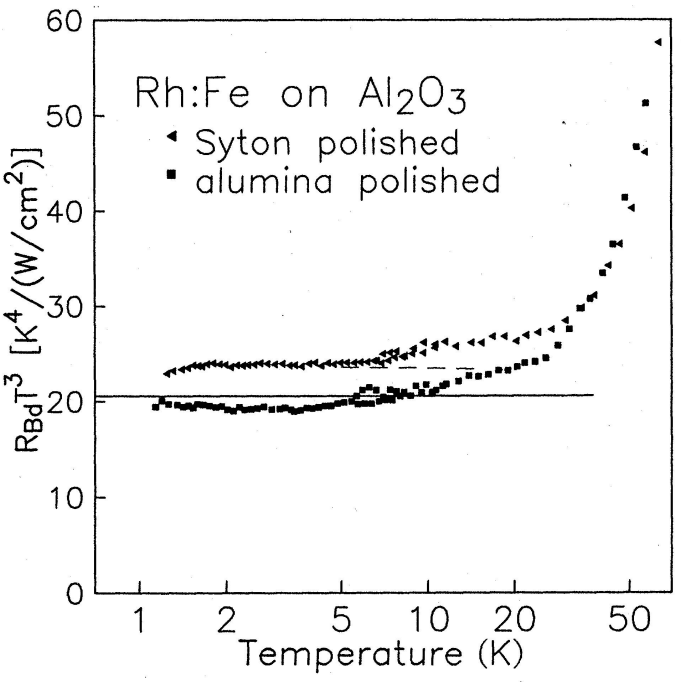

Figure 3.3: Typical plot of the thermal boundary resistance $R_{TB}T^3$ against temperature [35]. The horizontal lines represent predictions from theoretical models.

3.5 Thermal measurements

3.5.1 Theory of static measurements

The power transferred via phonons between two different media over a given surface A is

$$\dot{Q} = \frac{A}{4R_{TB}} \left(T_1^4 - T_2^4\right) \ , \tag{3.13}$$

with T_1 and T_2 being the temperature on either side of the thermal contact[36]. The thermal boundary resistivity can therefore be calculated out of the transferred heat, the area of the contact and the temperatures on both sides:

$$R_{BR} = \frac{A}{4\dot{Q}} \left(T_1^4 - T_2^4\right) \ . \tag{3.14}$$

The similarity of equation (3.13) to power transferred via radiation, equation (3.12), is due to the same bosonic nature of phonons and photons.

3.5.2 Theory of dynamic measurements

Heat distribution in a material is theoretically described by the heat equation[37]

$$\frac{\partial T}{\partial t} - \alpha \vec{\nabla}^2 T = 0 \ , \tag{3.15}$$

where T is the temperature, t the time, α the thermal diffusivity and $\vec{\nabla}$ the nabla operator. In a homogeneous, isotropic medium α is a scalar.
A temperature variation at one place in a bulk material will travel through the material over time. The physical material property describing especially the speed of this propagation is α. Since the speed of heat transfer through the sandwiches is important to know, α is measured in this work. It determines, how fast a given heat input on one side of the sandwich can be transferred through the sandwich to a colder region.
If the material has favorable geometry, simple formulas exist to calculate α out of a temperature measurement. When a semi-infinite rod is heated periodically at its end, the temperature variation will travel as a heat wave along this rod. If the temperature at the end of the rod is sinusoidal, then the temperature variation at some given distance to the end will also be sinusoidal, but with different amplitude and phase as shown in Figure 3.4. The thermal diffusivity can be calculated from the amplitude attenuation or phase shift of the oscillation[38]:

$$\alpha = \frac{d^2 \pi \nu}{(\Delta\phi)^2} \ , \tag{3.16}$$

$$\alpha = \frac{d^2 \pi \nu}{\ln \frac{A_1}{A_2}} \ , \tag{3.17}$$

where d is the distance, where the altered temperature variation is measured, ν the frequency of the oscillation, $\Delta\phi$ the phase shift of the oscillation and A_1 and A_2 the original and the attenuated amplitude, respectively.

Unfortunately the setup of the measurements on the sandwiches can not be described as a semi-infinite rod. First of all the geometry is different and the rod is finite. Second, one end of the rod is thermalized at a constant temperature, so applied temperature variations can not travel freely to infinity. Therefore, α can not be calculated by the simple formulas mentioned above. Still, the phase shift and amplitude attenuation of a temperature oscillation can be used to determine α even for the sandwiches. However, this has to be done by a computer simulation, see section 5.2.5.

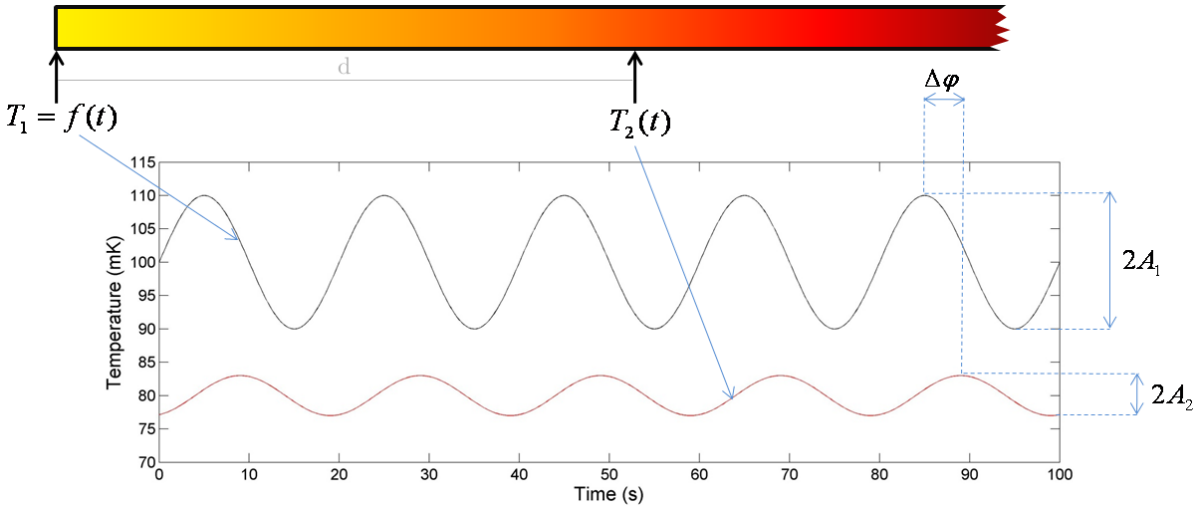

Figure 3.4: Illustration of the dynamic measurement theory. The given temperature variation over time, $T_1 = f(t)$, travels along the semi-infinite rod and is detected modified at a distance d as $T_2(t)$. The thermal diffusivity α can be calculated from the phase shift $\Delta\varphi$ or the two amplitudes A_1 and A_2.

A very important simplification is made concerning the thermal diffusivity of the sandwich. As stated above, α is a material property. It is connected to various other important physical properties via[37]

$$\alpha = \frac{\kappa}{\rho \cdot c} \,, \tag{3.18}$$

where κ is the thermal conductivity, ρ the density and c the specific heat capacity of the material. So the thermal diffusivity for a sandwich made up of layers of different materials is actually not defined. To point this issue out, the symbol α^* will be subsequentially used for the thermal diffusivity. So when measuring α^* for the sandwich, it implies the simplification of treating the sandwich as a bulk homogeneous and isotropic material. Therefore, the derived α^* can *only* be used for a sandwich with exactly the same layer geometry using the exact same materials.

4 Experimental setup

This chapter contains details of materials and instrumentation used in the test setup, as well as of how the measurement setup is assembled. Also the cooling to ultra low temperatures with a dilution refrigerator is explained.

4.1 The sandwich and its mounting

As said before, the sandwich is made of a sapphire disk with sheets of indium on each side, pressed between copper pieces, see Figure 4.1. The lower copper piece is part of the mixing chamber lid, like it will be in the future AEgIS setup. The upper piece is like a "stamp", by which the sandwich is pressed together. The contact surfaces of the copper pieces are circular with a diameter of 20 mm, fitting exactly the sapphire disk.

When mounted for measurements, the upper copper piece is pressed down on the sandwich by the force of four tightened brass nuts, which pull on threaded bronze rods attached to the mixing chamber as shown in Figure 4.2 and 4.3. Apart from the sandwich, any thermal contact from the upper copper piece to the mixing chamber has to be minimized in order to not influence the measurement. This is achieved by a special construction: directly on the copper stamp 20 thin sheets of G-10, a glass fiber-reinforced epoxy laminate are installed. Each interface between the layers acts as a high thermal contact resistance. On top of those rings, a tube of stainless steel is placed. Stainless steel has a fairly poor thermal conductivity at low temperatures so this tube acts both as thermal insulation and force transmitter. The actual force from the nuts is applied on a stainless steel lid sitting on the tube. There again, several layers of G-10 are put between the nuts and the lid. The use of many different materials is an issue regarding the overall thermal contraction when cooling down form room temperature to cryogenic temperatures. The rods where the nuts pull are chosen to be bronze, since bronze has a larger linear thermal contraction than copper and stainless steel [39, p. 601]. Therefore, the contraction will tighten the clamping instead of loosening it. As a precaution belleville

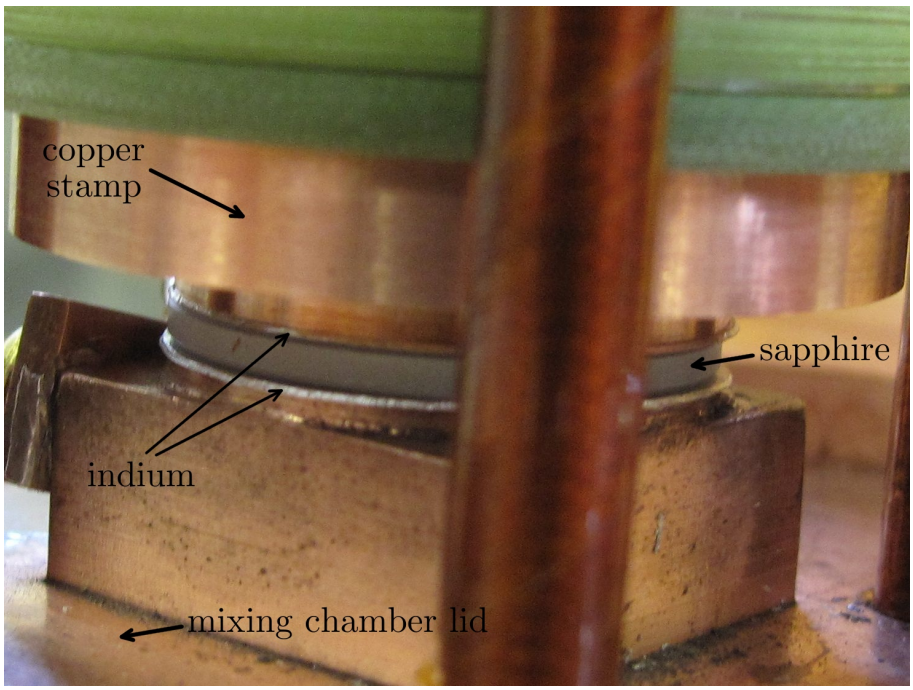

Figure 4.1: Mounted sandwich pressed together. The different layers of the sandwich are visible.

washers are put underneath the nuts. These washers act like springs and if the soft indium slackens because of the pressure, they keep up the force.
To avoid thermal shortcut, the bronze rods are covered by a layer of Kapton® and the stainless steel ring is kept in place by fits in the lid as well as additional G-10 rings around it.
Any copper pieces in the setup (including the parts of the dilution refrigerator) have been machined in the workshop of the cryolab. The copper used is oxygen-free high thermal conductivity (OFHC) copper. The very high purity of OFHC copper improves the copper's properties, especially its thermal conductivity.

Preparation and mounting of the sandwiches is a task, which needs to be done very carefully. The thermal contact of the sandwich is governed by its interfaces and is strongly influenced by the surface conditions of the different layers. Therefore any carelessness in preparation can tamper with the results. All surfaces have to be prepared and cleaned thoroughly:

- The bottom copper piece is part of the mixing chamber and can not be taken off. It therefore has to be cleaned directly on the spot.

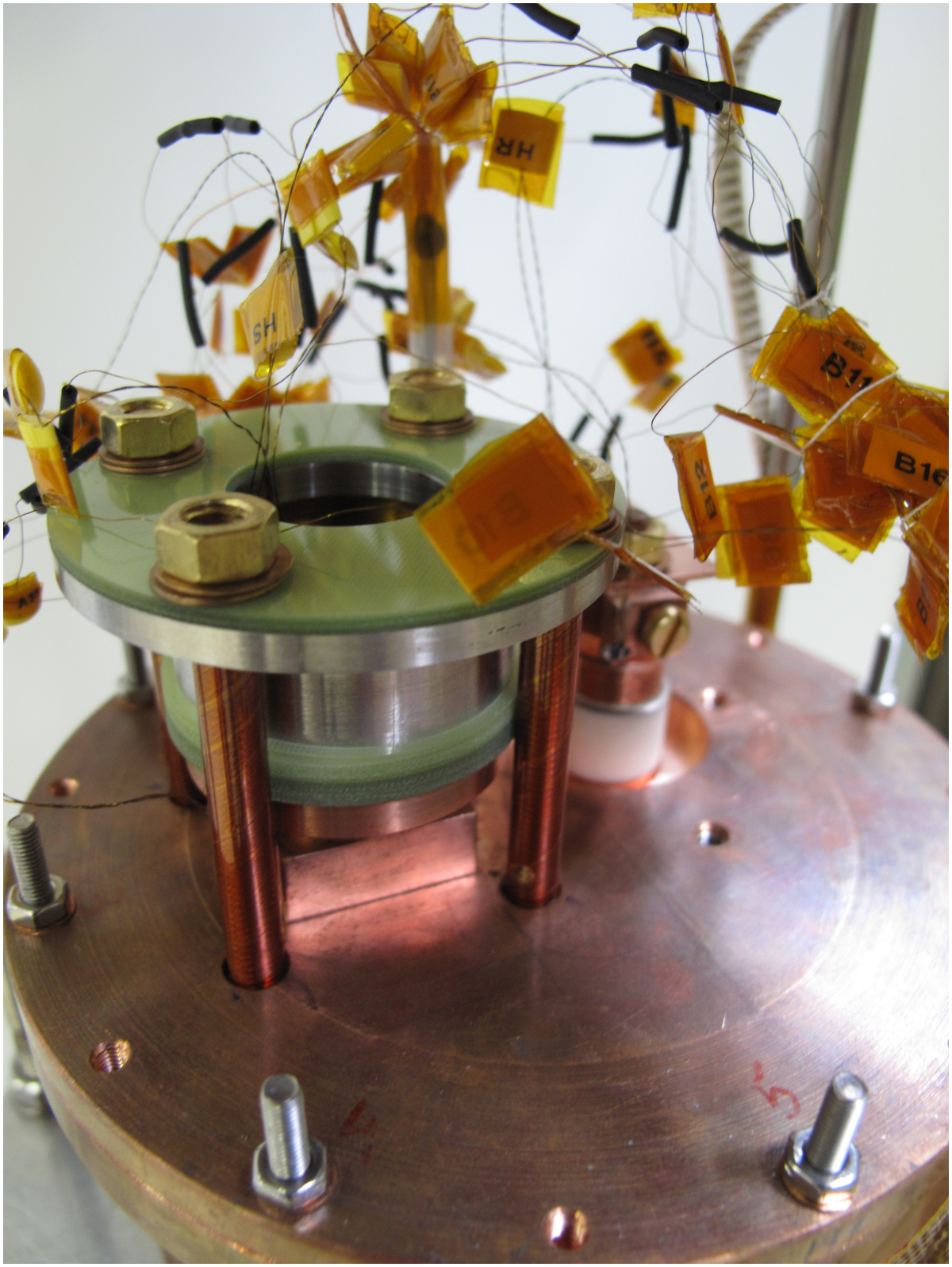

Figure 4.2: The mounting of the sandwich on the mixing chamber.

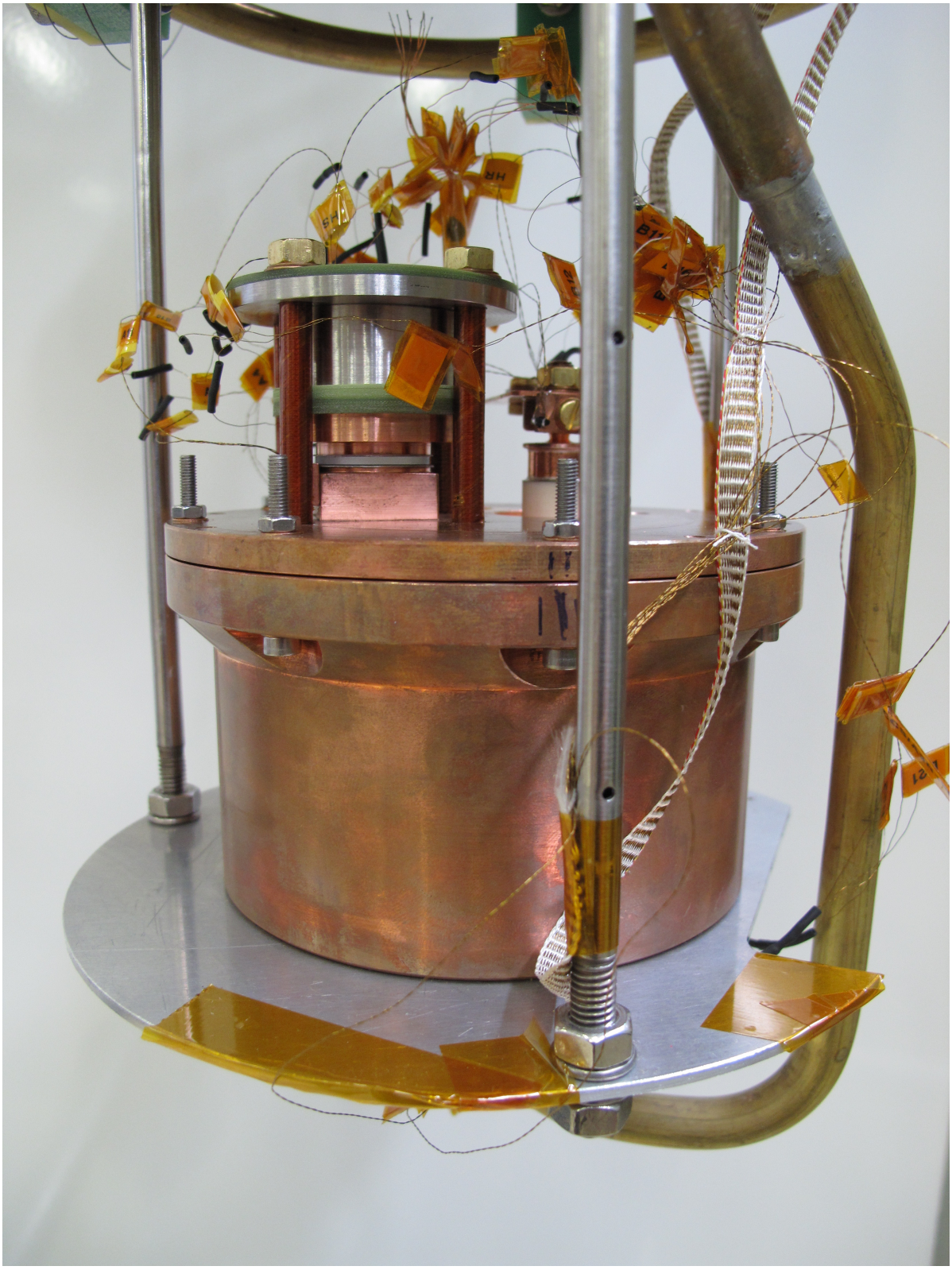

Figure 4.3: Mounted sandwich on the mixing chamber. Work on the sandwich and mixing chamber has to be done carefully, since no wires nor any other parts of the mixing chamber should be damaged.

- The indium foils have to be punched out and cleaned. The handling of them is not easy due to their thinness of 125 μm and 250 μm.
- The sapphire discs have to be cleaned. The PVD disks are treated specially, see below.
- The top copper part (stamp) has to be cleaned. Temperature sensors and a heater are attached to it, so it has to be handled with special care. The sensors, the heater and the attached cables shouldn't be damaged.
- All parts for the mounting and pressing of the sandwich have to be prepared.

The cleaning is done with ethanol to avoid any residue. Disposable gloves are used whenever the indium foils or the sapphire disk have to be touched.
When all the parts are ready for assembly, the sandwich has to be built. The first layer of indium foil is placed on the bottom copper part on the mixing chamber. Then the sapphire disk is placed on it, followed by the second layer of indium. The sandwich at this stage is shown in Figure 2.8. Finally the top copper stamp is placed on the sandwich. All parts have to be centered accurately. Once this is done the rest of the clamping equipment has to be put in place, involving all the parts described before. The tightening of the nuts has to be done exactly the same way for each sandwich to ensure that the same force is applied on every sandwich. The four nuts are carefully tightened with a torque wrench, going stepwise up to 1.6 Nm. Since the indium is pressed together to its yield strength it gives way and creeps to a certain extent out of the lateral sides of the sandwich. This creeping is happening very slowly, so the nuts are tightenend over several days to ensure enough pressure and therefore good contact.
The creeping of indium can cause problems when the indium foil is chosen inappropriately. If the indium foil is too thick the indium might creep so far outside the sandwich, that the foils from the top and bottom part touch each other and create a thermal shortcut, see Figure 4.4. During this work, this happened once and several weeks of measurements on one sandwich had to be redone. After this incident a thinner indium foil has been used, successfully avoidind thermal shortcut.
Any work done on the mixing chamber has to be done very carefully. The mixing chamber is the central part of the dilution refrigerator and houses many crucial gaskets, joints and cable feedthroughs as shown in Figure 4.3. Any damage done to one of these parts might result in problems during the measurement or even in malfunction of the dilution refrigerator. During operation the inner parts of the dilution refrigerator are not

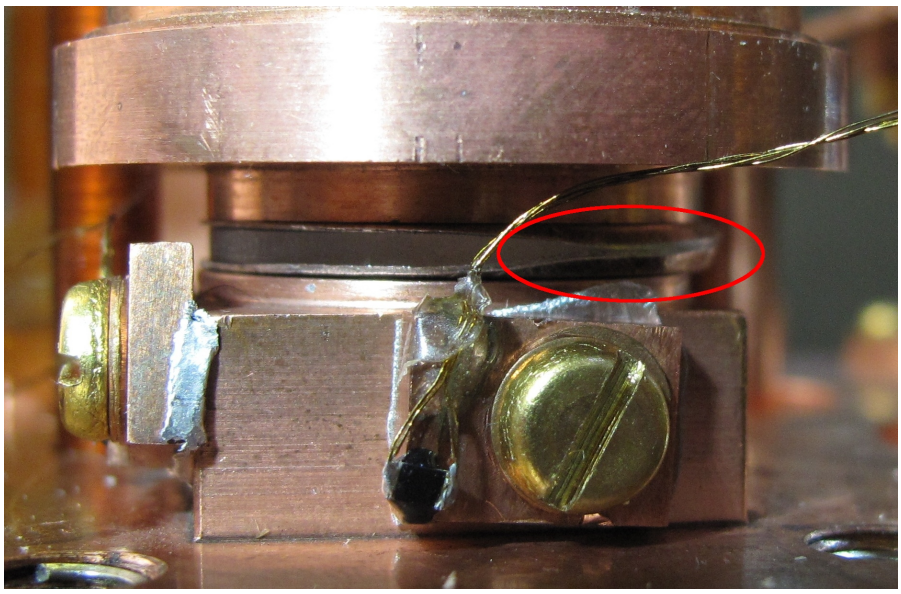

Figure 4.4: Sandwich showing the thermal shortcut (red circle). The indium foils have been pressed out due to the high ductility of indium.

accessible, so any repairs would involve the warming up and dismounting of the whole refrigerator. This is also why extensive precautions are made before placing the refrigerator in the cryostat: leak tests, checking of electric contacts and prudence while handling any hardware are time consuming but necessary. The preparation of the refrigerator for measurements takes at least two weeks.

4.1.1 The sapphire disks

The sapphire disks for all measurements have a thickness of (1.5±0.01) mm and a diameter of (20±0.01) mm. Their purity is 99.99 %, according to the manufacturer Djeva SA[40]. Two different types of disks are used, rough and polished ones. Surface measurements yielded maximum heights of the profile of (10±3) μm for the rough sapphire and (21±14) nm for the polished one.

4.1.2 The indium layer

On each sandwich, indium is applied by putting indium foil between the sapphire disk and the copper. The foils have the same size as the disks, being circular and having a diameter of 20 mm. They are punched from indium sheets with an estimated uncertainty of ±0.3 mm. Two different foils are used, one being 125 μm thick, the other 250 μm.

Uncertainties for the thickness are not provided by the retailer[41]. The purity is stated to be 99.99 %.
Some sapphire disks are specially surface treated. Their faces are coated with a thin film of indium, applied by physical vapor deposition (PVD). This is done by the thin film and glass laboratory at CERN. They use indium with a purity of 99.9999 %. One vapor deposited layer has been measured to be (3.5±0.2) μm thick. However, the evaporation conditions have been different for some disks and the estimation of the thin film and glass lab for the thickness is 2 μm. The actual thickness of the coatings is estimated to be between 2 and 4 μm.

4.2 Instrumentation

The measurements involve very low signals, so the instrumentation plays an important role. Sensors need to be calibrated well, cables and electronics need to be shielded against radio frequency (RF) capture and the readout electronics has to be reliable and accurate. The whole instrumentation had been built and taken care of before this work was started. Still, operation of it requires knowledge about its structure and functionality.

4.2.1 Sensors and heaters

For the whole dilution refrigerator system many sensors are used, which monitor mainly temperatures, pressures and massflows. Furthermore, simple ohmic heaters are used to regulate temperatures at various places in the apparatus. This section focuses on the temperature sensors and heater used directly during the measurements.
For every sensor and heater, 4-wire sensing is implemented to improve the accuracy of the measurements.

Overview of the sensors

Figure 4.5 shows the test setup with the temperature sensors attached. They are all glued to a small piece of copper, which is then screwed to the relevant part of the setup, using indium for thermal contact. The two temperature sensors not visible in the image are the ones in the mixing chamber, measuring the temperature of the heat exchanger and ^{3}He-^{4}He mixture, respectively. In Table 4.1 all relevant sensors for the measurements are listed.

All sensors are resistive thermal devices (RTDs) using thick film technology. The resistive layer is a film of ruthenium oxide (RuO_2).

Table 4.1: Sensors used for the measurements.

position	sensors	temperature labeling
top of sandwich	R1 and S1	T_1
bottom of sandwich	R2 and S2	T_2
mixing chamber (heat exchanger)	SC3	T_{SC3}
mixing chamber (^{3}He-^{4}He mixture)	LS	T_{LS}

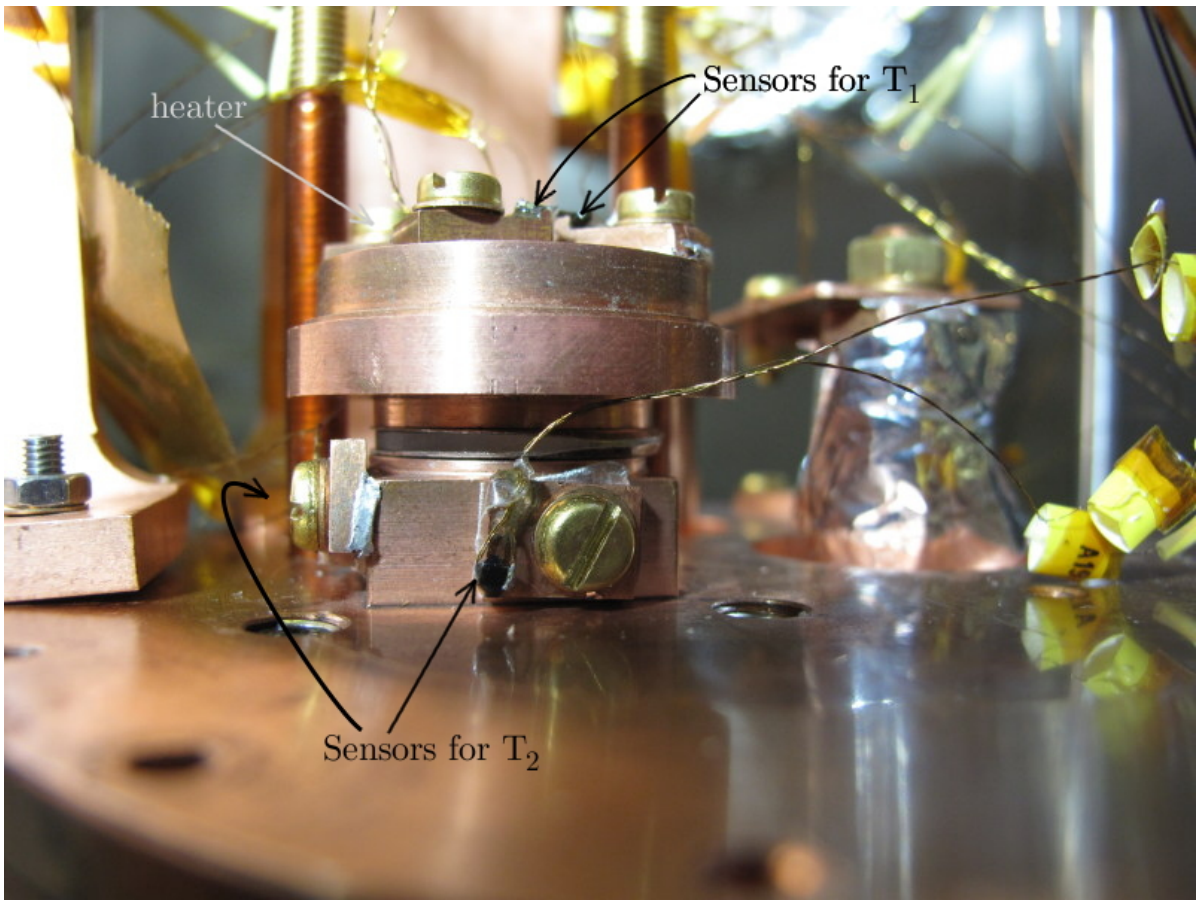

Figure 4.5: Test setup with the temperature sensors visible.

Calibrated LakeShore sensor LS

The most accurate sensor is the sensor placed in the mixing chamber measuring the temperature of the ^{3}He-^{4}He mixture, T_{LS}. It is the RX-202A model from LakeShore, having a resistance of 2 kΩ at room temperature. It is pre-calibrated, i.e. the calibration has been performed by the manufacturer. The specifications of this sensor include good radiation resistance and low magnetic field-induced errors[42]. In the temperature range used, its error is ±3 mK[43].

Ruthenium oxide sensors

Although the LakeShore sensor is also a ruthenium oxide sensor, the others are referred to as "the ruthenium oxide sensors". The difference is that they have been thermally cycled and calibrated in the cryolab and not by the manufacturer. The calibration has been done using T_{LS} as temperature reference. The overall error is estimated to ±5 mK when used below 70 mK and ±6 mK above 70 mK[43].
They are all from the RCWP0575-2K00-FKWB type, manufactured by Vishay/Dale. Their resistance at room temperature is 2 kΩ.

Heater

The heater is a ohmic heater attached at the stamp like R1 and S1. The maximum heating power used for the measurements is about 3.5 μW.

4.2.2 Electronics

Two electronic module racks house different power supplies and the devices for controlling and for signal readout, see Figure 4.11. Many of the devices serve the operation of the dilution refrigerator (pressure gauge readout, heaters, controlling of valves, etc.). For the measurements, the most relevant devices are the resistant bridges AVS-47A and AVS-47B by PICOWATT. They measure the resistances of the RTDs and their reliability is therefore necessary for any thermal measurements performed.
AVS-47A is mainly used for the temperature sensor LS in the mixing chamber. Together with the temperature controller TS-530A (also from PICOWATT) it controls the temperature in the mixing chamber. AVS-47B is used for RuO_2-sensors, i.e. all sensors used for the measurements except LS. The resistant bridges can only measure one channel at a time.

Together with other sensitive electronics, the above mentioned devices are mounted in the shielded rack. Shielded means that extensive precautions have been taken to make the signals robust against disturbances from RF. It includes common grounding of any metallic parts, additionally applied shielding and avoiding structures which might act as a RF antenna. Also the measuring wires to the dilution refrigerator as well as the dilution refrigerator itself have been designed in this way and recent adaptions have even improved the shielding.
In addition to the electronics mounted in the racks there exist two amplifier boxes, which sit directly on the dilution refrigerator. They pre-amplify the very low signals coming from the temperature sensors and are therefore placed as close as possible to the measuring sites. They are very well shielded by metal boxes.

A complete list of the electronic devices in the racks and their uses is shown in table 4.2. Various bus hubs and a controller are used to send the data collected by the electronics to the computer via GPIB (General Purpose Interface Bus).

4.2.3 Data acquisition and controlling software

All data are sent to a computer, where they are saved and processed. The existing LabVIEW® program controls the data collecting and saves the raw data to a file. In addition, it converts collected data into the desired quantities like temperature or pressure. These values and their previous developing are shown in realtime on the graphical user interface (GUI) of the program.
With the exception of some settings for the temperature controller TS-530A, all variables for controlling the refrigerator and the measurements are set via the program. Some of them are preset, some of them have to be regulated manually and some are automatically controlled. The program includes an automatic monitoring & alarm system for the operation of the dilution refrigerator. A sample screensshot from the GUI is given in Figure 4.6.

Table 4.2: Electronic devices used for the measurements.

device name	shielded rack	use
PICOWATT AVS-47A resistance bridge	yes	readout temperature sensors
PICOWATT AVS-47B resistance bridge	yes	readout temperature sensors
PICOWATT TS-530A temperature controller	yes	temperature regulation in mixing chamber
PICOWATT PLM-5 NMR thermometer	yes	controls for the magnet
PICOWATT AVS-47IB computer interfaces (2 times)	no	data handling
Stanford Research Instruments mainframe	yes	socket for the SIMs
Small Instrumentation Module 928 (SIM, 2 times)	yes	isolated voltage source for heaters
Keithley 2000 multimeter (3 times)	yes/no	signal readout
National Instruments GPIB BUS hub/controller	no	data handling
Twickenham Scientific Instruments (2 times)	no	helium depth indicators
Pfeiffer Vacuum dual gauge (3 times)	no	readout pressure sensors for IVC, still and 1K-pot
HAMEG HM8142 (2 times)	no	programmable power supply
TRACO Power	no	power supply, battery pack, battery controller

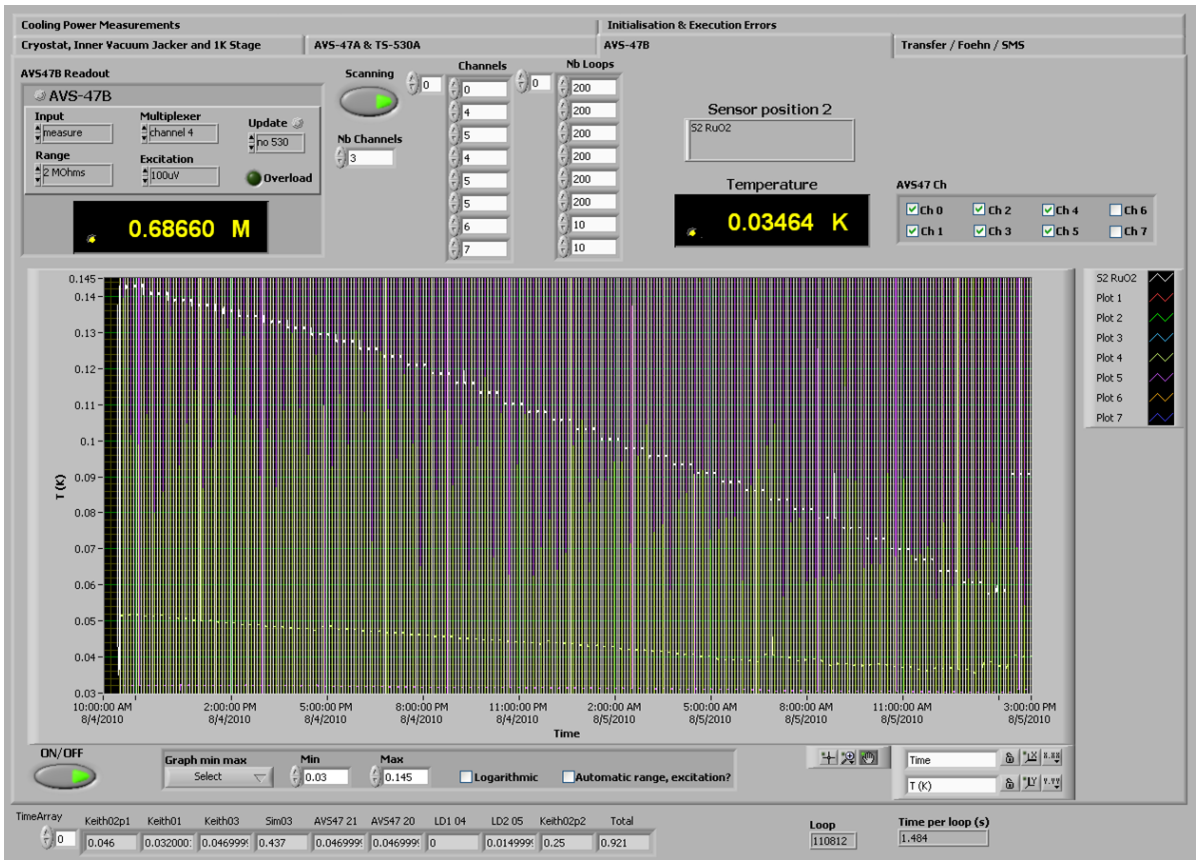

Figure 4.6: GUI of the LabVIEW® program.

4.3 Dilution Refrigeration

Out of the variety of cryogenic cooling methods, dilution refrigeration is the only one supplying continuous cooling power below ≈ 300 mK. Since AEgIS need continuous cooling power at around 100 mK, it will make use of a dilution refrigerator. The method used in dilution refrigeration has been proposed first by Heinz London in the early 1950s[3] and the first operating device was built in 1962[44]. Nowadays it is the standard method of reaching temperatures below 300 mK with a record of less than 2 mK. Reaching such low temperatures involves various ultra low temperature and vacuum techniques.

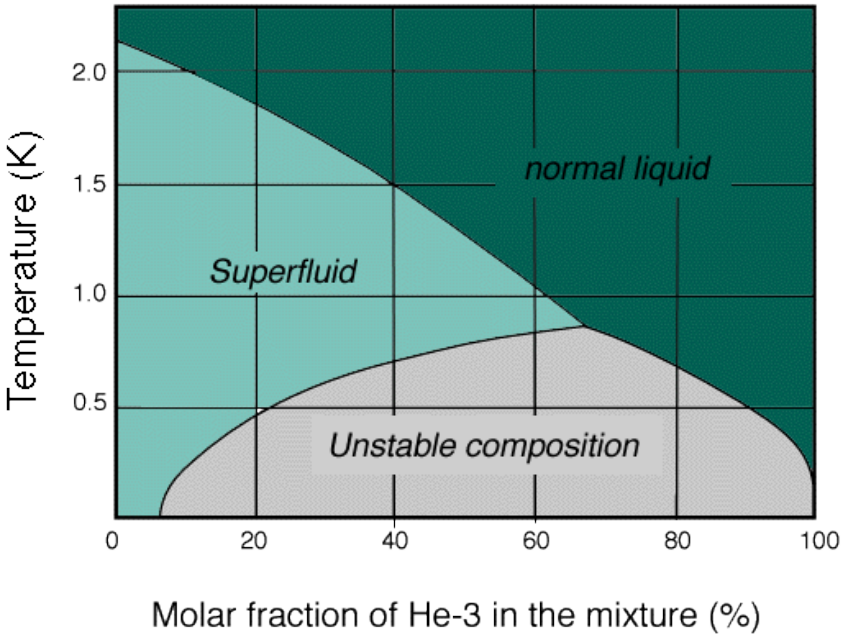

Figure 4.7: Phase diagram of the ^{3}He-^{4}He mixture [45]. Below ≈ 870 mK, a phase separation into two phases is observed.

4.3.1 Physical background

Dilution refrigeration uses a physical effect emerging at low temperatures in mixtures of ^{3}He and ^{4}He. Below about 870 mK, the mixture separates into two phases, a ^{3}He-rich phase and a ^{4}He-rich phase, see Figure 4.7. When further cooled, the ^{3}He-rich phase increases its relative amount of ^{3}He until at 0 K the liquid becomes pure ^{3}He. On the contrary, the ^{4}He-rich phase still contains a certain amount of ^{3}He when approaching 0 K. At absolute zero, this fraction is about 6.6 %[3]. This phase is also called the "dilute"

phase.
Having the two phases in the given volume of the mixing chamber, the lighter ^{3}He-rich phase flows on the ^{4}He-rich phase, both being liquids. When pumping only on the ^{4}He-rich side, mainly ^{3}He evaporates and is pumped away, since at low temperatures it has a significantly larger vapor pressure than ^{4}He. To maintain the composition of the dilute phase, ^{3}He-atoms will migrate from the ^{3}He-rich phase, crossing the phase boundary. To do so, the atoms need energy, which is taken from the thermal energy of the environment. In other words, when forcing ^{3}He to cross the phase boundary, the heat of mixing is taken away from the helium mixture. This cooling power can be maintained continuously when ^{3}He is circulating, i.e. when the ^{3}He taken away from the dilute phase is supplied for the ^{3}He-rich phase. A schematic overview of this process is shown in Figure 4.8.

4.3.2 Implementation of the cooling method

The ^{3}He-circuit is realized by taking the pumped out ^{3}He and reintroducing it to the ^{3}He-rich phase in the mixing chamber. Since the helium goes through a system of pumps and is therefore heated to room temperature, it has to be pre-cooled on the way back to the mixing chamber. This is done by staged cooling, diagramed in Figure 4.8. It is realized inside the so-called "inner vacuum chamber" (IVC), visible in Figure 4.9. The vacuum is necessary to avoid thermal contact of warm and cold parts by convection of gas. The IVC is emerged in a liquid helium bath and has therefore a temperature of about 4.2 K. Anything leading inside the IVC like cables or helium (through tubes) is thermalized to the same temperature on the way through the bath. Inside the IVC the cooling of incoming ^{3}He continues. First, evaporative cooling of ^{4}He creates temperatures of about 1.5 K. This is done in the so-called "1 K-pot". The incoming ^{3}He is cooled to this temperature, where it condenses. Further down it will pass the "still", where 0.7 K are initially reached by evaporative cooling of the outgoing ^{3}He. As mentioned above, ^{3}He has a much larger evaporation pressure than ^{4}He, so a lower temperature can be reached by the same method of evaporative cooling. The further cooling is done by heat exchangers, where heat from the incoming ^{3}He is transferred to the outgoing, cold ^{3}He which comes from the mixing chamber. With this technique the ^{3}He is further cooled down to the temperature of the mixing chamber. There the cooling power of the helium mixing is available, which cools the whole mixture in the mixing chamber. Heat exchangers play a major role in the cooling process. The cold ^{3}He leaving the mixing chamber is constantly warming up on the way out of the cryostat, supplying additional

and necessary cooling power for the incoming ^{3}He via heat exchangers. Also the cooling of the still during operation of the DR is effected by the cold ^{3}He.

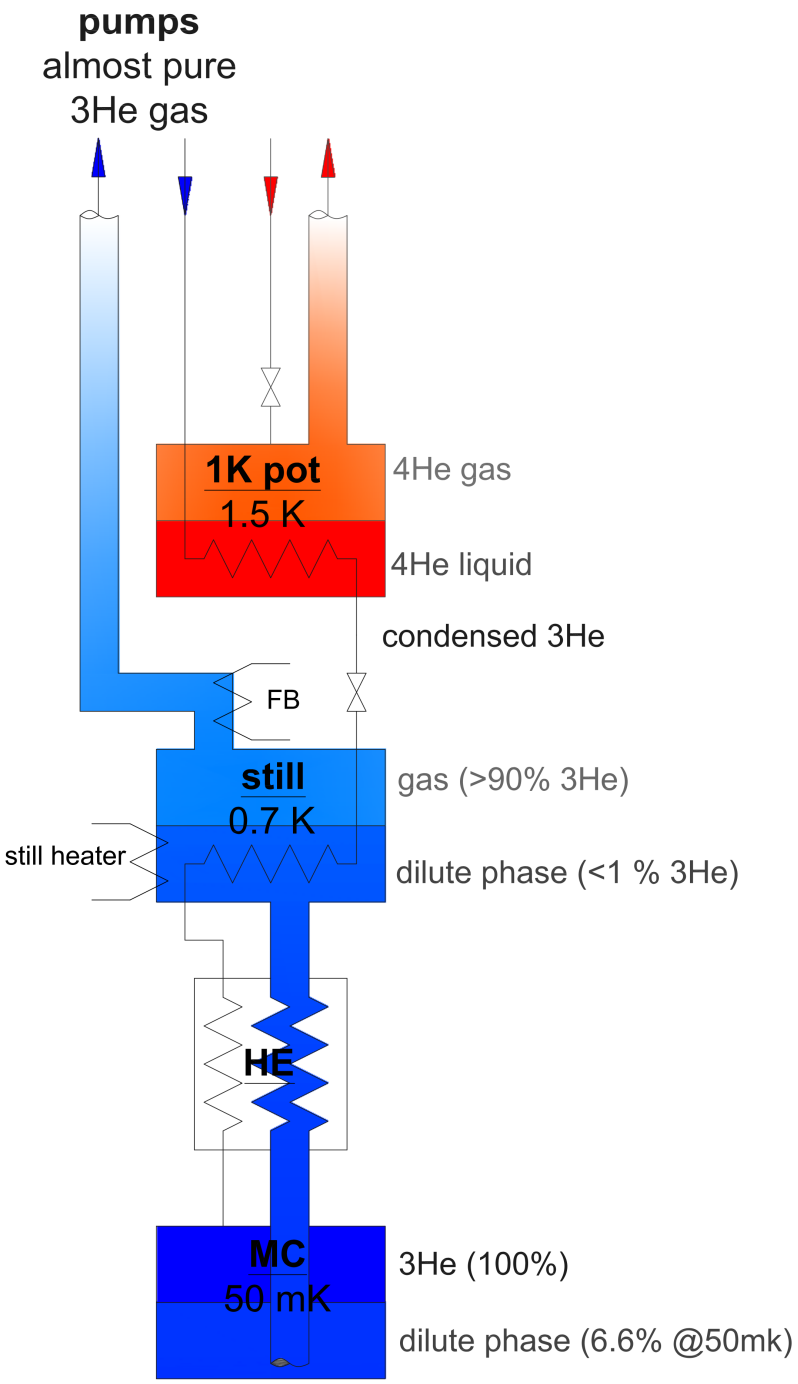

Figure 4.8: Scheme of the staged cooling in a dilution refrigerator. Detailed explanation of the working principle is given in the text.

4.3.3 The CERN Cryolab Dilution Refrigerator (CCDR)

The design of the CCDR is shown in 4.9. On the right side the IVC with the central components of a dilution refrigerator (1 K-pot, still, mixing chamber, heat exchangers) is shown. On the left the CCDR mounted in the cryostat is shown. The pump lines (for ^{4}He and ^{3}He, respectively) can be seen as tubes. They also act as carrier for the IVC. On the very top the main flange houses all the feedthroughs for the pump lines, cables and other parts reaching into the cryostat. In the cryostat a bath of liquid helium is supplied, in which the IVC is placed.
Figure 4.10 shows the dilution refrigerator outside the cryostat. The IVC is unmounted and therefore the 1 K-pot, the still and mixing chamber are visible. The heat exchangers are inside the spiraling tubes reaching from the top flange all the way down to the mixing chamber. The radiation baffles at the top are necessary to shield thermal radiation from the top flange, which is at room temperature also during operation.
Figure 4.11 shows the dilution refrigerator in operation.

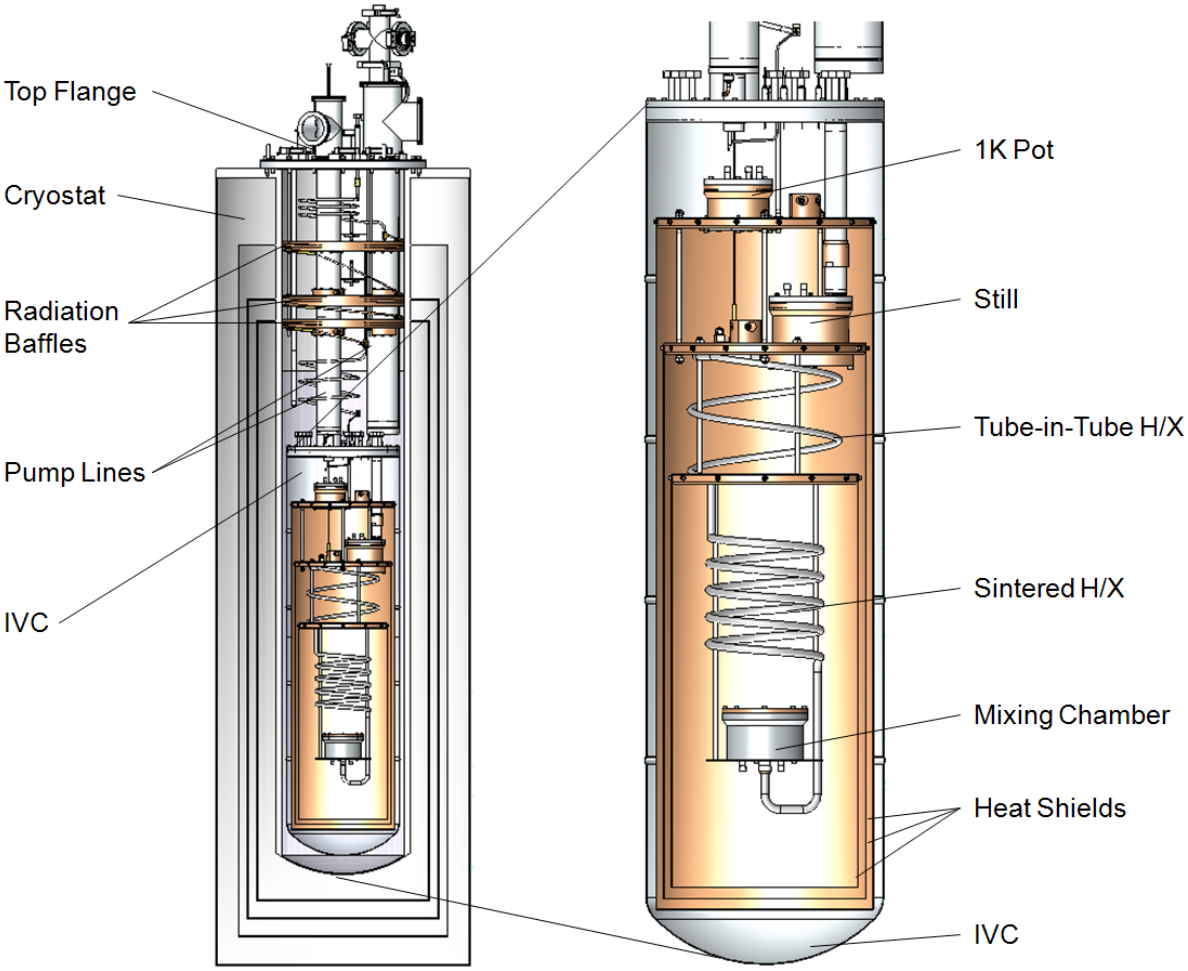

Figure 4.9: Design of CERN's Cryolab Dilution Refrigerator (CCDR). H/X stands for heat exchanger. The other parts are explained in the text.

4.3.4 Operating the CCDR

The operation of the CCDR requires time-consuming preparations. After having completed work on the test setup on the mixing chamber, e.g. installing a new sandwich, many procedures have to be done before any measurements at ultra low temperatures can be conducted. They include:

- On the unmounted dilution refrigerator:
  - Soldering electrical connections (e.g. from the sensors on the stamp, which have to be dismounted when installing a sandwich).
  - Testing all electric connections.
  - Mounting of the heat shields within the IVC.

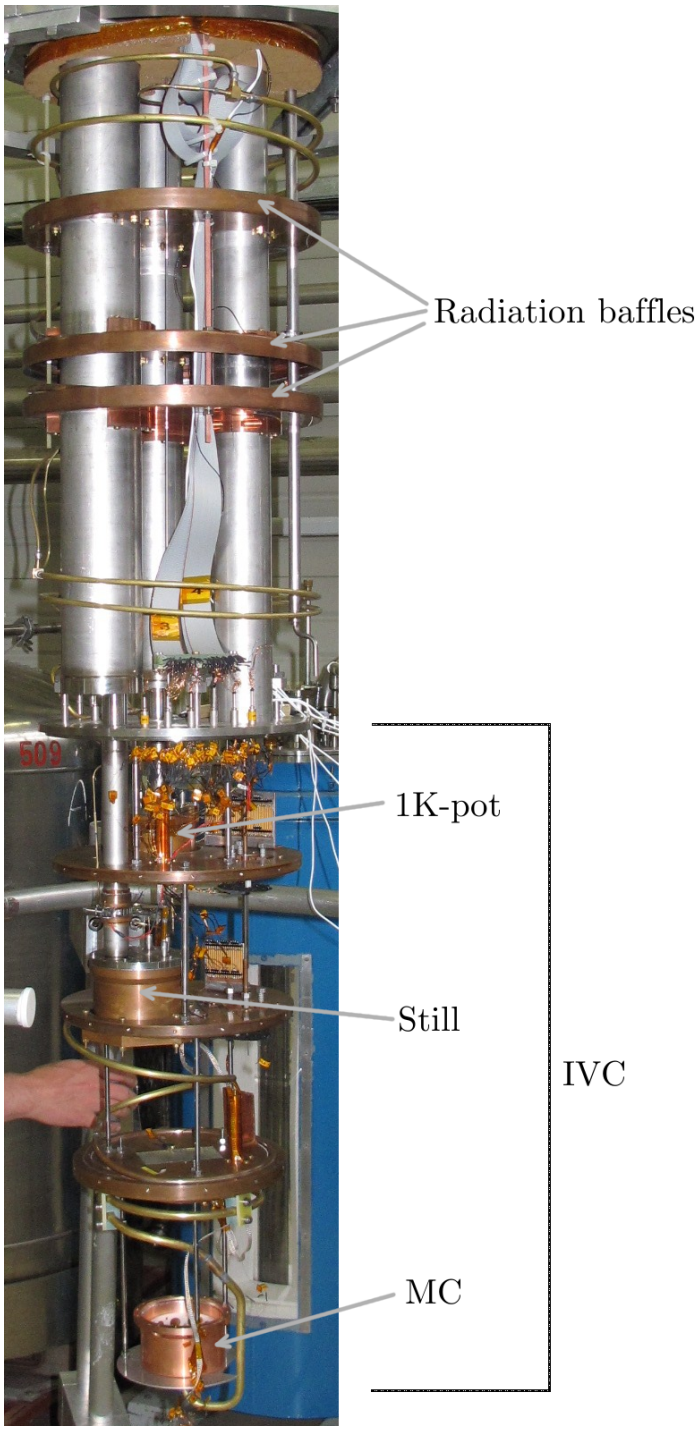

Figure 4.10: The CCDR outside the cryostat. The IVC is unmounted and therefore the 1 K-pot, the still and the mixing chamber are visible. The heat exchangers are inside the brass tubes spiraling down to the mixing chamber.

Figure 4.11: The CCDR in operation. The cryostat is placed in the floor, so only the upper part is visible (on the right side of the image). From the dilution refrigerator only the top flange is visible, with all necessary connections (tubes, cables). The tubes of the pump lines are visible, leaving the dilution refrigerator on top and then bending to the right. On the left the electronic module racks are visible as well as the workstation for data acquisition and controlling. The helium dewar for the liquid helium supply for the bath is posed next to the electronic racks, also placed in the ground.

  - Preparing the delicate IVC indium gasket and closing the IVC.
  - Leak tests of the ^{3}He-circuit and the IVC.

- After the dilution refrigerator is put in the (still warm) cryostat:
  - Activation of the charcoal trap (heating, pumping).
  - Connection of all cables and helium lines.
  - Filling of the cryostat with liquid helium, connecting the dewar and the recuperation line.
  - Leak test of the ^{3}He-circuit.
  - Use of exchange gas (hydrogen) in the IVC to cool down the parts in the IVC.
  - Evacuation of the IVC.
  - Pumping on the 1K-pot.
  - Introduction of ^{3}He into the ^{3}He-circuit and starting the circular flow.
  - Waiting for residual heatloads to diminish.

These procedures take at least two weeks and have to be done every time when the dilution refrigerator has been dismounted and at ambient temperature.

The stable operation of the dilution refrigerator after it has been cooled down is mainly achieved by the electronics and the control program. Still, everthing has to be monitored by the user regularly and tasks like changing the helium dewar have to be done manually.

The warm-up is a little less complicated than the cool-down, but still requires several days of work. Especially the recuperation of ^{3}He to the reservoir has to be done very carefully, see next section.

4.4 Experimental challenges at ultra low temperatures

4.4.1 Reducing heatloads acting on a ultra cold system

Working at ultra low temperatures involves special techniques to diminish heat input from outside a cold system. A body having a temperature in the millikelvin range carries only a relatively small amount of thermal energy. Therefore very small energy inputs

(heatloads) acting on the body can increase its temperature significantly. To diminish the heatloads on a cold system, the system has to be protected from heatloads by:

- Avoiding convective heat transfer by using a vacuum environment.
- Diminishing conductive heat transfer by using mountings out of materials, which conduct heat poorly and by using appropriate mounting designs.
- Shielding thermal radiation.

The last point is realized by two means. First, multilayer insulations out of several tens of thin high-reflectivity material reflect thermal radiation very effectively. Second, heatshields lower the radiation acting on an ultra cold part. They make use of the Stefan-Boltzmann law, which states that the radiative heat flow from a surface at temperature T is proportional to ϵT^4, where ϵ is the surface material's emissivity. Any surface "seen" by the ultra cold part should be at a very low temperature as well to keep the radiative heat flow little. Therefore the ultra cold part is normall completely surrounded by a shield being at a temperature close to the ultra-cold part. This and potential additional shields have to be actively cooled, of course. Staged heatshields of the CCDR can be seen in Figure 4.9. There the innermost shield is kept at about 200 mK by the cold helium coming out of the mixing chamber. Additional shields are connected to the still (≈ 700 mK) and the 1K-pot as well as to the radiation baffles on the outer cryostat. Heat shields also act as cold surfaces, where residual gas molecules can condense. Therefore they support the vacuum environment.

4.4.2 Vacuum at low temperatures

The IVC of the CCDR is at a pressure of about 10^{-5} mbar and at a temperature of about 4.2 K. Normal rubber gaskets can't be used for vacuum seals, since they get brittle and rigid at this temperature. Instead, indium gaskets are used, since the metal stays ductile down to very low temperatures. The preparation of the gasket for the IVC is a delicate task, since the used indium wire has to be placed accurately at the seal, which has a diameter of about 40 cm. Any pollution has to be avoided, since it could make the gasket defective by introducing leaks to the system. Before mounting the dilution refrigerator in the cryostat, excessive leak tests are performed to ensure the leak tightness of the system.

When measuring temperatures, the thermal contact between the sensors and any relevant parts has to be very good. Normally thermal grease is placed on any contacts. In a

vacuum environment the use of grease is unfavorable, since the grease might outgas. For the contact between two metal parts, thin indium sheets are used instead, since indium is a good heat conductor and ensures good thermal contact due to its ductility.

4.4.3 Superconductivity

At very low temperature several materials show superconductivity, including indium. In the superconducting state, the material's conduction electrons are grouped in so-called "Cooper pairs" and are therefore no longer available for thermal conduction. Since indium is used for thermal contacts at very low temperatures, its superconductivity has to be disabled. This can be done by a sufficiently strong magnetic field. In the test setup on the CCDR, this magnet field is realized by a superconducting magnet surrounding the mixing chamber. In the AEgIS setup the superconductivity of indium will be disabled by the high magnetic field, which is necessary for the beam environment.

4.4.4 Dilution refrigeration: Helium-3

The principle of dilution refrigeration is based on the use of the helium isotope ^{3}He. ^{3}He is very rare and therefore very expensive, if available at all. Therefore any loss of ^{3}He has to be avoided. This makes it necessary that the ^{3}He-circuit of the dilution refrigerator is absolutely leaktight. Whenever the dilution refrigerator is opened, ^{3}He is transferred to a storage reservoir. After having worked on the test setup, extensive leaktests are performed on the ^{3}He-circuit, which takes several days. They are a major task when preparing the dilution refrigerator for cooldown.

5 Measurements and results

The measurements, their preparation as well as the data analysis are presented in this chapter. The results are discussed and the implications on AEgIS are evaluated.

5.1 Preparation of measurements

After all steps for the cooldown are completed and the mixing chamber shows already the stable preset temperature, other temperature sensors might still show a significantly higher temperature, up to several millikelvin off the preset temperature. This is due to residual heatloads. The higher temperature persists over days or even weeks and is only slowly decreasing. After letting the residuals cool down for about one week, the remaining discrepancies in temperature are counteracted by taking the differences as an offset with T_{LS} as the reference. This can only be done when taking the decreasing temperatures constant over the time of one measurement. Due to the very long relaxation times of the residuals this condition can be seen as fulfilled.
Furthermore, each sensor shows its own stability, depending not only on systematic factors like its excitation, but also on the very given settings of the measurement. Many factors play a role in this issue, e.g. a noisy contact of a wire or RF capture of a certain frequency range can already cause significant disturbances. Therefore, after each cooldown each sensor's stability has to be checked by watching the temperature curve over some time.
Also the contact of the sensors to the setup is checked regularly. The sensors are glued to little pieces of copper, which are then screwed to the places where needed as seen in Figure 4.5. To ensure good thermal contact, indium foil is put between the copper pieces and the place where it is screwed. Some sensors have to be dismounted whenever the sandwich is changed, so the contact does not stay the same all the time. To test the contacts, the influence of each sensor's excitation to its temperature signal is checked. This is done by monitoring the sensor's temperature at different excitation levels, i.e. at different (tiny) heat inputs acting directly in the sensor. If the contact is bad, the

temperature rises abnormally. This procedure gives also information about the noise level which can be expected during the measurements. A higher excitation means lower noise, since the signal from the sensor is larger. However, some self heating is always observed at high excitation levels, so a compromise concerning the excitation used for the measurements has to be found.

Measured variables

For each measurement the temperatures at the top of the sandwich (T_1), at the bottom (T_2) and in the mixing chamber (T_{SC3} and T_{LS}) are measured. Also the heating power on the stamp, $\dot{Q}$, is measured.
In addition to this, temperatures on various other places in the dilution refrigerator can be measured (e.g. IVC), but these are normally only used for monitoring the cooldown and warm-up. With the temperatures from the list above, the sought-after quantities from the static and dynamic measurements can be calculated.

Further procedures

During the measurements it is important to monitor the temperature of the ^{3}He-^{4}He mixture, since its stability is requisite for stable conditions. Also the ^{3}He-flow through the mixing chamber has to be kept stable. Especially the transfer of liquid ^{4}He is always accompanied by disturbance of temperatures and only after about 1 hour conditions are again back to normal, see Figure 5.1. This is not avoidable, since each transfer starts with the warm helium flush gas, which rests in the transfer line. Therefore the transfer always introduces warm gaseous helium into the cryostat. As this helium finds its way through the cryostat to the recuperation line, it influences the in- and outlets of the ^{3}He-circuit, which pass through the gaseous helium above the bath. Therefore the ^{3}He-circuit is minimally disturbed, but strong enough to influence the ^{3}He-flow and the temperature of the mixing chamber.

All measurements are done at three different base temperatures, i.e. preset temperatures of T_{LS}. They are 30, 50 and 70 mK.

For each sandwich, the preparation of the sample, the mounting and cooldown has to be performed only once. After the sandwich has been put in place and cooled down,

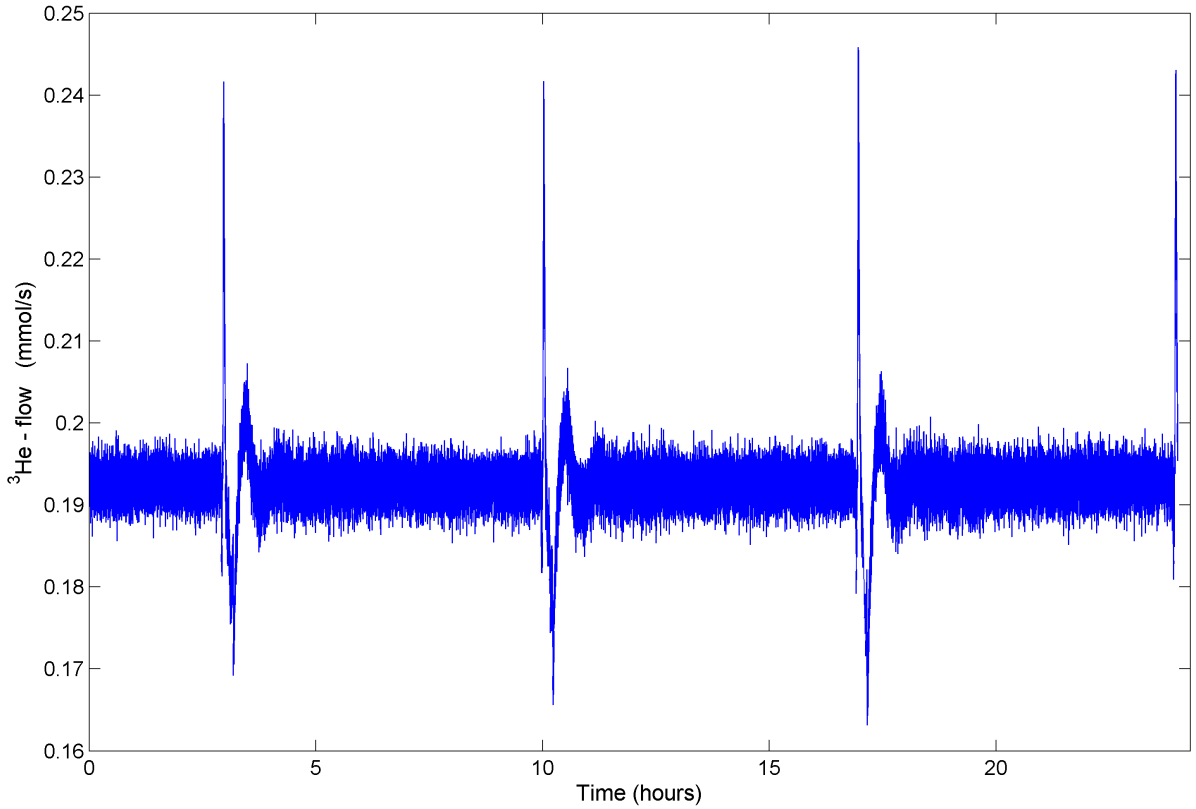

Figure 5.1: ^{3}He-flow disturbances caused by the transfer of liquid ^{4}He into the cryostat. These variations are accompanied by a small variation of T_{LS}. Therefore, measurements were preferably done between two transfers.

the dynamic, step and static measurements are done on the setup one after the other.

5.2 Dynamic measurements

The dynamic measurements are conducted for various reasons:

- They reveal information about the time-dependend behavior of the implemented sandwich solution
- They can be used to verify values obtained from the static measurement.

The first item is the major part of the presented work and is treated in this section.

As explained in section 3.5.2, in a material a given variation in temperature over time at one place will propagate through the material and causes some altered variation of temperature at any other place in the material with some delay. The material property, which determines this propagation, is the thermal diffusivity α. The larger the value for α, the faster the variation will travel from one point to another. In section 3.5.2 it is explained that a temperature oscillation has to be created at the top of the sandwich to measure α^* of the sandwich.

5.2.1 Periodic temperature variation

The test setup is not able to create a sinusoidal temperature variation on the top side of the sandwich. In fact, the heater used for changing the temperature can only be switched on or off and its heating power can be set to a certain value. The heating power is supplied by the very accurate power supply SIM 928 from Stanford Instruments. Controls in the LabVIEW® program offer automatic switching of the heater, where the following parameters can be set:

- Heater voltage,
- duration of heat pulse and
- duration of pause between heat pulses.

The resulting voltage variation has the shape of a square wave. Because of the thermal mass connected to the heater, the resulting temperature variation at the top of the

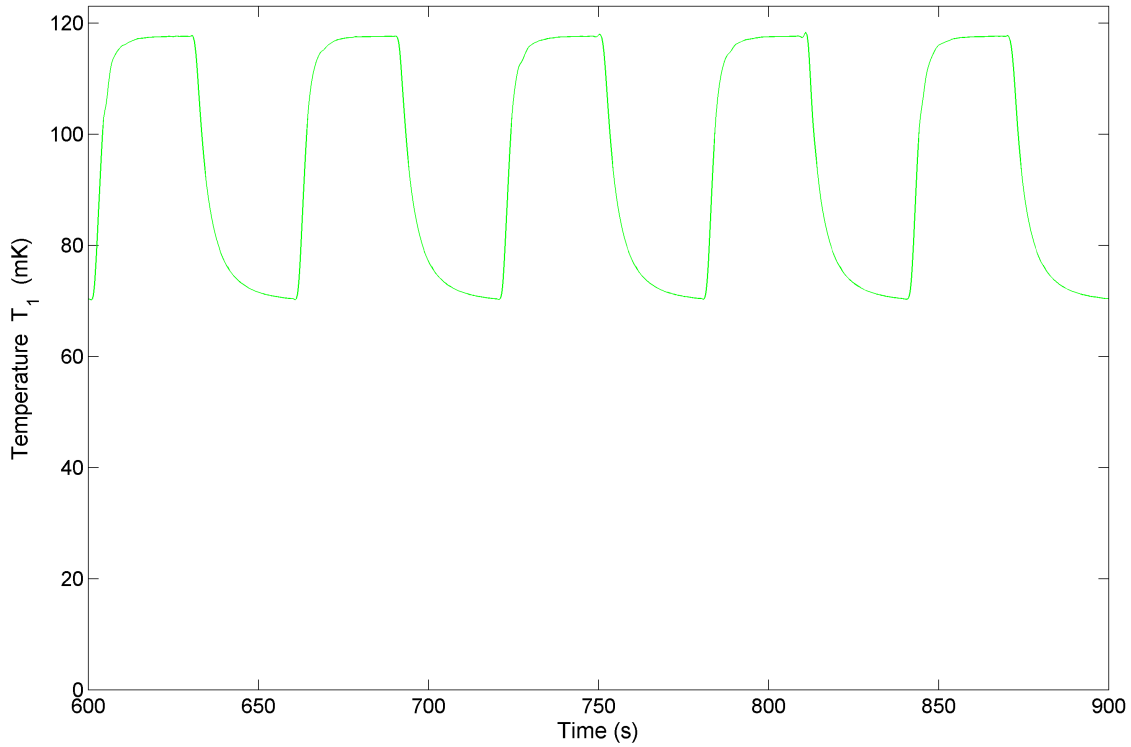

Figure 5.2: Typical temperature variation of T_1 resulting from the periodic heating. The original square wave is altered due to the thermal mass connected to the heater (Cu-stamp, sandwich, etc.).

sandwich has in general a shape like shown in Figure 5.2. Of course, the shape looks different for each sandwich, period and mixing chamber temperature.

For each given temperature of the mixing chamber (30, 50 and 70 mK), the measurements are done with three different oscillation periods, namely 30, 40 and 60 s. The first half of the period is the time when the heater is switched on, and the second half is without heating.

5.2.2 Particular considerations

Quasi-static state

One problem regarding the measurements is the readout of the RuO_2 temperature sensors. The resistance is measured with the resistance bridge PICOWATT AVS-47B. This bridge can only measure one sensor at a time, so temperatures of different sensors can not be measured simultaneously. Fortunately, when having the periodic heating applied, a quasi-static state is soon achieved, meaning that the (more or less fast) oscillations are still well there, but the average temperatures reach stable values, see Figure 5.3. Since this stability is maintained for the duration of each measurement, consecutive readouts of the channels can be treated as if they were done simultaneously. As zero-point for each readout any switching-on of the heater voltage can be taken, since the periodic heating is not changed during one measurement. Only this procedure enables to measure the phase shift of a heat pulse.

Thermalization speed

The top side of the sandwich is connected to the copper stamp, which can be seen in Figure 4.2. The heater and the temperature sensor are attached to it and between them there is a certain distance. Also the top part of the sandwich (the very upper indium-copper contact) is not exactly where the heating or sensing is performed. Therefore the question arises if the measured temperature is really the temperature at the top of the sandwich.

Below 1 K the thermal conductivity λ of sapphire is orders of magnitude lower than the one of copper. Since the thermal diffusivity α is directly proportional to λ (equation 3.18), it can be assumed that α is significantly higher for copper and that the major barrier for the heat transfer is the sandwich. As we will see later, this assumption is verified by the measurements. Therefore, the thermalization of the copper stamp can be taken as fast enough so that measured temperature is (within the measurement error)

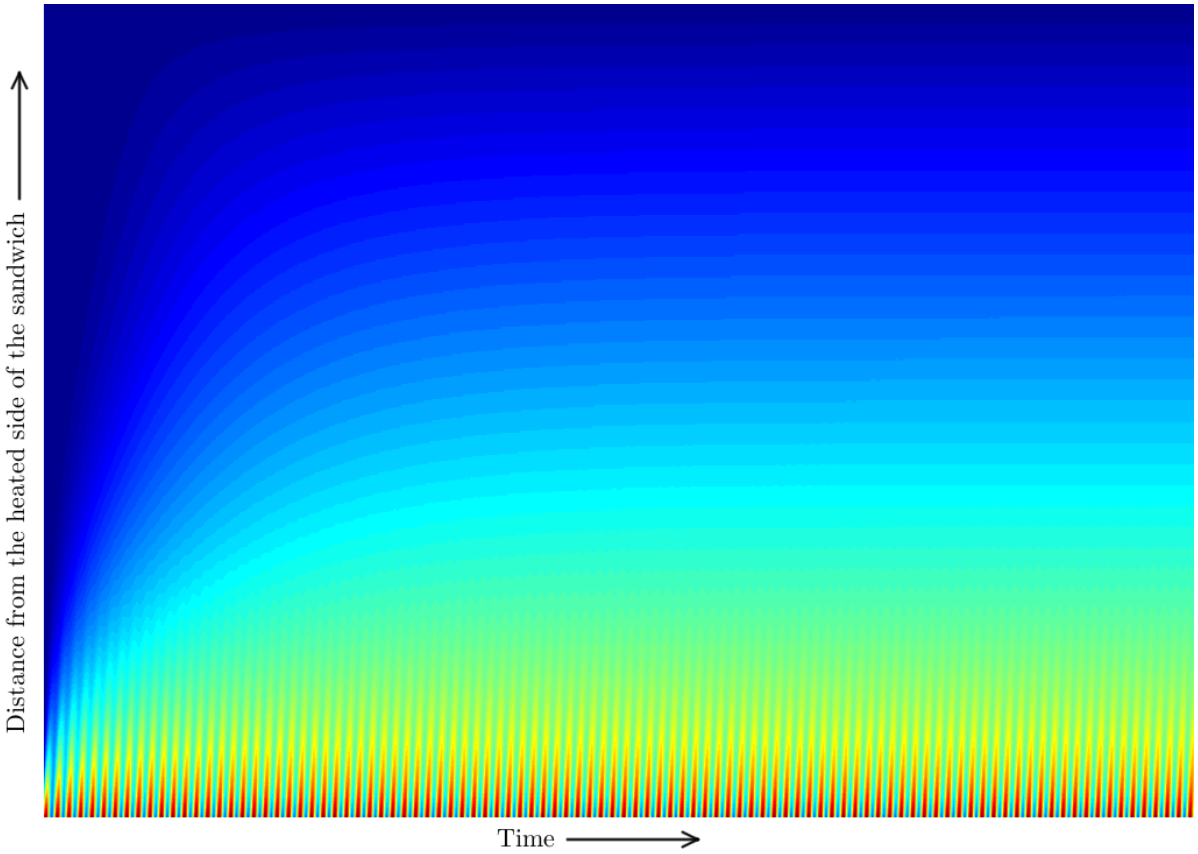

Figure 5.3: Graphic presentation of the results of the simulation, showing the achievement of the quasi-static state. The color represents the temperature (blue: cold, red: warm). The simulation time runs from the left to the right and the position in the (simulated, one-dimensional) sandwich is plotted on the ordinate. At the beginning of the simulation, the sandwich has the uniform temperature T_{LS}. The periodic heating on one side (here at the bottom of the graph) creates a certain temperature distribution in the sandwich. This distribution oscillates with the same period as the heating, but reaches a quasi-static state after some time, i.e. the average over one period or multiples of it yields a static temperature distribution.
The temperature oscillation is also present in the upper part of the graph, but too small to be seen there. The phase shift of the oscillation at a given point in the sandwich is visible as a slight tilt of the red "peaks" to the right. Units are not given, since the scale depends on the simulation. However, the pattern shown here emerges in every simulation conducted.

really the temperature on the top plane of the sandwich.

Time resolution

On the GUI of the LabVIEW® program, many values from different pressure, temperature and other sensors can be read. The readout and processing of all signals takes about 1.5 s. For the dynamic measurement the time resolution is important, so this time is shortened by switching off channels, which are not used for the measurement (e.g. pressure monitoring). In doing so, a readout is done every 0.7 s, which means about double the datapoints for a measurement.

5.2.3 The dynamic measurements

For the dynamic measurements the sensors listed in table 4.1 are used. The temperature of the heat exchanger in the mixing chamber, T_{SC3} is also measured but only used for monitoring.

An example of a measurement is shown in Figures 5.4 to 5.6. It is clearly visible, that the amplitude of the temperature oscillation experiences a significant attenuation travelling through the sandwich. The heater voltage is chosen in a way, that enough power is placed on the top of the sandwich to still get an evaluable amplitude at the bottom side. The resulting amplitude of T_1 at the top ranges from about 9 to 25 mK. The heat pulsing is applied automatically by the program. After it is switched on, the quasi-static state is waited for and 5 periods are recorded. As soon as enough data are collected for one temperature sensor the channel of the resistance bridge is changed and the next temperature sensor is read out. The starting time of the 5 periods is logged with an accuracy of $\pm 15\,\mu$s, since it is used to determine the phase shift of the temperature variation. This procedure is repeated for each different oscillation period, mixing chamber temperature and sandwich, resulting in 36 measurements. Their results are listed in table 5.1.

5.2.4 Analysis - dynamic measurements

The analysis of the data is not straightforward nor quickly done, but involves manual preparation and also time-consuming simulations.

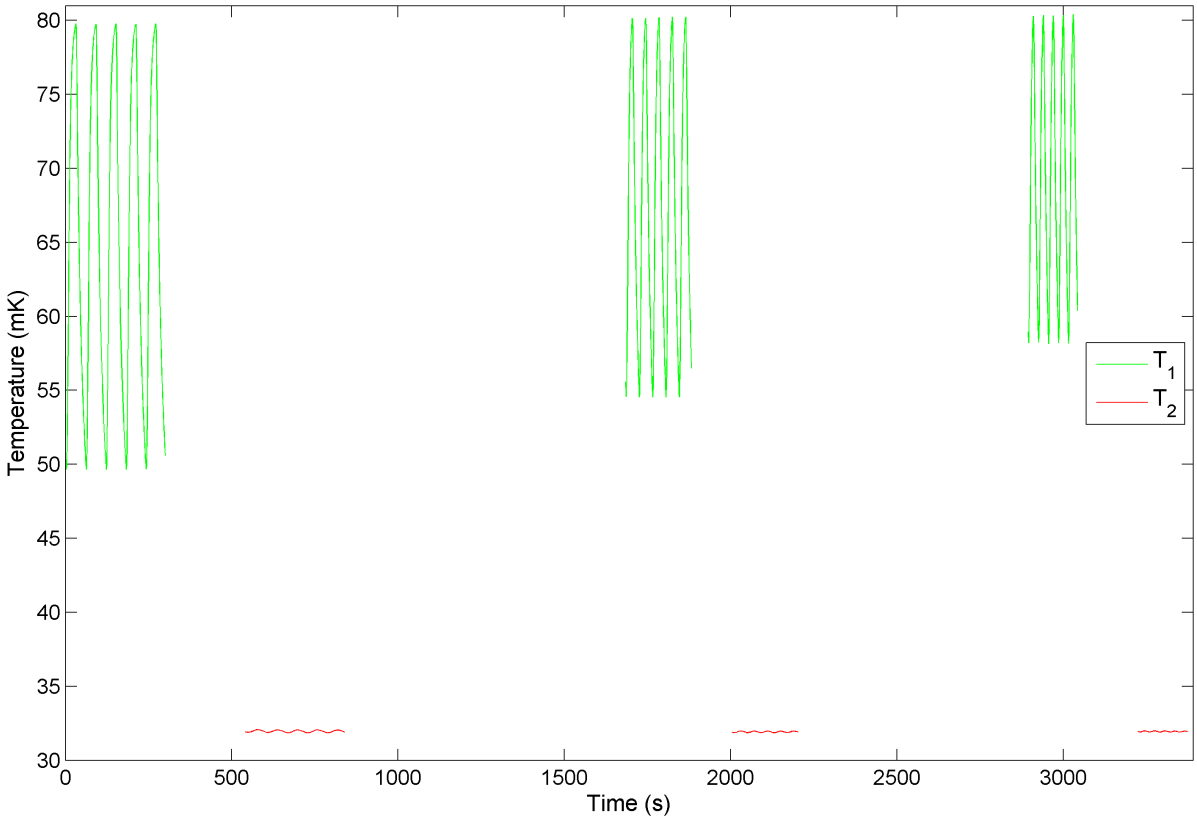

Figure 5.4: Overview of one dynamic measurement (sandwich C, T_{LS}=50 mK, heating period=60 s). The temperature variation resulting from the heating power variation is clearly visible for both temperatures T_1 and T_2.

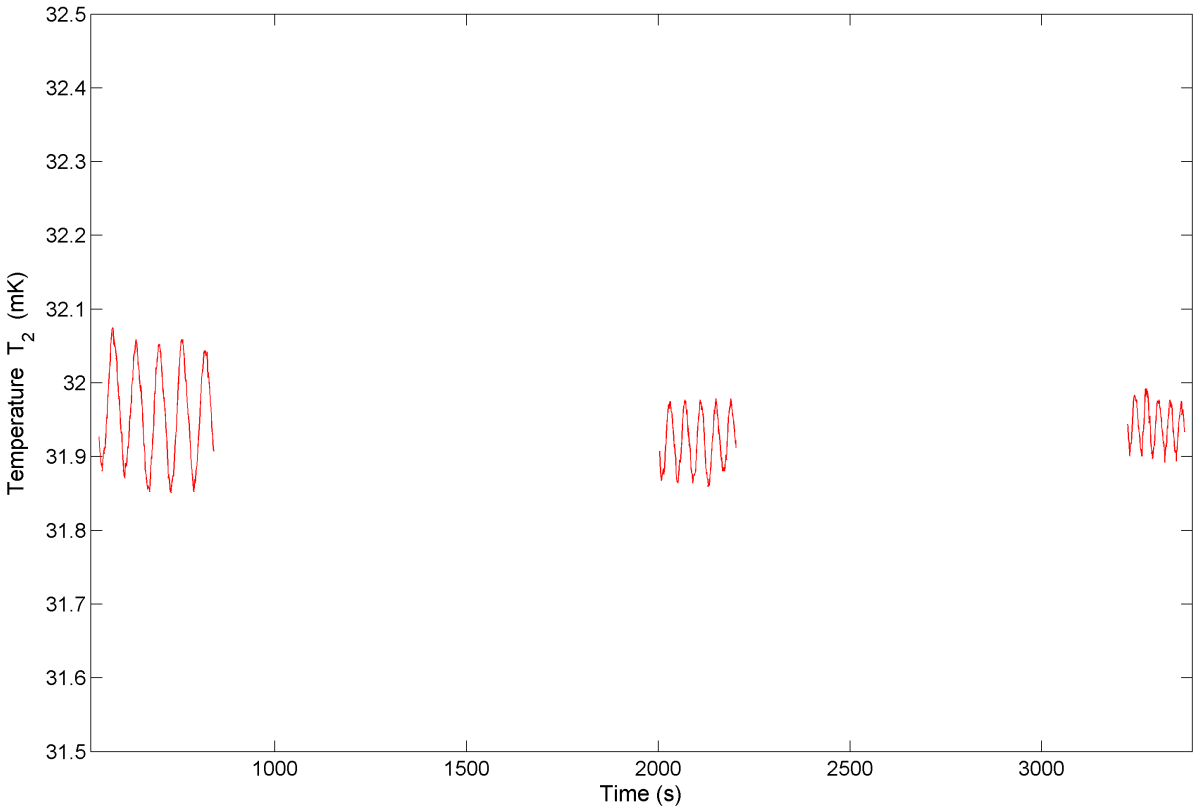

Figure 5.5: Detail of the measurement from Figure 5.4 to show the variation of T_2 in greater detail.

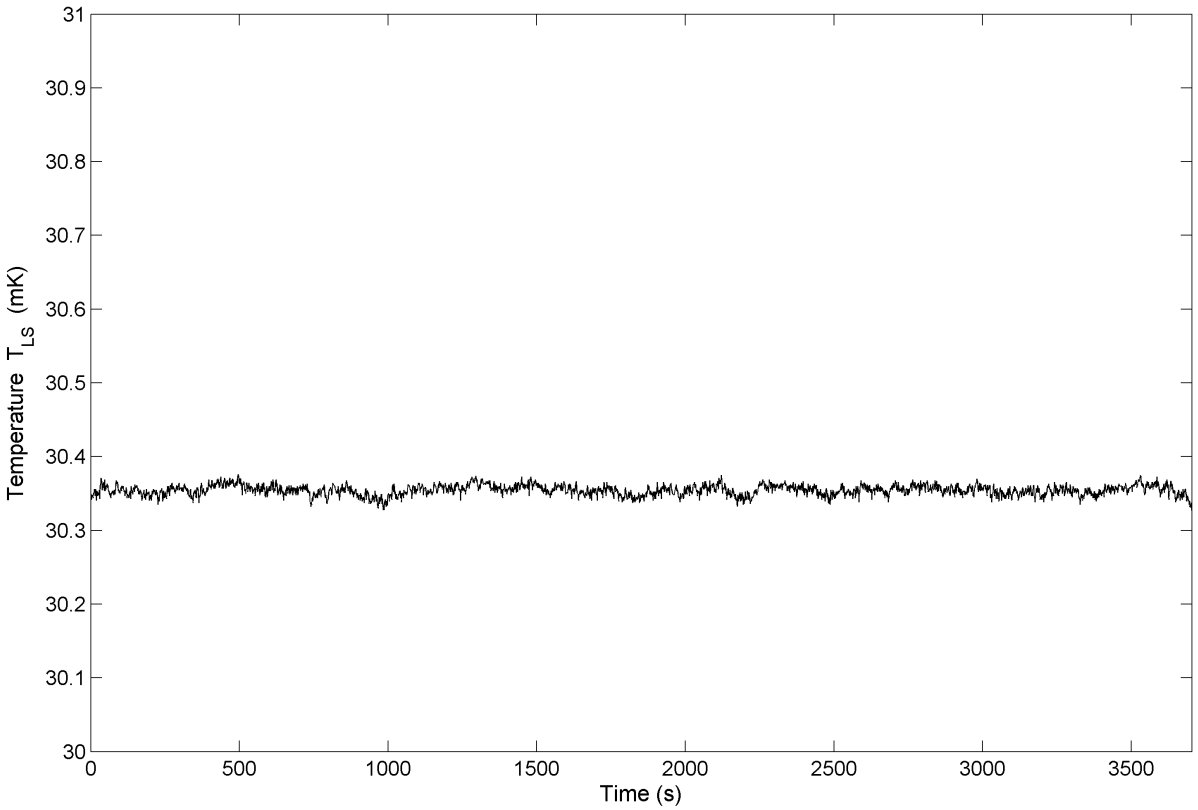

Figure 5.6: T_{LS} during the measurement shown in Figure 5.4. The observed variation of T_{LS} of about 25 μK at an absolute value of more than 30 mK is not only proof of a very stable temperature in the mixing chamber, but also shows that the signal-to-noise ratio is very good.

Preparation of Data

The analysis of the data is made up of the following parts:

1. Getting relevant data out of the raw data files
2. Group and sort data
3. Visualization
4. Calculation of the relevant parameters
5. Analysis of parameters to get α^*

First the data series of the relevant five oscillations for each temperature sensor and each measurement have to be extracted from a large file, which contains all data from one day (24 hours). This has to be done manually, since series of data has to be shifted correctly in time to achieve simultaneity. Only then visualization is done to check the data by eye. Before that, only the real-time visualization of the measurement and notes about it in the laboratory logbook identify the quality of the data. After this, calculation of the relevant parameters is done, which then are further analyzed.

Relevant parameters

According to theory (section. 3.5.2), the phase φ and amplitude A of the temperature oscillation are the parameters, from which the sought-after thermal diffusivity α^* can be deduced. These are the values, which are calculated from the prepared data. The complete list of them can be found in table 5.1.
As mentioned above, the simple ideal case of a semi-infinite rod is not realized with our setup, so the calculation of α^* by the parameters φ and A via the simple formulas (3.16) and (3.17) can not be done. Instead, computer simulations of the basic physical process "heat transfer" of the sandwiches have to be done. The comparison of their results with the actual measurements and optimization yields α^*.

5.2.5 Simulation

The basic idea of the simulation is the following: the measured temperature variation on the top of the sandwich is taken as a given. Heat transfer through the sandwich is simulated and the resulting simulated temperature variation on the bottom of the sandwich is compared to the real variation, which is also given. The simulation is

repeated with different values for its parameters until an optimum agreement with the real measurements is achieved. The simulation run with the optimized parameters yields α^* for the sandwich. The optimization remains manageable, since the only parameter to adjust in the heat equation is the thermal diffusivity α^*, see equation (3.15). However, other degrees of freedom of the simulation have to be taken care of and are discussed below.
The simulation is done in MATLAB®.

Modeling of the sandwich

As in any simulation, reality has to be modeled to become numerically computable. Simplifications are made in this step, but they are all justified as explained in this section. A schematic overview of the modeling is given in Figure 5.7.

Dimensionality & utilizing symmetry

A three-dimensional simulation would take too much time to implement, so the decision has been made to make a one-dimensional model. The real sandwich can be thought of a cylinder of sapphire with layers of indium on its faces. Since this geometry shows radial symmetry, the problem can be reduced to a one-dimensional "rod". To be able to do so, the temperature of any plane perpendicular to the cylinder's axis has to have homogeneous temperature. This is the case if the following requirements are met:

1. No sources or sinks of heat within the sandwich.
2. No gain or loss of heat on the lateral sides.
3. The top and bottom planes (faces) of the cylinder always have homogeneous temperature.

The first assumption is straightforward and is certainly met. The second one can also be treated as fulfilled, since the sandwich is operated in vacuum and is shielded by several layers of multilayer insulation and thermal shields. Therefore heat transfer via conduction or radiation through the lateral sides can be neglected.
The third assumption is equivalent to the demand that the copper pieces connected to the sandwich are quickly thermalized. This issue has already been treated before in section 5.2.2, where the thermalization has been concluded to be very fast and therefore also this assumption is justified.

Homogeneity

The simulation of the sandwich as a package of indium-sapphire-indium would complicate the simulation drastically, that's why the model of the sandwich has been simplified to have homogeneous structure. This means it is treated as being a one-dimensional rod out of *one* single material, having the only intrinsical physical property "thermal diffusivity". The effects of this have already been mentioned in section 3.5.2. The main consequence is that the calculated value for α^* can not be used with any similar material, but only for a stacked material of a 1.5 mm thick central layer of sapphire covered by a layer of indium on each side with the respective thicknesses.

Thickness

The thickness of the sapphire disks is (1.5 ± 0.01) mm and their diameter is (20 ± 0.01) mm. To get the length of the simulated rod, the indium layers have to be added. Where applied, the vapor deposited indium can be neglected, as its thickness is ≈ 2 microns. Therefore only the thickness of the used indium sheets has to be added. Sandwich A and B use sheets of 0.25 mm thickness. As shown in Figure 4.1, the indium has creeped due to the force applied, and some of it has been forced out of the sandwich. Assuming conservation of mass and having measured the altered diameter of the sheet after the measurements, the effective thickness has been calculated to be 0.22 mm. For sandwiches A and B the length of the simulated rod, x_{SW}, has therefore been taken to be 1.94 mm. After problems have arised using the thick indium foil on the first vapor deposited sandwich (see section 4.1.2), a thinner foil of 0.125 mm has been used. Here no creep has been observed, so for the last two measured sandwiches (C and D), the rod length has been taken as 1.75 mm. The estimated error of x_{SW} is ± 0.1 mm.

Fixed temperature on one end

The reason why the simple formulas from the theory can't be applied to the used setup is that the temperature variation can not travel freely in space, but is stopped by one end of the system, which is forced to be at a fixed temperature. This temperature is T_{LS}, which is indeed observed to be very constant during all the measurements. Of course, this temperature has to be incorporated in the simulation as well. It is done by extending the simulated rod by a certain length x_{th} at the cold side and fix its temperature at the very end to t_{LS}. This additional part of the rod incorporates everything that is happening between the bottom part of the sandwich and the ^{3}He-^{4}He mixture in the

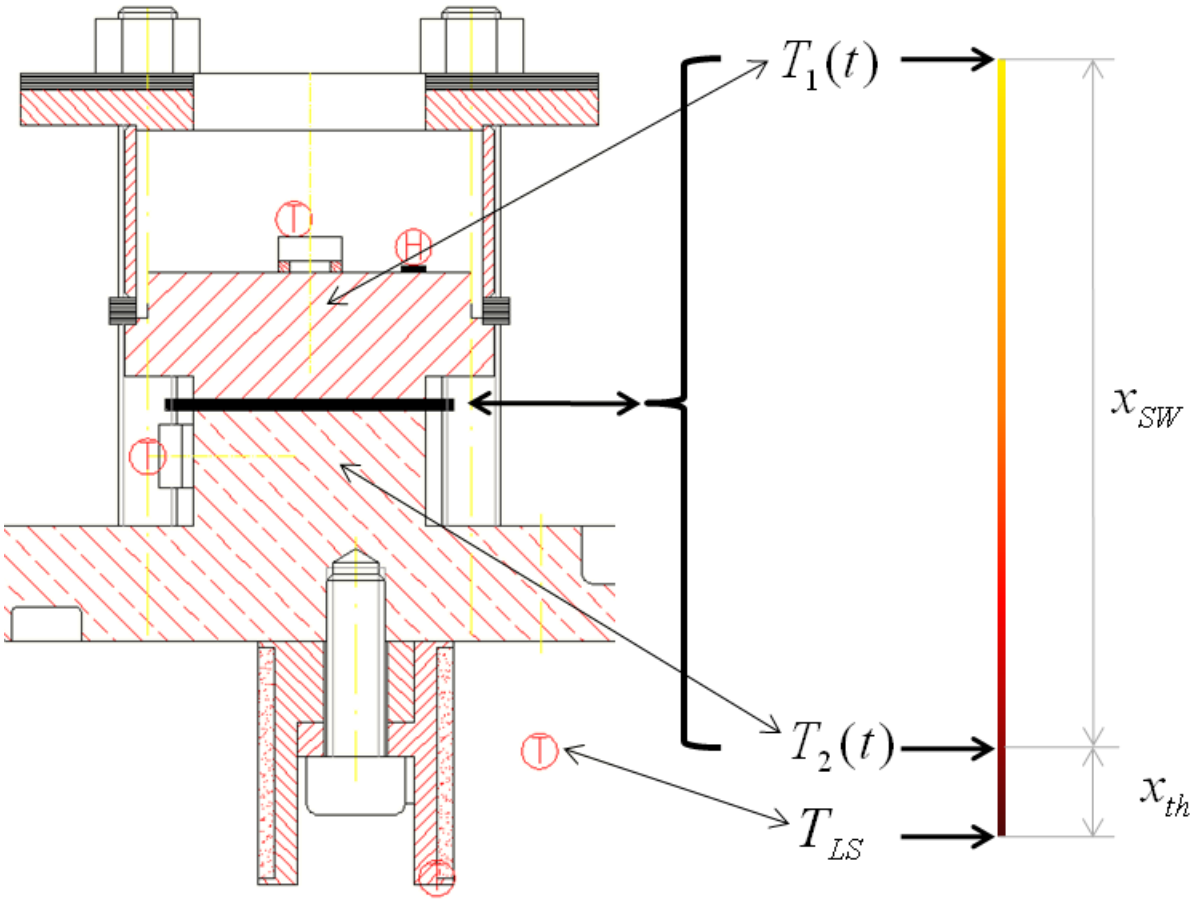

Figure 5.7: Scheme of how the sandwich is modeled for the simulation. In the profile of the real setup (on the left side), the "T" in a circle show the positions of the temperature sensors and the "H" shows the position of the heater.

mixing chamber, including the Kapitza resistance between the liquid helium and the heat exchanger. x_{th} is a parameter, which also has to be optimized during the simulation. Fortunately it can be optimized almost independently from α^*.

Simulation process

The simulation uses the function *pdepe* provided by MATLAB®. It is a partial differential equation (PDE) solver, which can handle one-dimensional initial-boundary value problems of parabolic-elliptic PDEs. A detailed description of the function can be found in the MathWorks documentation [46].
First the model is set to comply with the actual sandwich, i.e. specific values are attributed to the simulation's parameters, namely x_{SW}, x_{th} and T_{LS}. The very latter one

is the average value from the measurement and has already been calculated during data preparation. Also an initial value for α^* has to be chosen. Depending on the needs of the simulation, time and spatial resolution can be altered. For the simulation moderate but large enough values have been used to keep the simulation time at an acceptable level. Also the length of the simulated time span has to be set. Here a value has to be chosen, which makes sure the system reaches the quasi-static state. The quasi-static state can always be reached but the time to reach it depends on the initial conditions (IC) and boundary conditions (BC). The conditions, which have been used were:

- IC: the whole rod is at the temperature T_{LS}.
- BC (top): the top end of the rod is subject to the temperature variation $T_1(t)$.
- BC (bottom): the bottom end is always at the constant temperature of the mixing chamber.

The measured variation of T_1 is taken as a given. After each run of the simulation, the simulated temperature variation $T_{2_{sim}}(t)$ is compared to the real (measured) variation $T_{2_{meas}}(t)$. If the difference is small enough, the used value of α^* is taken as the result of the measurement/simulation. Details of the optimization are discussed in the next paragraph. An example of a simulation output is shown in Figure 5.8.

Optimization of simulation parameters

As stated before, the variable parameters of the simulation are x_{th} and α^*, where the latter one is also the sought-after physical property. Fortunately, each parameter affects the outcome $T_{2_{sim}}(t)$ of the simulation differently, so the parameters can be optimized independently.
The quality of a simulation run is seen when comparing $T_{2_{sim}}(t)$ to $T_{2_{meas}}(t)$. Two examples are given in figures 5.8 and 5.9. Figure 5.8 shows clearly that the chosen parameters for the simulation do not comply with reality well: the average temperatures of T_2 are distant from one another and the shape of the temperature sequence is also very dissimilar. In contrast, Figure 5.9 shows the outcome when using optimized parameters.

The parameter x_{th} is optimized by comparing the average temperature of $T_{2_{sim}}(t)$ to the average temperature of $T_{2_{meas}}(t)$. The value of x_{th} is changed until the two average temperatures are in good accordance. For all measurements the difference between the

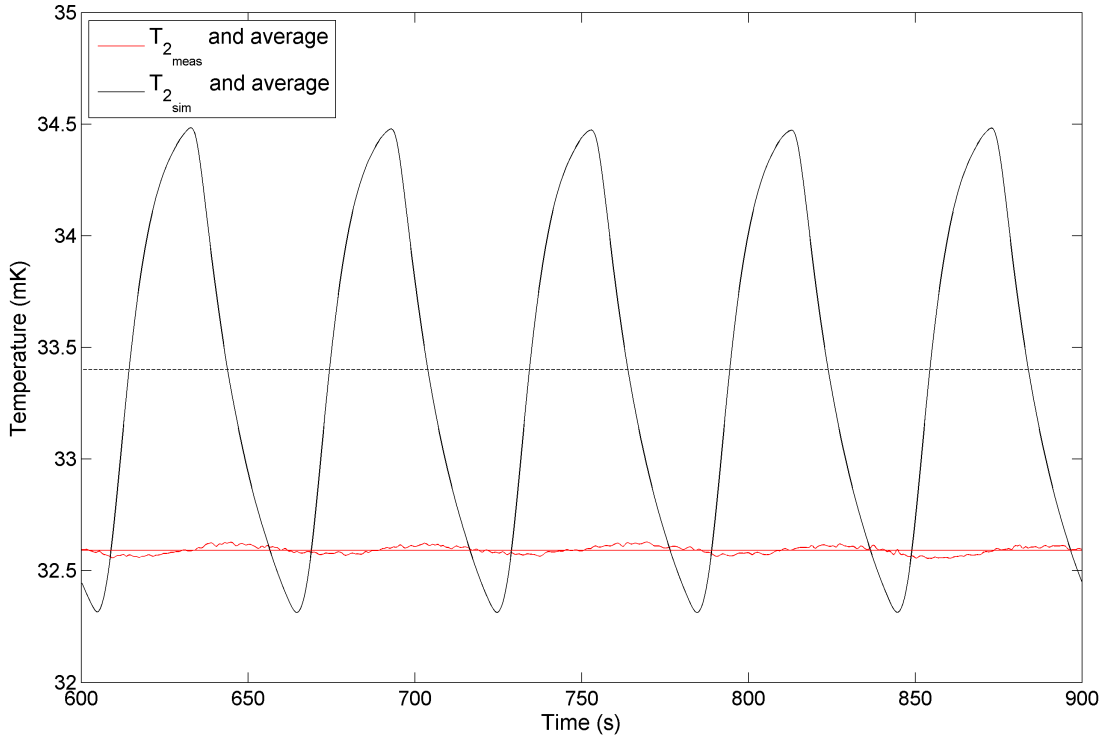

Figure 5.8: Simulation outcome with badly chosen parameters. The simulated temperature variation of T_2 does clearly not fit the measured variation.

average temperatures at the end of the optimization was less than 0.3 %. The optimization of α^* is done similarly, but the value to minimize is $\Delta\varphi$, the difference between the phase shifts of the real oscillation given in $T_{2_{meas}}(t)$ and the simulated oscillation emerging in $T_{2_{sim}}(t)$. For each measurement, the error of $\Delta\varphi$ could be reduced to less than 1 %.
The optimized parameter α^* is taken as the result of the measurement.

5.2.6 Results and discussion of the dynamic measurements

The settings for each measurement and the results are shown in Table 5.1. The interesting value for each sandwich is its thermal diffusivity for a certain temperature. Therefore α^* is averaged over the measurements with different periods. These results are listed in Table 5.1, labeled as $\overline{\alpha^*}$. They are also graphed in Figure 5.10, where a good overview is given and some tendencies can be seen.
The reason for the dynamic measurements is to determine which sandwich transfers heat the fasted. This is directly linked to the values of $\overline{\alpha^*}$: the larger $\overline{\alpha^*}$, the faster the heat transfer, see section 3.5.2. In Figure 5.10 some properties are clearly visible. First, for

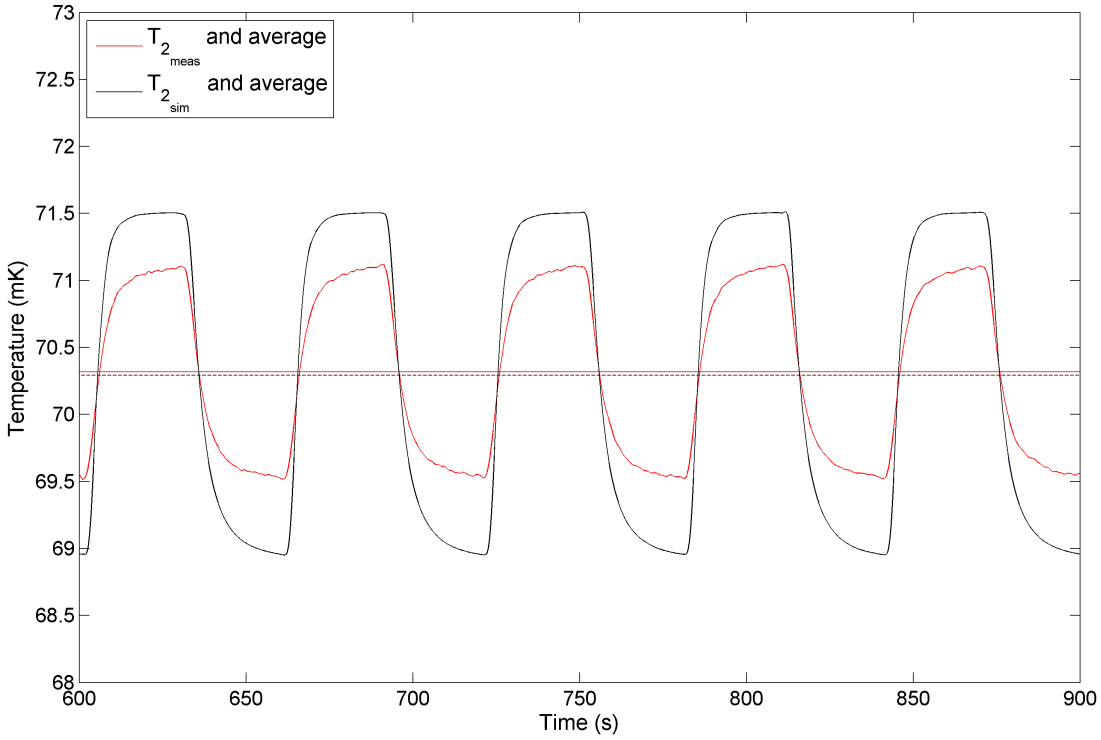

Figure 5.9: Simulation outcome with optimized parameters. The simulated and measured variation of T_2 are in good accordance.

every temperature the order of $\overline{\alpha^*}$ for the sandwiches is the same: Sandwich B shows the lowest value, followed by a slightly larger value for sandwich A. Then a bigger step occurs going to sandwich D and finally the highest values are found for sandwich C. This suggests that polished sapphire disks yield a better thermal diffusivity for the sandwich than rough ones and that physical vapor deposition of indium also supports heat transfer. The relative improvement from rough to polished disks is only small, whereas the additional use of PVD-indium shows significant improvement of the contact.
Furthermore, a dependence of $\overline{\alpha^*}$ on the temperature is clearly visible: $\overline{\alpha^*}$ decreases drastically with a decrease of temperature. This behavior has been expected, since according to theory the thermal resistance of the contact is proportional to T^{-3}. Since measurements at only 3 different temperatures have been conducted, no detailed temperature dependence can be concluded. To do so, measurements at many more different temperatures would be necessary.
The dynamic measurements are aimed to give relative results comparing different sandwiches. Nevertheless, the absolute values of $\overline{\alpha^*}$ are also briefly discussed. They are all in the range of about $10^{-7}\,\mathrm{m^2/s}$. Copper at room temperature has a thermal diffusivity of $1.17 \times 10^{-4}\,\mathrm{m^2/s}$. Below 1 K, this value rises to even 10^{-2} to $10^{1}\,\mathrm{m^2/s}$, which is 5 to 8 orders of magnitude higher than the observed $\overline{\alpha^*}$ for the sandwiches. This shows that the transfer of heat in the sandwich is much slower than in bulk copper, an assumption that has been made earlier in sections 5.2.2 and 5.2.5. This assumption is very important for all measurements on the sandwiches (not only the dynamic ones) and also for the simulation done. Therefore its confirmation assures the quality of the measurements.

The error for α^* is difficult to estimate, since the calculation method for α^* via the simulation inhibits proper calculation of errors. One error source to the simulation is the thickness x_{SW} of the sandwich, having an error of $\pm 0.1\,\mathrm{mm}$. The simulation has also been run with the largest and smallest value for x_{SW} resulting from this error. The difference of the resulting values for α^* are $\approx 12\,\%$.
The effect of uncertainties from other factors like simplifications for the simulation and measurement errors is also estimated to be $\approx 10\,\%$. Averaging over the periods leads to standard deviations for $\overline{\alpha^*}$, which are about half of the size of these errors.
Concerning the averaging over the periods an additional graph is shown in Figure 5.11. It shows α^* over the period for each measurement. This is done to check if the period of the oscillations has effects on the values calculated. As the graph shows, no general correlation between the period and the values of α^* can be seen. This assures the method

of the measurement and analysis procedure and shows that no systematic error is created by choosing a certain value for the period. However, Figure 5.11 shows that the values for α^* for the indium-coated sandwiches at 30 mK rise with smaller periods. The conclusions of this work are not affected by this behavior. If further measurements on indium-coated sapphire disks at 30 mK are done, this effect has to be investigated and understood though. The chemical and physical properties of the PVD-layer of indium might play a role as well as the indium foil, its surface cleaning and its application on the sandwich.

Table 5.1: Results of the dynamic measurements and the simulation. SW . . . measured sandwich, T_{LS} . . . mixing chamber temperature, Period . . . period of the periodic heating, x_{th} . . . thermalization length, Err. $\Delta\varphi$ . . . error of $\Delta\varphi$ (difference between measured and simulated $\Delta\varphi$), α^* . . . thermal diffusivity, $\overline{\alpha^*}$ . . . averaged thermal diffusivity for a given SW and T_{LS}

SW	T_{LS} (mK)	Period (s)	x_{th} (μm)	Err. $\Delta\varphi$ (%)	α^* ($10^{-8}\,m^2/s$)	SW	T_{LS} (mK)	$\overline{\alpha^*}$ ($10^{-8}\,m^2/s$)
A	30	30	180	0.1	5.1			
A	30	40	180	0.3	4.4	A	30	4.7
A	30	60	240	0.1	4.5			
A	50	30	120	0.3	10.8			
A	50	40	120	0	9.5	A	50	9.9
A	50	60	140	0.2	9.5			
A	70	30	140	0.2	23.6			
A	70	40	140	0.1	23.5	A	70	23.6
A	70	60	190	0	23.7			
B	30	30	105	0.1	4.1			
B	30	40	105	0.7	3.6	B	30	3.7
B	30	60	130	0	3.3			
B	50	30	65	0.2	8.9			
B	50	40	65	0.3	8.1	B	50	8.6
B	50	60	80	0.1	8.7			
B	70	30	50	0.2	19.1			
B	70	40	50	0.1	19.2	B	70	19.3
B	70	60	50	0.1	19.5			
C	30	30	180	0.4	8.8			
C	30	40	170	0.5	6.5	C	30	6.6
C	30	60	180	0.6	4.6			
C	50	30	140	0.1	14			
C	50	40	150	0.4	13.6	C	50	13.5
C	50	60	150	0.4	12.8			
C	70	30	100	0.1	32.1			
C	70	40	100	0.1	33	C	70	32.6
C	70	60	100	0.1	32.7			
D	30	30	75	0	8.4			
D	30	40	80	0.2	5.9	D	30	6.1
D	30	60	80	1	4.1			
D	50	30	60	0.5	11.7			
D	50	40	60	0	11	D	50	11.1
D	50	60	60	0.1	10.7			
D	70	30	90	0.1	31.4			
D	70	40	90	0.1	32	D	70	31.9
D	70	60	90	0	32.2			

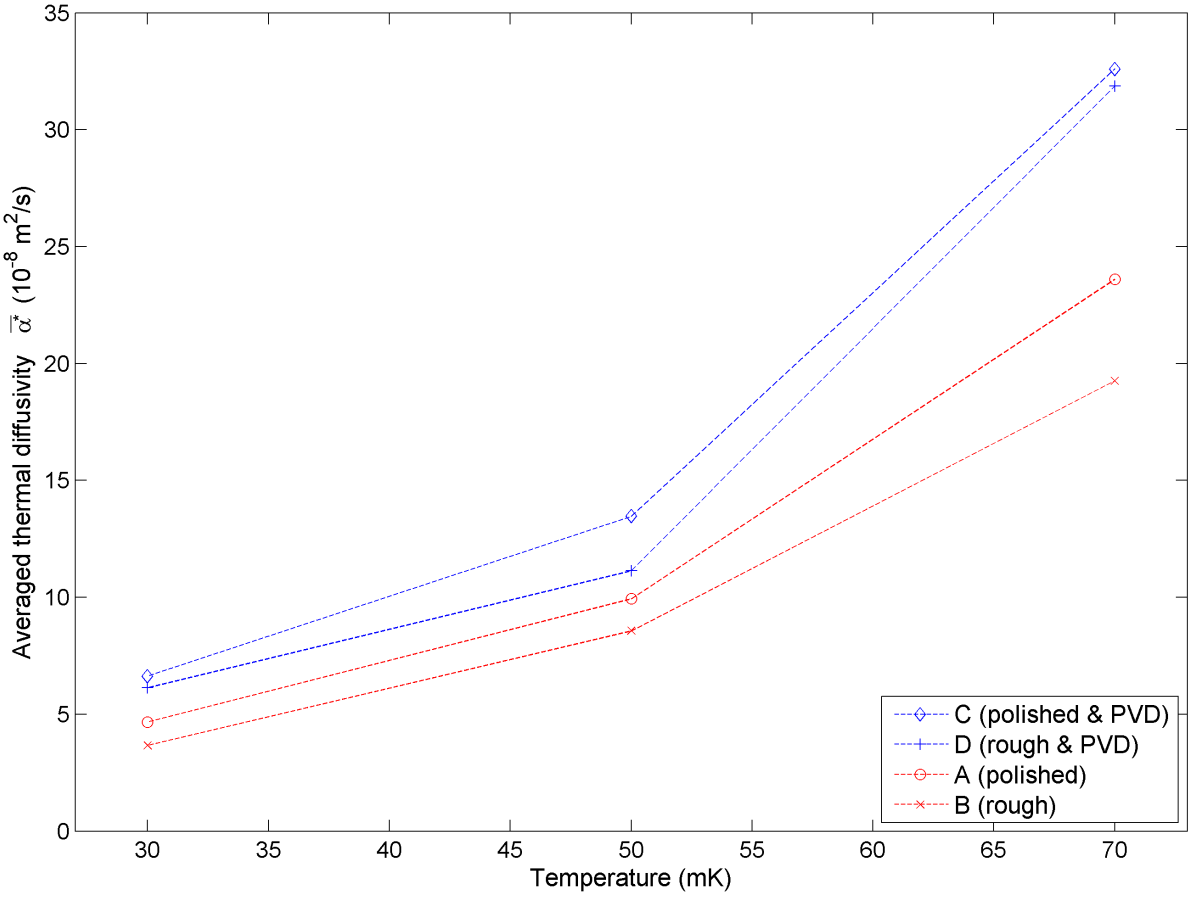

Figure 5.10: Graphic presentation of the results from the dynamic measurements. The averaged thermal diffusivity $\overline{\alpha^*}$ for all measured sandwiches is graphed against the temperature of the mixing chamber, T. It is clearly visible that $\overline{\alpha^*}$ rises significantly with increasing temperature. The differences between the sandwiches are also visible.

5.2.7 Consequences for AEgIS - dynamic measurements

The question is which sandwich should be used for the contact of the electrodes in AEgIS to maximize the speed of heat transfer to the mixing chamber. The results of the dynamic measurements show that polished sapphire disks with PVD-coated indium (sandwich C) has the highest thermal diffusivity and therefore conducts heat the fastest. If no other constraints prohibit the use of this solution, it should be implemented. However, the difference to sandwich D, which uses a PVD-coated rough sandwich, is rather small. In any case, PVD-coating should be applied, since it has rather high influence on the thermal contact as can be seen in Figure 5.10.

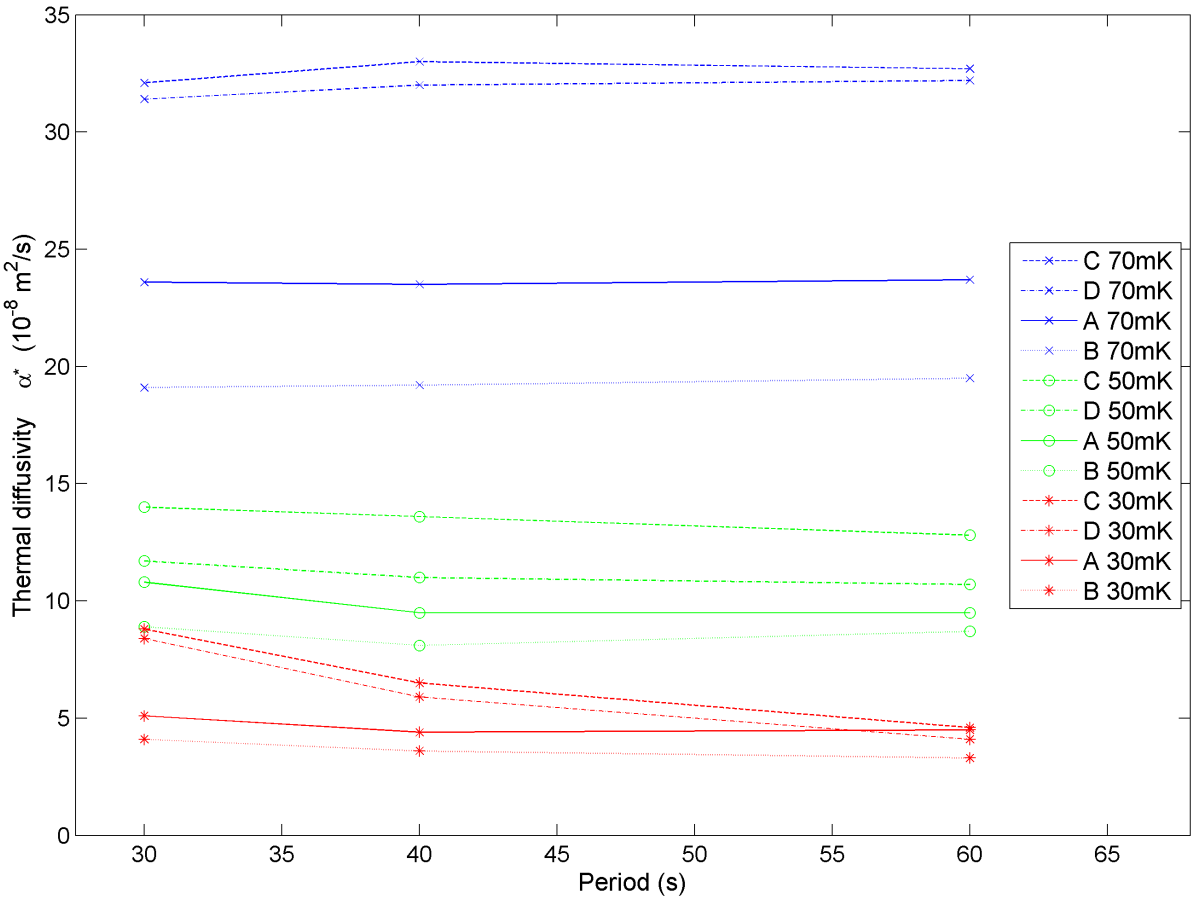

Figure 5.11: Graphic presentation of the results from the dynamic measurements. The thermal diffusivity α^* for all measurements is graphed against the period of the heating. Except for the values for sandwiches C and D at a mixing chamber temperature of 30 mK, no significant influence of the period on the obtained values for α^* is visible.

5.3 Single-step measurements

As explained in section 2.6.2, the electrodes of AEgIS will be heated up periodically from their preset temperature of 100 mK to about 130 mK because of γ radiation during the formation of antihydrogen. It is important to know how long it will take the electrodes to reach their operating temperature again. The step measurements are conducted to give an estimation of this time.

The procedure for the step measurement is quite simple compared to the other measurements. The top part (copper stamp) of the sandwich is heated with a constant heatload until a constant temperature is reached. Then the heating is switched off and the following thermalization process is recorded. The top part of the sandwich cools down to the initial base temperature by heat transfer through the sandwich to the cold mixing chamber. From this, characteristic times for the cooling process of the stamp are calculated and estimations for the cooling time in the final AEgIS setup are made.

The temperature monitored for this measurements are the temperature on the top of the sandwich (T_1) and the mixing chamber temperature (T_{LS}). A representative recorded curve is shown in Figure 5.12.
The heating is done with the same heater as in the dynamic measurements. The heating power is chosen in a way that T_1 is ≈ 30 mK above T_{LS}. For the analysis the measurements at a mixing chamber temperature of 70 mK are chosen. This is due to the estimations done in section 2.6.2: the electrodes in AEgIS will be at about 100 mK and will be heated to about 130 mK because of the pulsed heatloads. The temperature difference of 30 mK is therefore also chosen for the measurements on the test setup. The highest temperature of the mixing chamber is 70 mK for any measurements conducted. This value is the closest to the foreseen operating temperature of the AEgIS electrodes, so it was taken for the analysis.

5.3.1 Analysis - step measurements

From the graph shown in Figure 5.12, the sequence after switching off the heater is of interested, i.e. the part where T_{R1} drops from the plateau to the base temperature. For this part, the temperature curve is fitted with a simple exponential function. The fit includes a term $\exp(-\beta t)$ with t being the time and β the parameter to fit. From β a

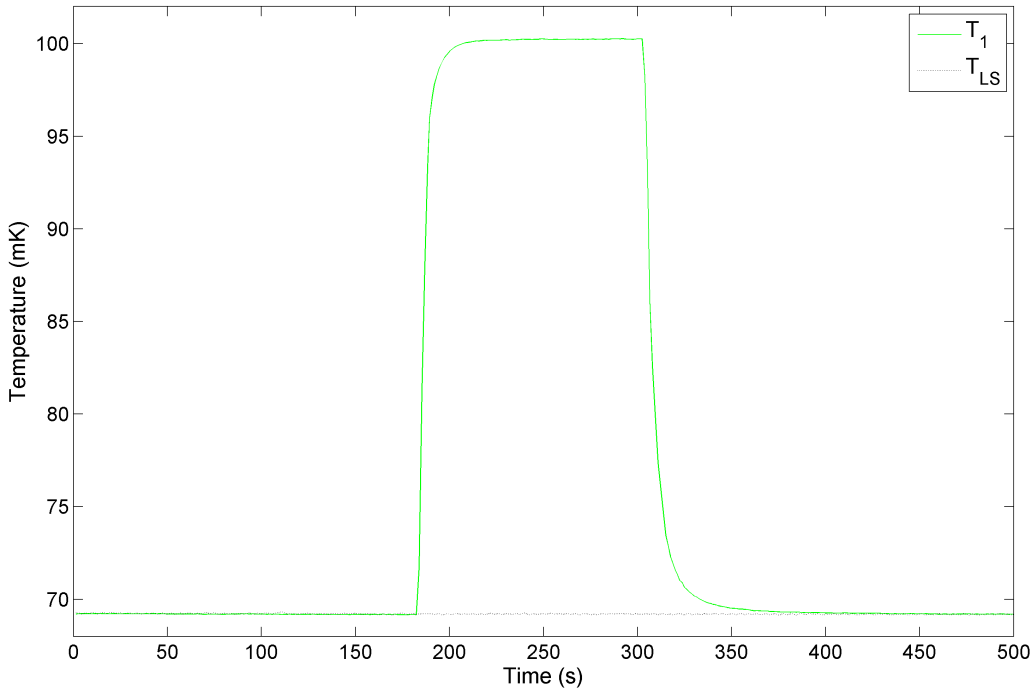

Figure 5.12: Typical temperature sequence of the step measurements. The sandwich is heated for a certain time at the top end, resulting in a high value for T_1. Then the heating is stopped and the falloff curve of T_1 back to the initial temperature is recorded and analyzed.

characteristic time for the falloff curve is calculated, namely its half-life $t_{1/2}$:

$$t_{1/2} = \frac{\ln 2}{\beta} \tag{5.1}$$

It is the time where the curve has fallen to half of its initial value with respect to the baseline, which here is at about 70 mK. In addition, the time after which the temperature has fallen by 95 % of it's initial value is calculated ($t_{95\%}$).
The fitting and calculations are done with MATLAB®.

5.3.2 Results and discussion of the step measurements

The values obtained for the characteristic times of the cooling process are listed in Table 5.2. The half-lives of the falloff process are in the range of several seconds. The half-lives $t_{1/2}$ are only given to make a comparison of the fit and the characteristic times of falloff. For an analysis for AEgIS, $t_{95\%}$ is more important, since it is not fitted but calculated directly from the data.
$t_{95\%}$ ranges from 21 to 39 s. At a given temperature difference of about 30 mK, the level

reached after $t_{95\%}$ is about 1.5 mK above the base temperature. This means that after some tens of seconds the temperature of the stamp on top of the sandwich nearly reaches the base temperature of 70 mK again. After a time of two or three times $t_{95\%}$, the base temperature is practically reached again. The derived values are valid for the test setup and describe the temperature falloff of the copper stamp on the top of the sandwich. The difficulty is to derive estimations for AEgIS out of these values.

5.3.3 Consequences for AEgIS - step measurements

In order to scale the values to the electrodes of AEgIS, the differences between the test setup and AEgIS' final setup have to be identified. The major difference will be the geometry. To be able to make a comparison, the value

$$k = \frac{\text{thermal mass to be cooled}}{\text{area available for heat transfer}}$$

of the two setups is regarded. The area available for heat transfer is the cross section of the sandwich and the sum of the contact areas of all electrodes respectively. The former is the surface area of the sapphire disks used. Given their circular geometry and the diameter of 20 mm, the area is $\approx 3.1\,\mathrm{cm}^2$. For the thermal mass the simple copper mass is taken, since the stamp and the electrodes are made out of the same material (OFHC copper). The mass of the stamp has been determined to be 63 g. This gives a value for k of $20.3\,\mathrm{g/cm}^2$. The design of the Penning trap yields a total mass of the electrodes of 344 g and a surface area available for heat transfer of $80\,\mathrm{cm}^2$ [29]. The resulting value for k is $4.3\,\mathrm{g/cm}^2$. This is about 5 times smaller than the value obtained for the test setup. This means that for a given mass the setup of AEgIS will have five times more area for the heat transfer than the test setup. Thus, the cooling of electrodes will be significantly faster than in the test setup. In addition, the base temperature for the measurements is 70 mK whereas for AEgIS it is forseen to be 100 mK. The speed of heat transfer is determined by the thermal diffusivity of the sandwiches, α^*, which has been

Table 5.2: Results of the single-step measurements.

Sandwich	$t_{1/2}$ (s)	$t_{95\%}(s)$
A	4.4	21.4
B	7.2	39.0
C	3.7	21.0
D	5.5	29.1

determined in the dynamic measurements. The dynamic measurements suggest that α^* rises when going to higher temperatures, which would accelerate the cooling process of the electrodes even more.
Taking all these points into account, a very careful estimation for AEgIS can be done. The electrodes in AEgIS will probably recover from the pulsed heatload from antihydrogen production in several tens of seconds, depending on the type of contact used. If the best contact - sandwich C - is used, then the recovery time is estimated to be below 20 seconds.
These values have to be read with caution, though. Changes of the base temperature or of the high temperature for the electrodes will change the time evolution of the cooling process.
An error calculation is not performed in this section, since the derived values serve only as rough estimations.

5.4 Static measurements

The static measurements reveal information about the constant cooling power, which can be supplied through the sandwich contact to the electrodes. The total thermal resistivity of the contact at different temperatures is calculated. The setup and method is the same as in the dynamic and step measurements. Temperatures at the top and bottom of the sandwich are measured as well as the heating power at the top. A more detailed treatment and discussion of the static measurements will be included in the doctoral thesis of my colleague T. Eisel[7].

Like the other measurements, the static ones are done for each sandwich at three different temperatures of the mixing chamber: 30, 50 and 70 mK. At each temperature the top part is heated with a certain power and the static case is waited for. Then the temperatures are recorded at the top of the sandwich and at the bottom. From these values the total thermal resistivity R_T is calculated by equation (3.14). This is done with the series of the different heatloads applied to the stamp.
For each different temperature of the stamp, thermal equilibrium has to be waited for. After changing the temperature of the stamp, the measurements can only start after some time, typically after 30 minutes. Then the temperature readout of the sensors is done and the heating power is changed to the next value. This procedure is normally done automatically and even then one measurement for a given sandwich and mixing chamber temperature takes about 30 hours, depending on the settings. An example of a typical measurement is shown in Figure 5.13.

5.4.1 Analysis - static measurements

Once the data are prepared and in the right format, the actual calculation of the total thermal resistivity is done by equation (3.14). As explained before, the usual way to present the resistivity is to plot $R_T T^3$ against the temperature T_1 of the warm side of the contact. Attention has to be paid to what the resistivity actually represents. R_T is not the thermal resistivity of one contact, but of the whole sandwich. So R_T includes the thermal resistivities of the two indium-sapphire interfaces as well as the thermal resistivity of the bulk sapphire. The latter is however small compared to the contact resistivities as explained in chapter 3.

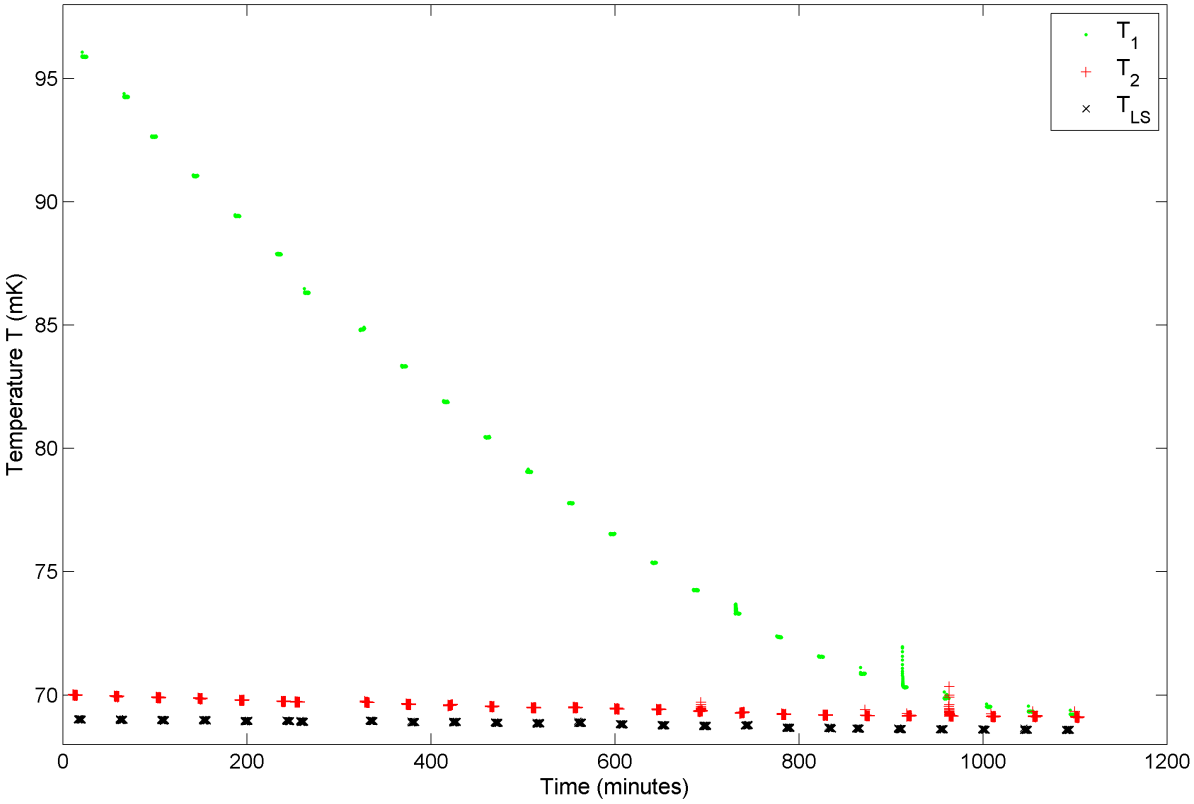

Figure 5.13: Typical temperature sequence of the static measurements. The heating power is stepwise decreased and the temperatures T_1, T_2 and T_{LS} are measured at each step. The visible peaks in this plot (for example between $t = 900$ and 1000 minutes) are due to the electronics when switching channels of the AVS47-B and are not taken for the analysis.

5.4.2 Results and discussion of the static measurements

The values for the total thermal resistivity of the sandwich are summarized in Figure 5.14. The lower the values for $R_T T^3$, the better the thermal contact achieved by the sandwich. According to theory, a perfect contact would yield a horizontal line, representing the predicted T^{-3}-dependence of the thermal resistivity. The values for the sandwich with the lowest and therefore best values for $R_T T^3$ (sandwich C) are indeed much closer to a horizontal line than the values for sandwich B, the sandwich showing the worst thermal contact. This is in accordance with the results from the dynamic measurement: also there sandwich C creates the best contact and sandwich B the worst. For sandwich A and D the measurements differ in the results. The dynamic measurements shows that the main improvement of the contact is achieved by the physical vapor deposition of indium on the sapphire disk and not by the surface roughness of the disk. The static measurements however suggest that the surface roughness influences the contact quality more than the vapor deposited layer of indium. Still, an agreement is found on the best solution: sandwich C, made up of a polished sapphire disk with a thin layer of vapor deposited indium provides the best thermal contact in the static case as well as in the dynamic case.
Figure 5.15 shows the transferred heatload against the temperature T_1 of the warm side of the sandwich. Like the results from the dynamic measurements, the curve shows that the thermal contact improves drastically with increase of temperature. For each sandwich and temperature of the mixing chamber such a graph exists. A higher T_1 means a higher temperature difference between the two sides of the sandwich. Therefore, the graphs can be used to calculate the transferable heatload across a contact with arbitrary surface area and given temperature difference, as long as the contact is built up the same way as the respective sandwich and as long as the temperature on the cold side is the same as in the measurement.

5.4.3 Consequences for AEgIS - static measurements

The static measurements show that also for the constant heatloads sandwich C offers the best solution. At given temperatures on both sides of the sandwich, it will be able to transfer larger heatloads than any other solution investigated from the electrodes to the mixing chamber. An estimation with the current specifications for AEgIS yield a total transferable heatload for the final setup of 70 μW [48]. An exact estimation of the heatloads expected on the electrodes in the final setup has not been performed yet, due

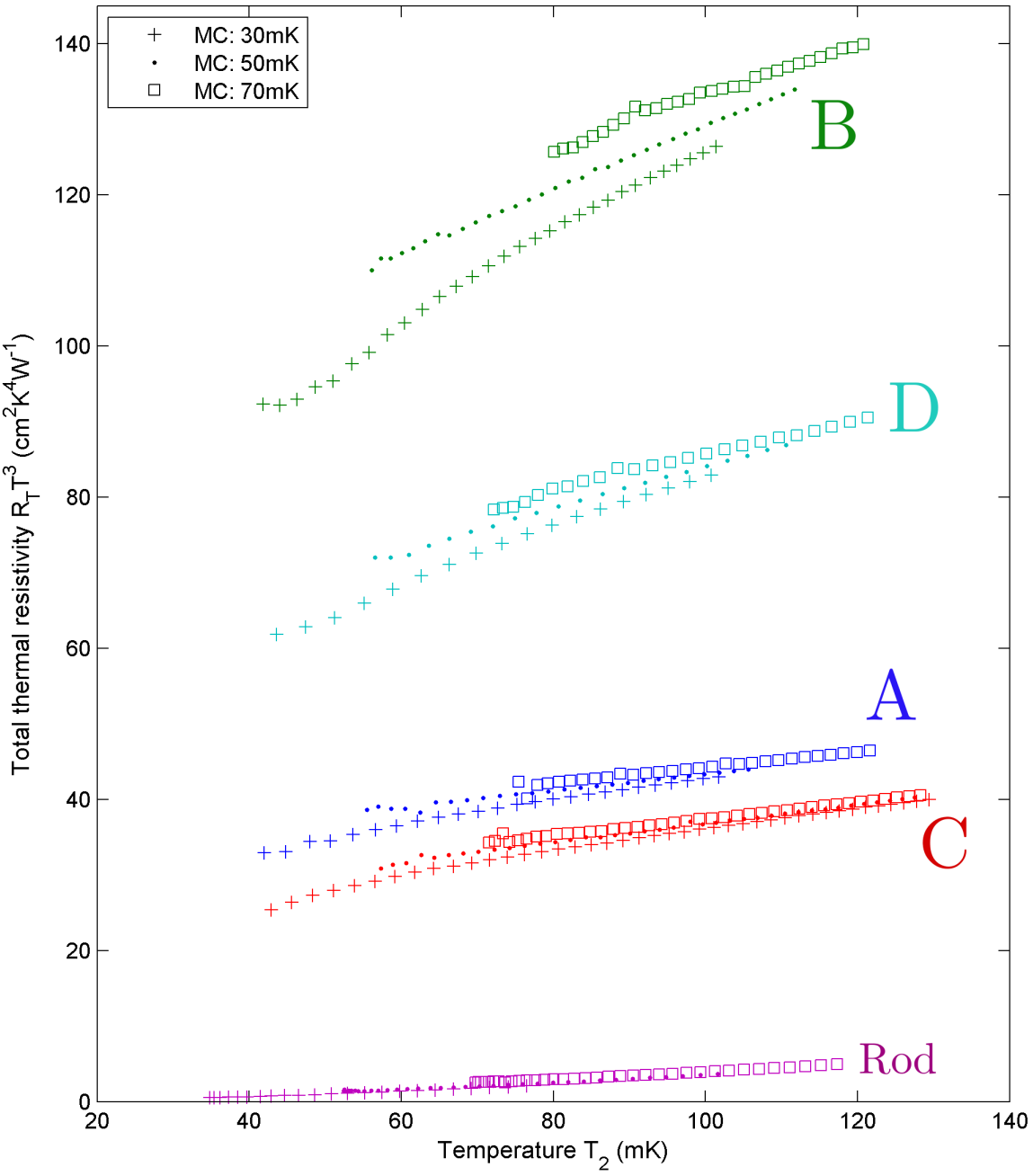

Figure 5.14: Summarized results of the static measurements graphed as total thermal resistivity $R_T T^3$ against T_2 for all sandwiches and also the rod-solution for comparison [47]. Discussion in the text.

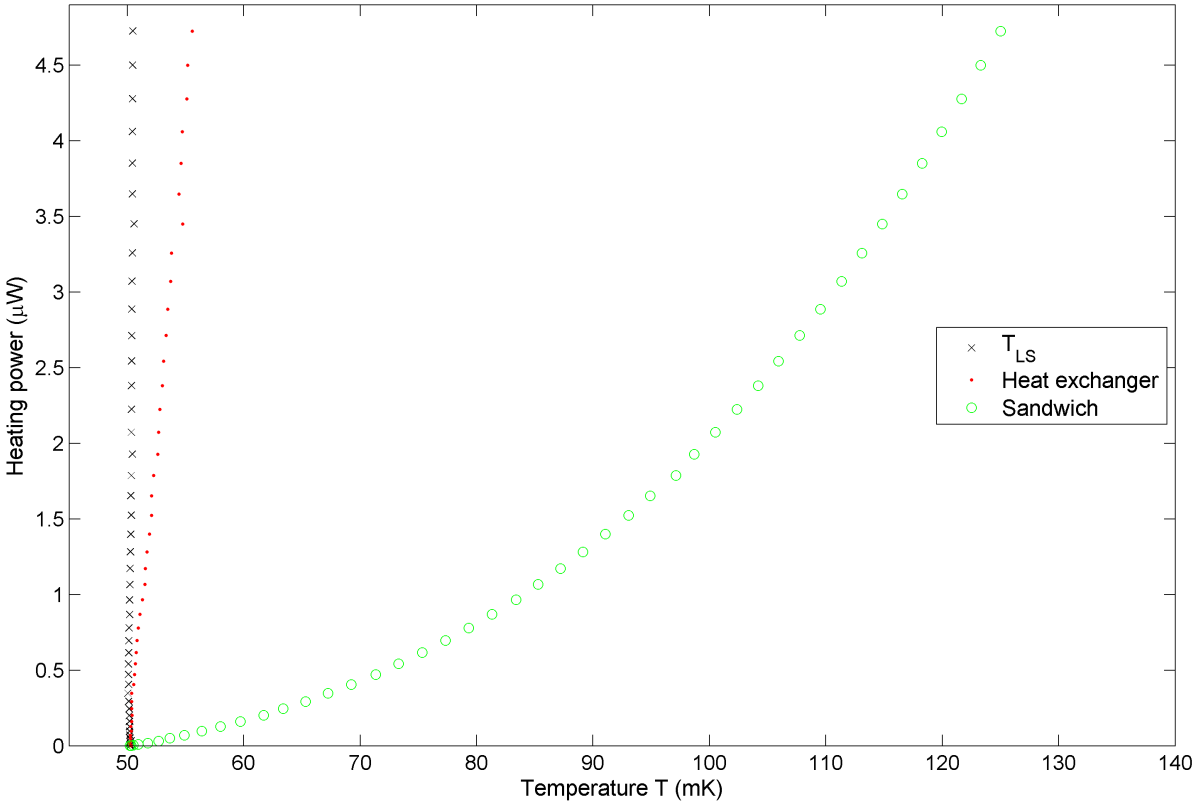

Figure 5.15: Result of a typical static measurement (sandwich C, $T_{LS} = 50\,\mathrm{mK}$). The heating power is graphed against T_1. T_{LS} is just graphed as a reference. The two curves for the heat exchanger and for the sandwich, respectively, show the heatload which can be transferred at a given temperature difference between T_{LS} and T_1.

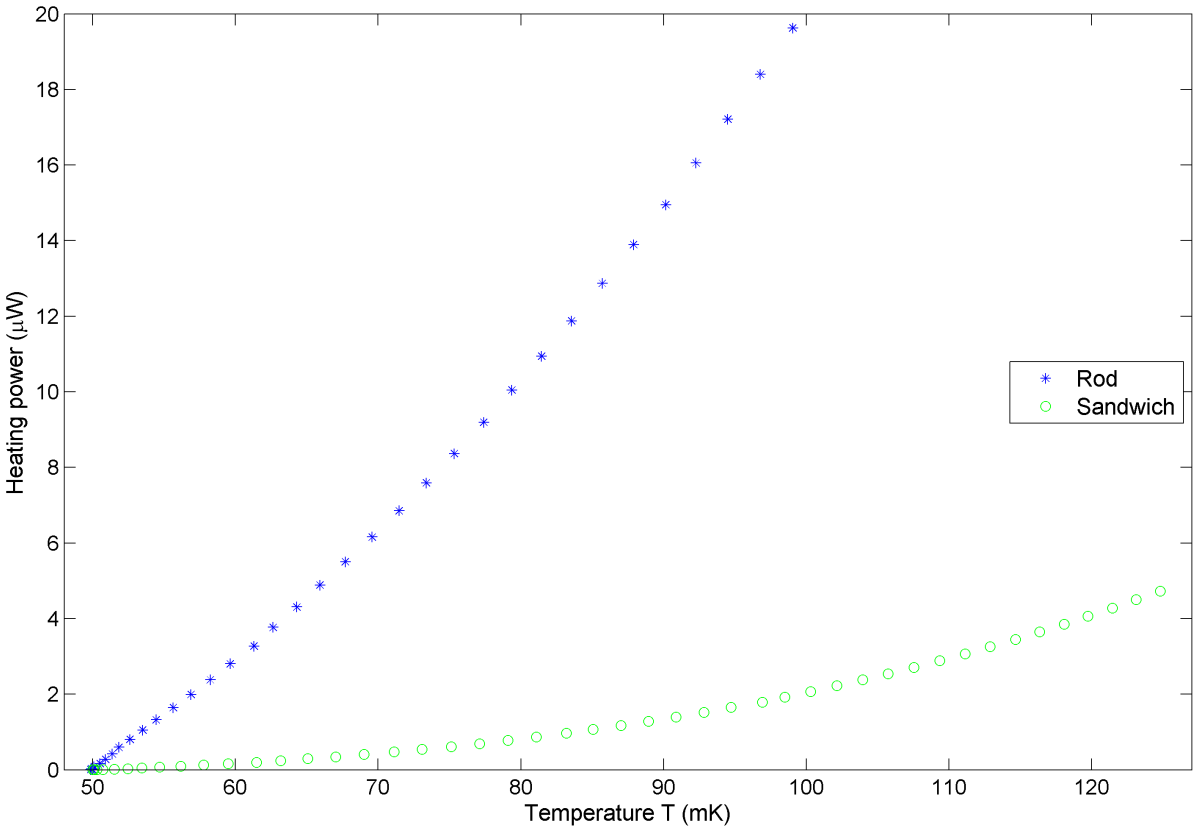

Figure 5.16: Result of the measurement shown in Figure 5.15 compared to a measurement on the rod-solution. Here it is clear why the rod-solution is better concerning the thermal properties: at a given temperature difference between T_{LS} and T_1 the rod can transfer a much larger heat load than the sandwich.

to incomplete information about the surroundings of the cold part. AEgIS is still in the planning phase and the exact design around the cold part is not yet fully specified. As soon as the specifications of the surroundings are fixed, an estimation of the heatloads can be done. If this reveals that the estimated $70\,\mu$W are not enough for AEgIS, an improved thermal contact for the electrodes has to be found and/or the heatloads on the electrodes have to be reduced.

6 Conclusions and Outlook

6.1 Summary

The work presented was conducted to test thermal contacts at ultra low temperatures for their suitability for the antimatter experiment AEgIS at CERN. AEgIS requires a connection between two copper pieces, which conducts heat well and electrically insulates at the same time. Sandwiches made out of a sapphire disk and thin indium layers provide such a connection. Since the preparation of the sandwiches has strong influence on their thermal properties, differently prepared test sandwiches were investigated to get the optimum solution. The sandwiches differed in the surface roughness of the sapphire disk and the application method of the indium layers. Out of the four sandwiches investigated, the sandwich with the optically polished sapphire disk and thin layers of physically vapor deposited indium showed the best thermal properties. This means it was conducting heat faster than the other sandwiches and also provided the highest transferable heatload at a given temperature difference between its two sides.
Furthermore, an estimation of the constantly transferable heatload from the electrodes of the Penning trap to the dilution refrigerator in the AEgIS setup when using the optimum contact method was made. The time it takes to cool the electrodes to the foreseen operating temperature of 100 mK after they experienced the heat pulse from the antihydrogen formation was also estimated.
All sought-after values were derived from thermal measurements in the temperature range between 30 and 130 mK. These temperatures were reached by using the CERN Cryolab Dilution Refrigerator (CCDR).
The results of the measurements are presented and discussed in detail in sections 5.2 to 5.4.

6.2 Consequences for AEgIS and future work

Three different measurement methods were used: dynamic, single-step and static measurements. All three of them showed that the contact with the best thermal properties is the one using a polished sapphire disk with a physically vapor deposited indium layer on each side. This solution should therefore be preferred when implementing a sandwich solution for the contact of the electrodes to the mixing chamber. It will transfer heat the fastest of all the sandwiches tested.
The heat pulse, which will be caused by the formation of antihydrogen in AEgIS, will rise the electrodes' temperature from their operating temperature of 100 mK to about 130 mK. With the optimum sandwich solution applied, the time to cool them back down to 100 mK was estimated to be less than 20 s. The period of antihydrogen formation will be about 120 s, so there will be about 100 s left during each period in which the electrodes are on their operating temperature and cooling of the trapped antiprotons can be achieved.
The heatloads acting on the cold electrodes could not be estimated, since the final design of AEgIS had not been fixed yet. However, an estimation of the constant heatload, which can be transferred from the electrodes to the mixing chamber when using the optimum contact method, was made. Assuming the electrodes' contact surface being 80 cm^2, the electrode temperature 100 mK and the mixing chamber lid temperature 55 mK, this heatload was estimated to be 70 μW. Before fixing the final design for AEgIS, it has to be verified that the overall heatload on the electrodes will be less than this value. Otherwise a better thermal contact between the electrodes and the mixing chamber has to be found, which would involve further measurements with the CCDR.

An other possible solution to engineer the electrodes emerged just after having finished the measurements and analysis for this work. It might be possible to manufacture the electrodes as a whole from sapphire and applying gold coating in a way that ensures the geometry of the electric field required in the Penning trap. For this solution the results presented are also useful, since the thermal contact still has to be realized between sapphire and copper. Determining which solution is the most advantageous for AEgIS is subject of ongoing studies.

Appendices

A Collaboration members of AEgIS

As of autumn 2010 [13]:

- LAPP, Annecy, France: G. Drobychev, D. Sillou
- Queen's U Belfast, UK: G. Gribakin, H.R.J.Walters
- INFN Firenze, Italy: G.Ferrari, M. Prevedelli
- CERN: M. Doser, A. Duradev, T. Eisel, F. Haug, T. Niinikoski, D. Perini , J. Bremer, T. Kaltenbacher, S. Feigl
- INFN Genova, Italy: C. Canali, C. Carraro, L. Di Noto, V. Lagomarsino, G. Manuzio, G. Testera, R. Vaccarone, S. Zavatarelli
- MPI-K Heidelberg: R. Heyne, A. Fischer, A. Kellerbauer, C. Morhard, U. Warring
- Kirchoff Inst. Of Phys., Heidelberg, Germany: M. Oberthaler, P. Bräunig, F. Haupert
- INFN Milano, Italy: I. Boscolo, F. Castelli, S. Cialdi, L. Formaro, M. Giammarchi, F. Prelz, M. Sacerdoti, D. Trezzi, F. Villa
- INR Moscow, Russia: A.S. Belov, S. Gninenko, V. A. Matveev, A. V. Turbabin
- ITEP Moscow, Russia: W. M. Byakov, S. V. Stepanov , D.S. Zvezhinskij
- Université Claude Bernard, Lyon, France: P.Nedelec
- New York Univ. USA: H.H. Stroke
- University of Oslo and University of Bergen, Norway: O. Rohne, S. Stapnes, H. Sandacker
- INFN Pavia-Brescia, Italy: G.Bonomi, A. Fontana, C. Riccardi, A. Rotondi, A. Zenoni

- Czech Tech. Univ, Prague, Czech Republic: V. Petracek, D. Krasnicky
- IRNE Sofia, Bulgary: N. Djurelov
- INFN Padova-Trento, Italy: R.S. Brusa, S. Mariazzi
- ETH Zurich, Switzerland: S.D. Hogan, F. Merkt
- Qatar University: I. Y. Al-Qaradawi, L. Jorgensen
- Politecnico Milano, Italy: G. Consolati, A. Dupasquier, R. Ferragut, P. Folegati, F. Quasso
- Lab. Aimé Cotton, Orsay, France: L. Cabaret, D. Comparat
- University of Zurich, Switzerland: Y. Allkofer, C. Amsler, C. Regenfus, J. Rochet, J. Storey.

Bibliography

[1] W. Fairbank *et al.* in *Proc. Int. School Phys. Enrico Fermi* (B. Bertotti, ed.), (New York), p. p. 310, Academic Press, 1974.

[2] M. Holzscheiter, R. Brown, J. Camp, S. Cornford, T. Darling, P. Dyer, T. Goldman, S. Høibråten, K. Hosea, R. Hughes, N. Jarmie, R. Kenefick, N. King, D. Lizon, M. Nieto, M. Midzor, S. Parry, J. Rochet, R. Ristinen, M. Schauer, J. Schecker, and F. Witteborn, "Trapping of antiprotons in a large penning trap – progress towards a measurement of the gravitational acceleration of the antiproton," *Nuclear Physics A*, vol. 558, pp. 709 – 718, 1993.

[3] F. Pobell, *Matter and Methods at Low Temperatures; 3^{rd} ed.* Heidelberg: Springer, 2007.

[4] E. T. Swartz and R. O. Pohl, "Thermal boundary resistance," *Rev. Mod. Phys.*, vol. 61, pp. 605–668, Jul 1989.

[5] C. Schmidt and E. Umlauf, "Thermal boundary resistance at interfaces between sapphire and indium," *Journal of Low Temperature Physics*, vol. 22, pp. 597–611, 1975.

[6] D. A. Neeper and J. R. Dillinger, "Thermal resistance at indium-sapphire boundaries between 1.1 and 2.1°k," *Phys. Rev.*, vol. 135, pp. A1028–A1033, Aug 1964.

[7] T. Eisel (forthcoming), *Thermal Measurements for AEgIS.* PhD thesis, 2011.

[8] W. N. Cottingham and D. A. Greenwood, *An Introduction to the Standard Model of Particle Physics; 2nd ed.* Cambridge: Cambridge Univ. Press, 2007.

[9] M. Doser AEgIS collaboration Private Communication, September 2010.

[10] G. Baur, G. Boero, A. Brauksiepe, A. Buzzo, W. Eyrich, R. Geyer, D. Grzonka, J. Hauffe, K. Kilian, M. LoVetere, M. Macri, M. Moosburger, R. Nellen, W. Oelert,

S. Passaggio, A. Pozzo, K. Röhrich, K. Sachs, G. Schepers, T. Sefzick, R. S. Simon, R. Stratmann, F. Stinzing, and M. Wolke, "Production of antihydrogen," *Physics Letters B*, vol. 368, no. 3, pp. 251 – 258, 1996.

[11] M. Amoretti, C. Amsler, G. Bonomi, A. Bouchta, P. Bowe, C. Carraro, C. L. Cesar, M. Charlton, M. J. T. Collier, M. Doser, V. Filippini, K. S. Fine, A. Fontana, M. C. Fujiwara, R. Funakoshi, P. Genova, J. S. Hangst, R. S. Hayano, M. H. Holzscheiter, L. V. Jorgensen, V. Lagomarsino, R. Landua, D. Lindelof, E. L. Rizzini, M. Macri, N. Madsen, G. Manuzio, M. Marchesotti, P. Montagna, H. Pruys, C. Regenfus, P. Riedler, J. Rochet, A. Rotondi, G. Rouleau, G. Testera, A. Variola, T. L. Watson, and D. P. van der Werf, "Production and detection of cold antihydrogen atoms," *Nature*, vol. 419, pp. 456–459, Oct. 2002.

[12] A. Kellerbauer, M. Amoretti, A. Belov, G. Bonomi, I. Boscolo, R. Brusa, M. Büchner, V. Byakov, L. Cabaret, C. Canali, C. Carraro, F. Castelli, S. Cialdi, M. de Combarieu, D. Comparat, G. Consolati, N. Djourelov, M. Doser, G. Drobychev, A. Dupasquier, G. Ferrari, P. Forget, L. Formaro, A. Gervasini, M. Giammarchi, S. Gninenko, G. Gribakin, S. Hogan, M. Jacquey, V. Lagomarsino, G. Manuzio, S. Mariazzi, V. Matveev, J. Meier, F. Merkt, P. Nedelec, M. Oberthaler, P. Pari, M. Prevedelli, F. Quasso, A. Rotondi, D. Sillou, S. Stepanov, H. Stroke, G. Testera, G. Tino, G. Trénec, A. Vairo, J. Vigué, H. Walters, U. Warring, S. Zavatarelli, and D. Zvezhinskij, "Proposed antimatter gravity measurement with an antihydrogen beam," *Nuclear Instruments and Methods in Physics Research Section B: Beam Interactions with Materials and Atoms*, vol. 266, no. 3, pp. 351 – 356, 2008. Low Energy Positron and Positronium Physics - Proceedings of the XIV International Workshop on Low Energy Positron and Positronium Physics.

[13] "Aegis homepage at cern." `http://www.mi.infn.it/$\sim$trezzi/aegis.htm`. (Online; as of Sep. 2010).

[14] "Homepage of the ad complex at cern." `http://psdoc.web.cern.ch/PSdoc/acc/ad/index.html`. (Online; as of Sep. 2010).

[15] "Scheme of the antiproton decelerator at cern." `http://commons.wikimedia.org/wiki/File:Antiproton_Decelerator_CERN.svg`. (Online; as of Sep. 2010).

[16] M. Doser and the Aegis collaboration, "Aegis: An experiment to measure the grav-

itational interaction between matter and antimatter," *Journal of Physics: Conference Series*, vol. 199, no. 1, p. 012009, 2010.

[17] G. Testera, A. S. Belov, G. Bonomi, I. Boscolo, N. Brambilla, R. S. Brusa, V. M. Byakov, L. Cabaret, C. Canali, C. Carraro, F. Castelli, S. Cialdi, M. de Combarieu, D. Comparat, G. Consolati, N. Djourelov, M. Doser, G. Drobychev, A. Dupasquier, D. Fabris, R. Ferragut, G. Ferrari, A. Fischer, A. Fontana, P. Forget, L. Formaro, M. Lunardon, A. Gervasini, M. G. Giammarchi, S. N. Gninenko, G. Gribakin, R. Heyne, S. D. Hogan, A. Kellerbauer, D. Krasnicky, V. Lagomarsino, G. Manuzio, S. Mariazzi, V. A. Matveev, F. Merkt, S. Moretto, C. Morhard, G. Nebbia, P. Nedelec, M. K. Oberthaler, P. Pari, V. Petracek, M. Prevedelli, I. Y. Al-Qaradawi, F. Quasso, O. Rohne, S. Pesente, A. Rotondi, S. Stapnes, D. Sillou, S. V. Stepanov, H. H. Stroke, G. Tino, A. Vairo, G. Viesti, H. Walters, U. Warring, S. Zavatarelli, A. Zenoni, and D. S. Zvezhinskij, "Formation of a cold antihydrogen beam in aegis for gravity measurements," *AIP Conference Proceedings*, vol. 1037, no. 1, pp. 5–15, 2008.

[18] AEgIS Collaboration, Internal Document: `https://edms.cern.ch/nav/CERN-0000083842%26expand_open=Y`, June 2010.

[19] Y. H. Huang and G. B. Chen, "A practical vapor pressure equation for helium-3 from 0.01 k to the critical point," *Cryogenics*, vol. 46, pp. 833–839, 2006.

[20] B. Sethumadhavan, W. Yao, Y. H. Huang, R. E. Lanou, H. J. Maris, and G. M. Seidel, "Electrical breakdown in helium cells at low temperature," *Phys. Rev. Lett.*, vol. 97, p. 015301, Jul 2006.

[21] B. Sethumadhavan, *Electrical Breakdown in Helium Cells at Low Temperature*. PhD thesis, Brown University, Providence, Rhode Island, May 2007.

[22] G. Seidel Private Communication, January 2010.

[23] J. Gerhold, "Properties of cryogenic insulants," *Cryogenics*, vol. 38, no. 11, pp. 1063–1081, 1998.

[24] K. Yoshino, K. Ohseko, M. Shiraishi, M. Terauchi, and Y. Inuishi, "Dielectric breakdown of cryogenic liquids in terms of pressure, polarity, pulse width and impurity," *Journal of Electrostatics*, vol. 12, pp. 305 – 314, 1982.

[25] A. Phillips and P. V. E. McClintock, "Field emission and field ionization in liquid 4he," *Philosophical Transactions of The Royal Society A*, vol. 278, pp. 271–310, 1975.

[26] C. Blank and M. Edward, "Dielectric breakdown of liquid helium," *Physical Review*, vol. 119, pp. 50–53, July 1960.

[27] J. Suehiro, K. Ohno, T. Takahashi, M. Miyama, and M. Hara, "Statistical characteristics of electrical breakdown in saturated superfluid helium," in *Conference Record of the ICDL '96 12th International Conference on Conduction and Breakdown in Dielectric Liquids*, (Roma, Italy), pp. 320–323, July 1996.

[28] W. F. Schmidt, E. Illenberger, A. Khrapak, Y. Sakai, and K. Yoshino, "Electronic conduction and breakdown in liquid helium and liquid neon," *IEEE Transactions on Dielectrics and Electrical Insulation*, vol. 10, pp. 1012 –1021, December 2003.

[29] G. Burghart AEgIS collaboration Private Communication, September 2010.

[30] C. Enss and S. Hunklinger, *Tieftemperaturphysik*. Berlin: Springer, 2000.

[31] P. L. Kapitza *J. Phys. (U.S.S.R.)*, vol. 4, p. 181, 1941.

[32] I. Khalatnikov *Zh. Eksp. i Teor Fiz.*, vol. 22, p. 687, 1952.

[33] G. L. POLLACK, "Kapitza resistance," *Rev. Mod. Phys.*, vol. 41, pp. 48–81, Jan 1969.

[34] W. Little, "The transport of heat between dissimilar solids at low temperatures," *Canadian Journal of Physics*, vol. 37, no. 3, pp. 334–349, 1959.

[35] E. T. Swartz and R. O. Pohl, "Thermal resistance at interfaces," *Applied Physics Letters*, vol. 51, pp. 2200 –2202, dec. 1987.

[36] G. Frossati, "Experimental techniques: Methods for cooling below 300 mk," *Journal of Low Temperature Physics*, vol. 87, no. 3, pp. 595–633, 1992.

[37] L. Wang, *Heat conduction: mathematical models and analytical solutions*. Berlin: Springer, 2007.

[38] R. Erlebach Protocol Friedrich-Schiller-Universität Jena, `http://www.personal.uni-jena.de/~p1erra/physik/protokolle/seite%20129-%20versuch%20210.pdf`, 2002.

[39] J. W. Ekin, *Experimental Techniques for Low-Temperature Measurements: Cryostat Design, Material Properties, and Superconductor Critical-Current Testing*. Oxford: Oxford Univ. Press, 2006.

[40] K. Blaser Private Communication with Djeva SA, Monthey, Switzerland, March 2010.

[41] "Online shop where the indium has been ordered from." `http://www.idbscb.com/`. (Online; as of Sep. 2010).

[42] "Product overview of ruthenium oxide resistive thermal devices from lakeshore." `http://www.lakeshore.com/temp/sen/rrtd.html`. (Online; as of Sep. 2010).

[43] W. van der Veur, "Calibration of ruo2 temperature sensors in the 25mk-1k range." Internship thesis, August 2009.

[44] P. Das, R. de Bruyn Ouboter, and K. Taconis *Proc. 9th Int. Conf. on Low Temp. Phys.*, p. 1253, 1965.

[45] "Dilution refrigeration explained on the homepage from the na47-experiment of the spin muon collaboration at cern (by peter berglund)." `http://na47sun05.cern.ch/target/outline/dilref.html`. (Online; as of Sep. 2010).

[46] "Matlab r2010b mathworks documentation." `http://www.mathworks.com/help/techdoc/ref/pdepe.html`. (Online; as of Sep. 2010).

[47] T. Eisel *Proc. 23th International Cryogenic Engineering Conference*, 2010.

[48] T. W. Eisel AEgIS collaboration internal presentation, June 2010.